Linear and nonlinear properties of photonic band-gap fibres

Luan, Feng

Award date:
2005

Awarding institution:
University of Bath

LINEAR AND NONLINEAR PROPERTIES OF PHOTONIC BAND-GAP FIBRES

Feng Luan

A thesis submitted for the degree of Doctor of Philosophy

University of Bath
Department of Physics

February 2005

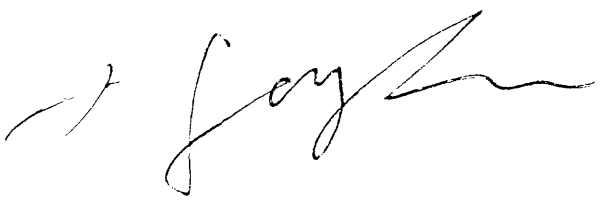

ProQuest LLC
789 East Eisenhower Parkway
P.O. Box 1346
Ann Arbor, MI 48106-1346

Abstract

This thesis reports the design, fabrication and characterisation of the first photonic bandgap fibre (PBGF) to be formed from two solid materials (two different glasses). It also reports the characterisation of a bandgap fibre with a hollow core, and the use of this fibre for delivery of high-power ultrashort optical pulses. Finally, a novel feature of soliton propagation in solid-core photonic crystal fibres is reported and explained.

The first all-solid PBGF was fabricated and characterised. The transmitted spectrum shows several low-attenuation windows, which stand out from the background by more than 30dB. The measured dispersion has shown anomalous region in the transmission bands despite the huge normal dispersion from the material. The bandgap formation in all solid PBGFs is attributed to antiresonances of the high-index strands in the cladding.

A hollow-core photonic bandgap fibre designed for use in the 850nm wavelength region is characterised. The fibre has a minimum attenuation of 180dB/km at 847nm wavelength. The low-loss mode has a quasi-Gaussian intensity profile. The group-velocity dispersion of this mode passes through zero around 830nm, and is anomalous for longer wavelengths. The slight departure from perfection in the fibre fabrication leads to a splitting of the polarisation modes, and the polarisation beat length is measured to vary from 4mm to 13mm across the band gap. Comparing the operation of both solid-core and hollow-core bandgap fibres sheds light on the operation of the hollow-core variety.

Femtosecond solitons at 800nm wavelength were transmitted over 5m of hollow-core PBGF. At the soliton formation energy, the output pulses had a length of less than 300fs and an output pulse energy of around 65nJ. The Raman-shifted solitons, which were almost bandwidth-limited, had a constant bandwidth of 3nm which is limited by the Raman spectrum of the gas inside the fibre. Numerical modelling shows that the nonlinear phase shift is determined by both the nonlinearity of air and by the overlap of the guided mode with the glass.

The cancellation of the soliton self-frequency shift in a silica-core photonic crystal fibre with a negative dispersion slope was demonstrated. The results show that stabilization of the soliton wavelength is accompanied by exponential growth of Cherenkov radiation emitted by the soliton. The compensate for the Raman frequency shift is attributed to the soliton spectral recoil from emitting the red-shifted radiation.

Acknowledgements

There are a lot of people I should thank for their help and support during my PhD. First of all, I would like to thank my supervisor, Jonathan Knight, for all the help, support, suggestions, ideas and the interest he has shown in my work during the last three years and four months.

I would like to acknowledge and thank Philip Russell for his supervision and for giving me the opportunity to study in the Optoelectronics Group at Bath.

Thanks must go to Alan George, Nicolas Joly, Geraud Bouwmans and the fabrication team from BlazePhotonics Ltd., for their great help in drawing the endless number of fibres, which are critical for this thesis.

To Tom Hedley, David Bird and Greg Pierce for their powerful codes which enabled me to carry out most of the numerical simulations shown in this thesis.

To Dmitry Skryabin, Tim Birks, Fabio Biancalana and William Wadsworth for very inspiring discussions.

To John Pottage for proof reading this thesis to make it readable.

To John Roberts and Fetah Benabid for all the good time together playing badminton and football, which is important to keep me fit.

To Greg Antonopoulos for being so supportive during the course of my PhD study, especially in the dreadful days of writing up.

In fact I would like to thank everyone in the Opto-group for making my PhD enjoyable.

Finally I would like to thank my wife, Langqin, for just being together happily.

Contents

List of Figures

List of Tables

List of publication

1. F Luan, AK George, TD Hedley, GJ Pearce, DM Bird, JC Knight and PSJ Ressell, "All solid photonic band-gap fiber", *Optics Lett.* 29(20) 2369-2371, OCT 2004

2. F Luan, JC Knight, PSJ Russell, S Campbell, D Xiao, DT Reid, BJ Mangan, DP Williams, and PJ Roberts, "Femtosecond soliton pulse delivery at 800nm wavelength in hollow-core photonic bandgap fibers", *Opt. Express* 12(5) 835-840, MAR 2004

3. DV Skryabin, F Luan, JC Knight, PSJ Russell, "Soliton self-frequency shift cancellation in photonic crystal fibers", *Science* 301 1705-1708, SEP 2003

4. G Bouwmans, F Luan, JC Knight, PSJ Russell, L Farr, BJ Mangan and H Sabert, "Properties of a hollow-core photonic bandgap fiber at 850 nm wavelength", *Opt. Express* 11(14) 1613-1620, JUL 2003

Chapter 1

Introduction

Modern optical fibres were one of the major technological successes of the 20th century. After the first low-loss (< 20dB/km) single-mode fibre in 1970, this technology has developed at an incredible pace. Now optical fibres have been the key components of not only our sophisticated global telecommunication network but also many non-telecom applications, such as beam delivery for medicine, machining and diagnostics, sensing and a host of other uses. After all the progress in technology, the basic physics of optical fibres has remained unchanged since the 19th century, and the remaining space for the improvement of optical fibre performance is very small. The loss of a single-mode fibre, which is as low as 0.15dB/km in the 1.55μm wavelength region, is limited mainly by the fundamental process of Rayleigh scattering. Although properties like optical nonlinearity and group-velocity dispersion can be influenced to a limited extent by fibre design, they are largely depending on the material's properties. It seemed that fibre optics had reached perfection until the birth of photonic crystal fibres.

Since the 1980s, optical physicists have recognized that the ability to structure materials on the scale of the optical wavelength, a fraction of a micrometre or less, will allow the development of new optical materials known as photonic crystals [1]. Photonic crystals rely on regular morphological microstructure incorporated into the material to radically alter its optical properties. When fibre optics embraced this new idea, a new breed of fibre was born. Such fibres are known as photonic crystal fibres (PCFs) [2][3], as they rely on the unusual properties of photonic crystal structures in the cladding to deliver previously unimaginable performance

from an optical fibre waveguide. Depending on the properties of the microstructure in the cladding, the fibres guide light with different mechanisms: modified total internal reflection (index-guiding PCFs) or band-gap guidance (photonic band-gap fibres(PBGFs)). Over the last few years, PCFs have already demonstrated some superior performances in several respects, which is leading to new phenomena and new applications, and they have greatly enriched the concepts of fibre optics.

This thesis gives a detailed description of the basic physics and properties of the new fibres, especially those guiding light by photonic band-gap guidance. Chapter 2 provides an overview of fibre optics, in which I discuss conventional fibres and index-guiding PCFs from a comparative point of view. Chapter 3 reviews some of the important progress that has been made regarding various photonic crystal fibres over the last few years. Chapters 4 to 7 present the new work done during the course of my PhD research. Chapter 4 describes the fabrication and characterisation of a new type of PCF: all solid PBGF, in which the band-gap guidance mechanisms is explained in detail. Chapter 5 describes the linear properties of a hollow-core PBGF. Chapter 6 demonstrates high power femtosecond soliton transmission by using a hollow-core PBGF. The origin of the nonlinearity and the characteristics of soliton behaviour in hollow-core fibre are discussed. Chapter 7 demonstrates the compensation of the soliton self-frequency shift (SSFS) by strong soliton Cherenkov radiation in an index-guiding PCF with engineered dispersion profile. Chapter 8 is the summary.

Chapter 2

Basics of optical fibres

This chapter briefly reviews the field of linear and nonlinear fibre optics. The first two sections outline the guidance mechanism, fundamental parameters and optical characteristics of conventional optical fibres and index-guiding photonic crystal fibres (PCFs). The third section briefly discusses the nonlinear fibre optics. The last section outlines the fabrication processes of conventional fibres.

2.1 Guiding mechanism

Modern optical fibre, born in the 1960s [4], normally consists of a central core surrounded by a cladding layer and then protected by a thick jacket. The index profile of a optical fibre, described generally by $n(x, y)$ as shown in Fig.2.1, does not change along the fibre axis (z). This translational invariance in the z direction leads to the most important conserved quantity in fibre optics, β, the propagation constant. β is the z component of the wavevector $n\vec{k_0}$, where n is the material index and $\vec{k_0}$ is the vacuum wavevector. Therefore β is always either equal to or smaller than the absolute value of the wavevector, i.e. $\beta \leq \vec{k_0}$. It is convenient to define the mode index $n_{mode} = \beta/k_0$.

The limited cross section area of an optical fibre makes all the possible values of β discretized. Each allowed β corresponds to a possible light distribution in the fibre and we call such a distribution a mode. Some modes are propagative in the core

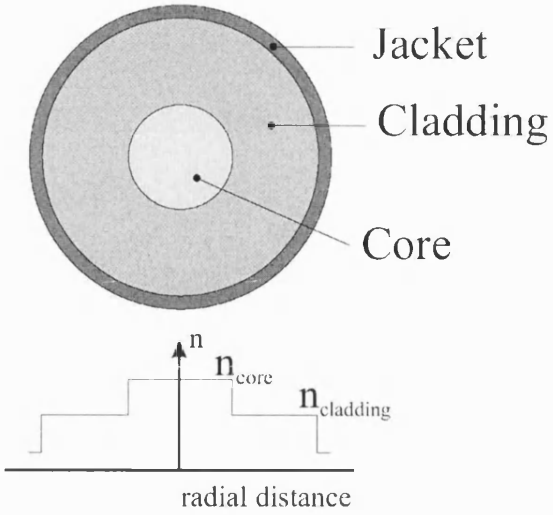

Figure 2.1: Schematic cross-sectional, index profile of a conventional step-index optical fibre

and evanescent in the cladding, and these are called core modes or guided modes. Core modes usually have low loss because they are isolated from the environment by the cladding layer. The others, that are not evanescent in the cladding, are called cladding modes, and these modes will experience high loss. Compared with the core, the size of the cladding is very big so the propagation constants of the cladding modes can be considered as continuous, and they therefore form a band. A core mode will inevitably couple into cladding modes if its propagation constant falls within a band of cladding modes. Therefore, the most important thing in fibre design is to make the desired core modes stand out from the cladding modes. There are two possible strategies to realize this, as illustrated in Fig.2.2. One is to make the core mode indices higher than the biggest mode index of the cladding, which is determined by the material and structure of the cladding. Both conventional fibres and index-guiding PCFs fall into this category. Another approach is to utilise band-gap effects, i.e. to divide the cladding modes into different bands and put core modes in the gap between the cladding mode bands. Photonic bandgap fibres belong to this latter category.

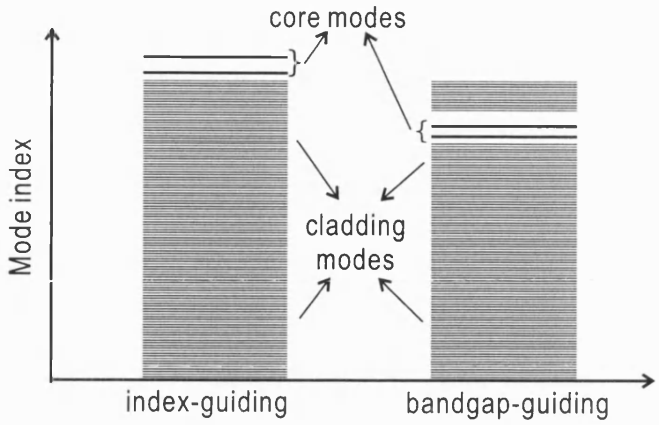

Figure 2.2: Two ways of making the desired core mode indices stand out from the cladding mode indices

2.1.1 Guidance mechanism of conventional fibre

In conventional fibre, the maximum cladding mode index is bounded above by the cladding material index, which must be lower than the core material index (Fig.2.3(a)). Under such conditions, there is at least one mode whose mode index is bigger than the material index of the cladding [5].

2.1.2 Guidance mechanism of index-guiding PCFs

In index-guiding PCFs, the maximum cladding mode index is reduced not by using different materials but having microstructure, usually air holes, in the cladding. The reduced cladding mode index is somewhere between the bulk material indices of silica and air, while the core area, normally formed by omitting one air hole in the centre, could support modes with mode indices higher than that of the cladding. A comparison of typical material index profile of a conventional fibre and an index-guiding PCF is shown in Fig.2.3. There is at least one core mode in both cases.

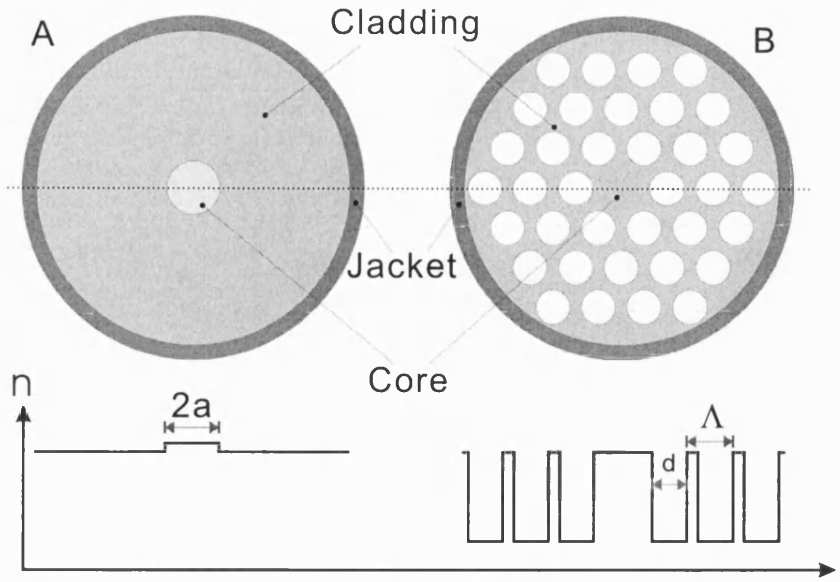

Figure 2.3: Comparison between (A) a conventional fibre and (B) an index-guiding PCF.

2.1.3 Single mode operation

The number of modes supported by the core is determined by several factors, including the index step between the core and the cladding, the size of the core and the wavelength. One can define a normalized parameter, called the V parameter, as a measure of the 'mode capacity' in a fibre. For a step index fibre, the V parameter is defined as [5]:

$$V = \frac{2\pi a}{\lambda}\sqrt{n_{core}^2 - n_{clad}^2} \tag{2.1}$$

where a is radius of the core, n_{core} and n_{clad} are the material index of the core and cladding respectively, and λ is is the free-space wavelength.

For index-guiding PCFs, the definition is quite similar [6]:

$$V = \frac{2\pi\Lambda}{\lambda}\sqrt{n_{core}^2 - n_{eff}^2} \tag{2.2}$$

where the effective index of the cladding n_{eff} , i.e. the maximum mode index of the cladding, is used instead of n_{clad} and the pitch Λ is used instead of radius of

the core whose boundary is not well defined in index-guiding PCFs. The bigger the V value, the more guided modes the fibre has. There is a critical value V_c for single mode operation. When $V < V_c$, the fibre will have only one core mode, in which case we call it a single mode fibre. For step index fibre $V_c = 2.405$, and for index-guiding PCFs $V_c = 4.1$ [7].

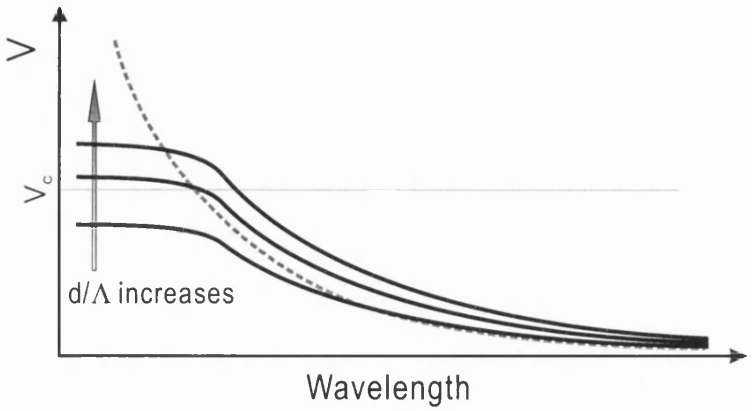

Figure 2.4: The V parameter is a function of wavelength. The dashed curve is for the conventional step index fibre. The solid curves are for index-guiding PCFs with different d/Λ. The V parameter increases as d/Λ increases.

Although Eq.2.1 and 2.2 have similar forms, the behaviour of the V parameter as a function of wavelength is quite different, which is shown in Fig.2.4. For step index fibre (the dashed curve in Fig.2.4), V is inversely proportional to wavelength. So for any single mode step index fibre, there is always a cut-off wavelength λ_c, below which the fibre will be multimode. However, for index-guiding PCFs, n_{eff} is strongly dependent on wavelength. In the long wavelength limit, n_{eff} approaches the average material index of the cladding structure and V descends to zero. In the short wavelength limit, light tends to avoid the hole areas and n_{eff} approaches to the material index of the glass, which is normally close to n_{core}. More detailed analysis [6][8] shows that V tends to a limiting value as the wavelength gets progressively shorter, which means there is a maximum V value. By proper design, for example by making $d/\Lambda < 0.45$ in the silica-air structure [6], we can make the maximum V value smaller than the critical value V_c and the fibre will then become "endlessly single mode". In the remainder of this thesis we will focus on single mode fibre or fibre with only few modes and discuss mainly the properties of the fundamental mode.

2.2 Linear properties of optical fibres

2.2.1 Losses

There are two main loss mechanisms in conventional optical fibres: absorption and radiation. The absorption losses are due to the interaction of the light with the material when propagating in the glass. The infrared absorption bands of silica and OH^- ions in the glass are the main contributors. Radiation losses are due to light in the guided mode coupling to the cladding (usually caused by perturbations such as micro and macro bending or discontinuities in the fibre structure). The biggest radiation loss contribution comes from Rayleigh scattering. This is an intrinsic problem of the fibre fabrication process, during which the fibre preform is heated over 2000^oC in the furnace. At the drawing temperature, silica is a liquid with lower viscosity, and has thermally excited density fluctuations. These density fluctuations are frozen into the fibre as it cools down. When working in the telecommunication window (around 1.55μm), the loss due to Rayleigh scattering in silica is 0.15dB/km and therefore, nowadays, accounts for the total loss of conventional optical fibre at that wavelength.

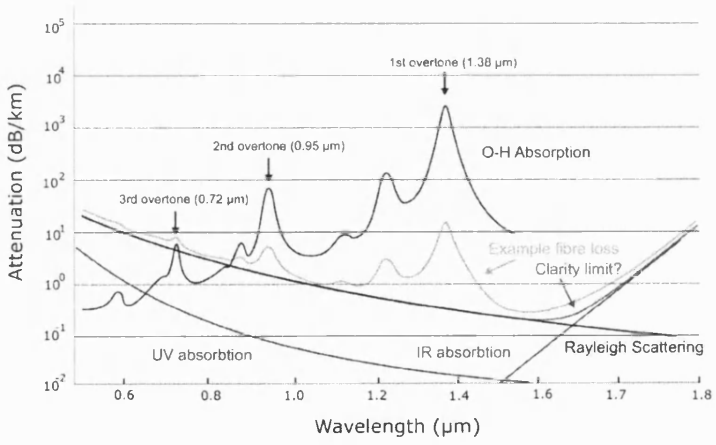

Figure 2.5: A schematic diagram showing various sources of loss in optical fibre.

There is a third type of loss — the confinement loss. Confinement loss in index-guiding PCFs arises mainly from the fact of not having an infinite structured cladding with effective index lower than the material index of the core. Unlike the case of conventional fibre where the core has the highest material index in

the whole structure, in most PCFs the jacketing material is pure silica or some other lower grade glass whose material index is not lower than that of the core. This means that in the jacketing layer there must be some modes whose mode indices are the same as or very close to the core mode index and the core mode can couple to these modes via the evanescent fields that exist in the cladding structure. Such coupling is the origin of the confinement loss. By making the cladding thicker to increase the physical displacement between the core and the jacket layer or increasing the air filing fraction to reduce the evanescent field in the cladding, we can reduce the confinement loss to the extent that it is much smaller than that due to the other loss mechanisms.

2.2.2 Geometric symmetry and Birefringence

The geometric symmetry of the index profile of the fibre causes some mode degeneracy, i.e. different field configurations share the same propagation constant β and any linear combination of these modes is still a possible mode with the same β. For example, the fundamental mode of a circularly symmetric fibre, such as conventional step-index fibre, consists of a pair of linearly polarized degenerate modes which have identical field intensity distributions but perpendicular polarizations. It means that the fundamental mode of such a fibre could be any polarization, which can be seen as a certain linear combination of the two linearly polarized degenerate modes.

A typical index-guiding PCF, as shown in Fig.2.3(b), has 6-fold rotational symmetry. However such reduced rotational symmetry does not separate the two linear polarized degenerate fundamental modes [9]. From Fig.2.6 we can see that the rotation operations give us three degenerate linearly polarized modes and by combining two of them we can compose another degenerate linearly polarized mode which is perpendicular to the third one. In fact, any index profile with rotational symmetry greater than 2-fold will have degenerate linearly polarized modes.

In reality, the index profiles of fibres are not perfectly symmetrical and any deviation from perfect symmetry will cause coupling between degenerate modes. For conventional fibre, very small imperfections are distributed along the fibre in a random way, so the polarization at the output will be random no matter

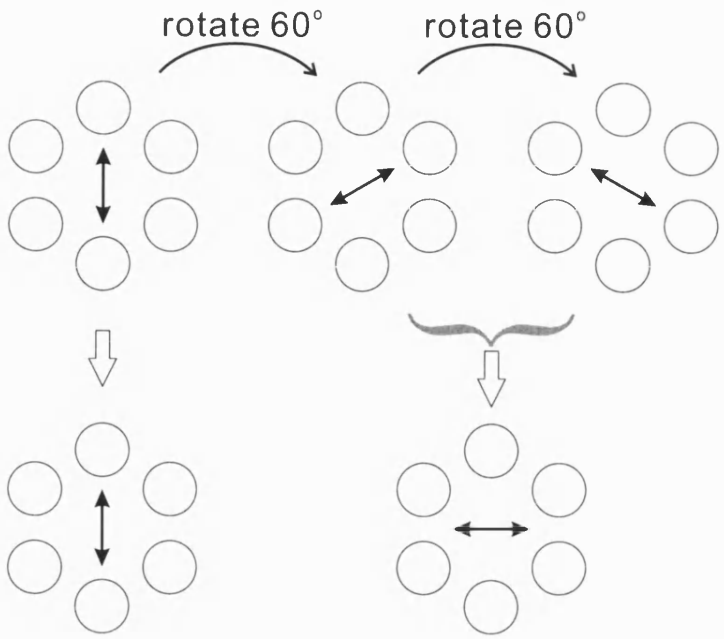

Figure 2.6: Polarisation degeneracy induced by rotational symmetry in PCFs

what the input is. For photonic crystal fibres, the structural imperfections are a result of the stack-and-draw process and are instead fixed along the fibre length. Such uniform asymmetry gives the fibre some birefringence, which means that the fundamental mode splits into two polarized modes along the two orthogonal axes (normally denoted as x, y) and they have slightly different propagation constants β_x and β_y. That is the reason why all PCFs have a certain level of birefringence. Input light with polarization other than x or y is no longer a mode of the fibre and its polarization state changes continuously along the fibre in a periodic manner with period equal to :

$$L_B = \frac{2\pi}{|\beta_x - \beta_y|} \tag{2.3}$$

The polarization beat length, L_B, is a measure of the birefringence. Fibre with short L_B, corresponding to strong birefringence, is called polarization maintaining fibre (PMF) or highly birefringent (HiBi) fibre. Very high birefringence can be obtained in index-guiding PCF by suitably designing the microstructured cladding.

2.2.3 Dispersion

The propagation constant β is a function of ω, known as the dispersion relation. Dispersion plays a critical role in the propagation of short pulses and all kinds of nonlinear processes in fibres. For a monochromatic wave propagating in an optical fibre, only the phase changes along the fibre and the intensity is constant. The phase can be written as $e^{i(\beta z-\omega t)}$ and the phase change propagates with speed ω/β. However, the absolute phase has little physical meaning because it cannot be measured. The important thing is the phase difference. For example, considering two equal amplitude monochromatic waves with different frequencies ω_1 and ω_2 propagating in the same direction in a fibre, there will be intensity modulation because of the interference between the two waves. The intensity modulation has the form of $cos(\Delta\beta z - \Delta\omega t)$ and it propagates at a speed of $\Delta\omega/\Delta\beta$, where $\Delta\omega = \omega_1 - \omega_2$ and $\Delta\beta = \beta_1 - \beta_2$. In reality optical signals, usually pulses, are often composed of a group of frequencies very close to each other around a central frequency ω_0 and travel at a speed of $\left(\frac{d\omega}{d\beta}\right)_{\omega=\omega_0}$, called the group velocity. If the group velocity did not change with frequency, optical signals would travel along the fibre without distortion. However, the group velocity does change with wavelength. By expanding the propagation constant β in a Taylor series about the central frequency ω_0, we can write a mathematical expression of the dispersion:

$$\beta(\omega) = n(\omega)\omega/c = \beta_0 + \beta_1(\omega - \omega_0) + \frac{1}{2}\beta_2(\omega - \omega_0)^2 + \cdots \tag{2.4}$$

where

$$\beta_m = \left(\frac{d^m\beta}{d\omega^m}\right)_{\omega=\omega_0} \tag{2.5}$$

and among them:

$$\beta_1 = \frac{d\beta}{d\omega} = \frac{1}{v_g} = \frac{n_g}{c} = \frac{1}{c}\left(n + \omega\frac{dn}{d\omega}\right) \tag{2.6}$$

$$\beta_2 = \frac{d\frac{1}{v_g}}{d\omega} = \frac{1}{c}\left(2\frac{dn}{d\omega} + \omega\frac{d^2n}{d\omega^2}\right) \tag{2.7}$$

Here it is clear that β_1 is inversely proportional to the group velocity v_g and β_2, called the group velocity dispersion (GVD), is related to the group velocity change with frequency. Likewise, β_3, β_4, etc. reflect higher-order GVD and we call them 3rd-order dispersion, 4th-order dispersion and so on. In practice, it is

more convenient to use the parameter $D \equiv \frac{d\beta_1}{d\lambda}$ to describe the dispersion as a function of wavelength. D usually has units of ps/nm/km, and is related to β_2 by:

$$D = -\frac{2\pi c}{\lambda^2}\beta_2 \tag{2.8}$$

Dispersion in single mode fibre has contributions from mainly two sources. One is the dispersion caused by the bulk materials of core and cladding (called material dispersion), and the other is the dispersion induced by the slight change in the confinement of light in the core as the wavelength changes (called waveguide or geometric dispersion).

As the material dispersion is rather fixed, the easiest way of controlling the dispersion is through engineering the waveguide dispersion. In conventional fibre this is achieved by choosing appropriate core radii and the index step or by introducing other layers around the core. Fig.2.7 shows one such example, a dispersion flattened fibre formed by adding a low index layer around the core (known as 'W' fibre).

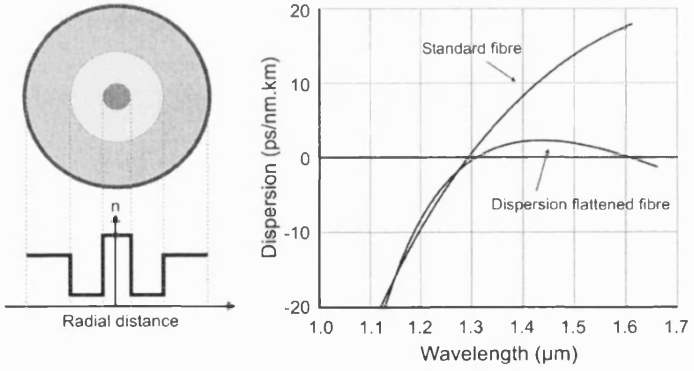

Figure 2.7: A schematic of a dispersion flattened 'W-fibre' and example dispersion profiles of standard and dispersion flattened fibres.

2.3 Nonlinear properties

The response of any dielectric material to light becomes nonlinear for high intensities, and optical fibres are no exception. This chapter is intended to be a

brief summary of some of the main concepts in nonlinear fibre optics, which have been studied and summarized in detail in '*NonlinearFiberOptics*' by Govind P. Agrawal [10].

In the following text, we assume the optical field is linearly polarized and maintains its polarization along the fibre, which is true in polarization-maintaining fibres. Also we assume that the optical field is quasi-monochromatic, i.e. the spectral width $\Delta\omega$ (usually related to the pulse length) is much smaller than the central frequency ω_0. This assumption is valid for optical pulses as short as tens of femtoseconds.

2.3.1 Origin of optical nonlinearities in materials

The response of a dielectric medium to an applied electric field $\vec{E}(\vec{r},t)$ can be described by the polarization vector $\vec{P}(\vec{r},t)$. If we assume the response is instantaneous, the polarization vector can be generally expressed as [11]:

$$\vec{P} = \epsilon_0(\chi^{(1)} \cdot \vec{E} + \chi^{(2)} : \vec{E}\vec{E} + \chi^{(3)} \vdots \vec{E}\vec{E}\vec{E} + \cdots) \tag{2.9}$$

where $\chi^{(1)}$ is the linear susceptibility of the medium and is related to the refractive index n by $n^2 = \epsilon = 1 + \chi^{(1)}$. The quantity $\chi^{(j)}$ $(j > 1)$, the nonlinear susceptibility, is a tensor of rank $j+1$ and has $3j+1$ complex components. They describe the nonlinear-optical properties of the medium. In order to avoid some of the complexities of the polarization vector, in what follows we shall make some assumptions and focus on certain material systems.

In silica, $\chi^{(2)}$ vanishes because of the inversion symmetry of the molecular structure. If we consider only the lowest order nonlinearity, then the response of silica to linearly polarized light can be simply written as:

$$P = \epsilon_0(\chi^{(1)}E + \chi^{(3)}E^3) = P_L + P_{NL} \tag{2.10}$$

where $P_{NL} = \epsilon_0\chi^{(3)}E^3$ is the nonlinear response of the silica to the applied field. P_{NL} is related to a refractive index change by:

$$\Delta n = \frac{\epsilon_{NL}}{2n} \tag{2.11}$$

where

$$P_{NL}(\vec{r},t) = \epsilon_0 \epsilon_{NL} E(\vec{r},t)$$

Under the quasi-monochromatic assumption, a linearly polarized light pulse with central frequency ω_0 can be expressed as:

$$\vec{E}(\vec{r},t) = \frac{1}{2}\hat{x}[E(\vec{r},t)e^{i(\beta(\omega_0)z-\omega_0 t)} + c.c.] \tag{2.12}$$

where $E(\vec{r},t)$ is a slowly varying function of time (relative to the optical phase $e^{i\omega_0 t}$). If two optical fields with different frequencies ω_1 and ω_2 interact with each other via $\chi^{(3)}$, we can find that P_{NL} not only has the components with frequencies ω_1 and ω_2, but also has new frequencies at $2\omega_1 \pm \omega_2$, $2\omega_2 \pm \omega_1$, $3\omega_1$, $3\omega_2$. They are:

$$P_{NL}^{\omega_1} = \frac{3\epsilon_0}{4}\chi^{(3)}(|E_1|^2 + 2|E_2|^2)\frac{1}{2}(E_1 e^{i(\beta_1 z-\omega_1 t)} + c.c.) \tag{2.13a}$$

$$P_{NL}^{\omega_2} = \frac{3\epsilon_0}{4}\chi^{(3)}(|E_2|^2 + 2|E_1|^2)\frac{1}{2}(E_2 e^{i(\beta_2 z-\omega_2 t)} + c.c.) \tag{2.13b}$$

$$P_{NL}^{2\omega_1-\omega_2} = \frac{3\epsilon_0}{4}\chi^{(3)}\frac{1}{2}(E_1^2 E_2^* e^{i[(2\beta_1-\beta_2)z-(2\omega_1-\omega_2)t]} + c.c.) \tag{2.13c}$$

$$P_{NL}^{2\omega_2-\omega_1} = \frac{3\epsilon_0}{4}\chi^{(3)}\frac{1}{2}(E_2^2 E_1^* e^{i[(2\beta_2-\beta_1)z-(2\omega_2-\omega_1)t]} + c.c.) \tag{2.13d}$$

$$P_{NL}^{2\omega_1+\omega_2} = \frac{3\epsilon_0}{4}\chi^{(3)}\frac{1}{2}(E_1^2 E_2 e^{i[(2\beta_1+\beta_2)z-(2\omega_1+\omega_2)t]} + c.c.) \tag{2.13e}$$

$$P_{NL}^{2\omega_2+\omega_1} = \frac{3\epsilon_0}{4}\chi^{(3)}\frac{1}{2}(E_2^2 E_1 e^{i[(2\beta_2+\beta_1)z-(2\omega_2+\omega_1)t]} + c.c.) \tag{2.13f}$$

$$P_{NL}^{3\omega_1} = \frac{\epsilon_0}{4}\chi^{(3)}\frac{1}{2}(E_1^3 e^{i(3\beta_1 z-3\omega_1 t)} + c.c.) \tag{2.13g}$$

$$P_{NL}^{3\omega_2} = \frac{\epsilon_0}{4}\chi^{(3)}\frac{1}{2}(E_2^3 e^{i(3\beta_2 z-3\omega_2 t)} + c.c.) \tag{2.13h}$$

In fibres, the phase of the field cannot be arbitrary and has to satisfy the dispersion relation $\beta(\omega)$. It is clear that the phase of the field $P_{NL}^{\omega_j}$ $(j = 1, 2)$ satisfies the dispersion relation automatically, while for other new frequency components, the dispersion relation is generally not satisfied except in some special cases. For example, the phase of $P_{NL}^{2\omega_1-\omega_2}$ is $e^{i[(2\beta(\omega_1)-\beta(\omega_2))z-(2\omega_1-\omega_2)t]}$ and the dispersion relation is satisfied only at some special points where $2\beta(\omega_1) - \beta(\omega_2) = \beta(2\omega_1 - \omega_2)$ is true. This condition is called the phase matching condition, which is critical to some nonlinear processes.

2.3.2 Pulse propagation in fibre

Because the field distribution changes little as pulses propagate in a fibre, it is useful to separate the mode profile and pulse profile, by writing the light field in the form:

$$\vec{E}(\vec{r},t) = \frac{1}{2}\hat{x}[F(x,y)A(z,t)e^{i(\beta_0 z-\omega_0 t)} + c.c.] \tag{2.14}$$

where $F(x,y)$ is the field distribution in the cross section of the fibre, $A(z,t)$ is the slowly varying pulse envelope, ω_0 is the central frequency and $\beta_0 = \beta(\omega_0)$. In frequency space, Equ.2.14 becomes:

$$\tilde{E}(\vec{r},\omega) = F(x,y)\tilde{A}(z,\omega)e^{i\beta_0 z} \tag{2.15}$$

Here we assume that $F(x,y)$ does not depend on frequency because the change of field distribution within a small frequency range is negligible. At a single frequency, the z dependence of the electric field is only a phase change, i.e.

$$\frac{\partial \tilde{E}}{\partial z} = i\beta(\omega)\tilde{E} \tag{2.16}$$

By substituting Equ.2.15 into Equ.2.16 we have:

$$\frac{\partial \tilde{A}(z,\omega)}{\partial z} = i[\beta(\omega) - \beta_0]\tilde{A}(z,\omega) \tag{2.17}$$

Up to now we have not taken into account any nonlinear effects in the pulse propagation equation. Equ.2.11 related P_{NL} with a small index change Δn, which will change the propagation constant β by:

$$\Delta\beta = \frac{k_0 \iint_{-\infty}^{\infty} \Delta n\,|F(x,y)|^2\,dxdy}{\iint_{-\infty}^{\infty} |F(x,y)|^2\,dxdy} = k_0 \iint_{-\infty}^{\infty} \Delta n\,|F(x,y)|^2\,dxdy \tag{2.18}$$

where we assume $F(x,y)$, the field profile, is normalized, i.e.

$$\iint_{-\infty}^{\infty} |F(x,y)|^2\,dxdy = 1$$

Taking into account the nonlinear contribution, the propagation constant becomes $\beta(\omega) + \Delta\beta$. Then Equ.2.17 becomes:

$$\frac{\partial \tilde{A}(z,\omega)}{\partial z} = i[\beta(\omega) + \Delta\beta - \beta_0]\tilde{A}(z,\omega) \tag{2.19}$$

It is often easier to express Equ.2.19 in the time domain, because the Fourier transform of $\Delta\beta$ is quite complex. Using the Taylor series of $\beta(\omega)$ and replacing $(\omega - \omega_0)^m$ by the differential operator $i^m(\partial^m/\partial t^m)$, we get:

$$\frac{\partial A(z,T)}{\partial z} - i\sum_{m=2}^{\infty}\frac{i^m\beta_m}{m!}\frac{\partial^m A(z,T)}{\partial T^m} = i\Delta\beta A(z,T) \tag{2.20}$$

where a frame of reference moving with the pulse at the group velocity v_g is used by making the transformation:

$$T \equiv t - z/v_g = t - \beta_1 z \tag{2.21}$$

In practise, only a limited numbers of dispersion terms are retained and we write out $\Delta\beta$ by using Equ.2.13 and Equ.2.18. For example, if we consider a single pulse (carrier frequency ω_0) in a fibre, P_{NL} only contains $P_{NL}^{\omega_0}$ and $P_{NL}^{3\omega_0}$. $P_{NL}^{3\omega_0}$ can be neglected because the phase-matching condition is generally not satisfied. Then we can write Δn as:

$$\Delta n = \frac{3}{8n}\chi^{(3)}\left|E(\vec{r},t)\right|^2 = \frac{3}{8n}\chi^{(3)}\left|F(x,y)A(z,t)\right|^2 \tag{2.22}$$

Then from Equ.2.18, $\Delta\beta$ is:

$$\Delta\beta = \frac{3k_0}{8n}\chi^{(3)}\left|A(z,t)\right|^2\iint_{-\infty}^{\infty}\left|F(x,y)\right|^4 dxdy = \gamma\left|A(z,t)\right|^2 \tag{2.23}$$

where the nonlinear parameter γ is defined as:

$$\gamma = \frac{n_2\omega_0}{cA_{eff}};\quad n_2 = \frac{3}{8n}\chi^{(3)};\quad A_{eff} = \frac{1}{\iint_{-\infty}^{\infty}\left|F(x,y)\right|^4 dxdy} \tag{2.24}$$

If $F(x,y)$ is approximated by a normalised Gaussian distribution $F(x,y) = \frac{1}{w}\sqrt{\frac{2}{\pi}}e^{-(x^2+y^2)/w^2}$ (for single mode fibre $w \approx$ core radius), then $A_{eff} = \pi w^2$ and it is called the effective-area. Typically, for conventional fibre A_{eff} can vary in the range of 20-100μm^2 in the 1.5μm region. As a result, γ takes values in the range of 1-10/W/km if we set the n_2 for silica at about $2.2 \times 10^{-20}\mathrm{m}^2/\mathrm{W}$ [12].

Using Equ.2.20 and 2.23 and neglecting the fibre dispersion higher than third-order, we will have:

$$\frac{\partial A}{\partial z} + \frac{i\beta_2}{2}\frac{\partial^2 A}{\partial T^2} - \frac{\beta_3}{6}\frac{\partial^3 A}{\partial T^3} = i\gamma\left|A\right|^2 A \tag{2.25}$$

By solving this equation numerically, we can predict the behaviour of the pulse propagating in a fibre under appropriate approximations. In the following text, we briefly describe different nonlinear effects and dispersion effects separately.

2.3.3 Group velocity dispersion (GVD) effect

When β_2 is dominant and nonlinearity is negligible, from Equ.2.17, we get:

$$\tilde{A}(z,\omega) = \tilde{A}(0,\omega)e^{i\beta_2\omega^2 z/2} \tag{2.26}$$

where $\tilde{A}(0,\omega) = \int_{-\infty}^{\infty} A(0,T)e^{i\omega T}dT$. Group velocity dispersion is purely a linear effect, which means there is no coupling between different frequency components. Therefore, as the pulse propagate along the fibre, the spectrum is unchanged, i.e.$\left|\tilde{A}(0,\omega)\right| = \left|\tilde{A}(z,\omega)\right|$. But the relative phases between the different frequency components will be changed as a result of a difference in group velocity, which will deform the pulse shape (in time). When $\beta_2 > 0$, called normal dispersion, low frequency components travel faster. When $\beta_2 < 0$, called anomalous dispersion, high frequency components travel faster.

The dispersion length, $L_D = T_0^2/|\beta_2|$, is as a measure of the GVD effects on a pulse with pulse length T_0, which is related to the FWHM by $T_{FWHM} = \eta T_0$. η is a pulse shape related constant (for Gaussian pulses $\eta \approx 1.665$, for Hyperbolic-Secant pulses $\eta \approx 1.763$). Dispersion effects become important when fibre length $> L_D$.

2.3.4 Self-phase modulation (SPM)

If we neglect GVD effects, from Equ.2.25 we will have:

$$\frac{\partial A(z,T)}{\partial z} = i\gamma\left|A(z,T)\right|^2 A(z,T) \tag{2.27}$$

We can see that as the pulse propagates along the fibre, it only acquires a time related phase and as a result the pulse shape is unchanged, i.e.$|A(0,T)| = |A(z,T)|$.

So Equ.2.27 becomes:

$$\frac{\partial A(z,T)}{\partial z} = i\gamma \left|A(0,T)\right|^2 A(z,T) \tag{2.28}$$

and its solution is:

$$A(z,T) = A(0,T)e^{i\phi_{NL}(z,T)} \tag{2.29}$$

where $\phi_{NL}(z,T) = \gamma \left|A(0,T)\right|^2 z$ is called the nonlinear phase shift. For a given length L, the maximum nonlinear phase shift is given by $\phi_{max} = \gamma P_0 L$, where $P_0 = \left|A(0,T)\right|^2_{max}$ is the peak power. The time dependence of the nonlinear phase shift results in a frequency shift $\delta\omega$ given by:

$$\delta\omega(T) = -\frac{\partial\phi_{NL}}{\partial T} = -\gamma L \frac{\partial \left|A(0,T)\right|^2}{\partial T} \tag{2.30}$$

This frequency shift is related to the pulse shape. At the pulse front, $|A(0,T)|$ has a positive slope over time, so there is a red shift. One the contrary, there is a blue shift at the pulse tail.

The nonlinear length is defined to be $L_{NL} = \frac{1}{\gamma P_0}$, and it is a measure of the extent of the nonlinear effects, which can be neglected when the fibre length $<< L_{NL}$.

2.3.5 Soliton effects

From the sections above, we know that: the GVD effects are time shifts of different frequency components while keeping the spectrum unchanged; the SPM effects are frequency shifts at different times while keeping the pulse shape unchanged. When both GVD and SPM are present in the fibre, which is more realistic, the joint effects can result in a stable pulse solution, called an optical soliton, whose shape and spectrum are both unchanged during the propagation.

If we only consider SPM and the lowest order of GVD effects, the pulse propagation equation becomes:

$$\frac{\partial A}{\partial z} + \frac{i\beta_2}{2}\frac{\partial^2 A}{\partial T^2} = i\gamma \left|A\right|^2 A \tag{2.31}$$

If at $z = 0$, we put a pulse into a fibre with anomalous GVD ($\beta_2 < 0$) and the

pulse has the form of:

$$A(0,T) = \sqrt{P_0} sech(T/T_0) \tag{2.32}$$

where the parameter P_0 (the peak power) and $T_0 (= 1.763 T_{FWHM})$ are chosen such that N, whose definition is:

$$N = \sqrt{\frac{L_D}{L_{NL}}} = \left(\frac{\gamma P_0 T_0^2}{|\beta_2|}\right)^{1/2} \tag{2.33}$$

is a integer, we find that when $N \geq 2$ as the pulse propagates along the fibre, both the shape and spectrum of the pulse will evolve periodically with a period of:

$$z_0 = \frac{\pi}{2} L_D = \frac{\pi}{2} \frac{T_0^2}{|\beta_2|} \tag{2.34}$$

These periodically evolving pulses are called Nth-order solitons. The situation for $N = 1$ (called a fundamental soliton) is exceptionally simple. Nothing, except for a collective phase, will change as the pulse propagates, i.e.:

$$A(z,T) = \sqrt{P_0} sech(T/T_0) exp(i\frac{z}{2L_D}) = \sqrt{P_0} sech(T/T_0) exp(i\gamma P z/2) \tag{2.35}$$

2.3.6 Stimulated inelastic scattering processes

The nonlinear effects governed by the third-order susceptibility $\chi^{(3)}$ are elastic in the sense that no energy is exchanged between the light field and the dielectric medium. A second class of nonlinear effects results from stimulated inelastic scattering in which the optical field transfer part of its energy to the nonlinear medium. Two important nonlinear effects in optical fibres fall in this category. Both of them are related to vibrational excitation modes of silica. These phenomena are known as stimulated Raman scattering (SRS) and stimulated Brillouin scattering (SBS). The main difference between the two is that optical phonons participate in SRS while acoustic phonons participate in SBS.

Raman scattering is a spontaneous effect in which a small fraction of the power of an optical field is transferred (via optical phonons, molecular excitations accompanied by dipole oscillations) to another field whose frequency is red-shifted by an amount determined by the vibrational modes of the medium. The photons can be scattered as well to higher frequencies. When the scattered photon frequency is lower than the pump frequency, this is referred to as a Stokes wave, and

the frequency is blue-shifted it is referred to as an anti-Stokes wave. When an intense pump is present, this effect becomes stimulated and an exponential growth of the Stokes band occurs. Then, it is called stimulated Raman scattering (SRS). One of the SRS effects is soliton self-frequency shift (SSFS) which was observed in 1986 [13]. When the spectrum width of the soliton is large enough (this is usually true for pulse width T_0 <1ps), the Raman gain can amplify the low-frequency components of the soliton with high-frequency components of the same soliton acting as a pump. Then the soliton experiences a continuous red-shift as it propagates along the fibre. When higher-order dispersions are neglected, the frequency shift $\Delta\omega_R$ of the soliton can be expressed as [10]:

$$\Delta\omega_R(z) = -\frac{8|\beta_2|T_R z}{15T_0^4} \tag{2.36}$$

where $T_R \approx$ 3fs (for silica) can be related to the Raman gain property within the spectrum width of the soliton [14]. Although SSFS has been considered an immutable feature of sub-picosecond solitons in silica fibres, in Chapter7 I will demonstrate the compensation of SSFS in an index-guiding PCF with a negative GVD slope.

Brillouin scattering is very similar to Raman scattering. The difference resides in the fact that the energy and momentum transfer takes place via acoustic phonons (molecular excitations not accompanied by dipole oscillations) but not optical phonons as with Raman scattering. Therefore, Brillouin scattering is due to light scattered by acoustic waves.

2.4 Fabrication methods for conventional fibre

There are two ways to manufacture optical glass fibre: either by directly drawing the fibre from molten glasses, which are placed in two concentric crucibles (Double Crucible method [15]), or from a glass rod called a preform. Nowadays most optical fibres are made from preforms. There are two steps in the preform based fibre fabrication process. First, a preform with the desired refractive index contrast and geometrical profile is made. Then the perform is drawn into fibre. Although the fibre drawing process varies little, the processes of making the preforms are dramatically different. In this section we describe briefly two optical

glass fibre manufacturing processes, rod-in-tube and modified chemical vapour deposition (MCVD).

2.4.1 Rod-in-tube method

The first conventional step-index optical fibres were produced using the rod-in-tube method of fabrication. To make fibres by this method, we insert a glass rod with high refractive index into a glass tube with lower refractive index and heat them so that the tube melts onto the rod, forming a thicker solid rod called a preform. This preform is then pulled down to fibre. This process is shown schematically in Fig.2.8.

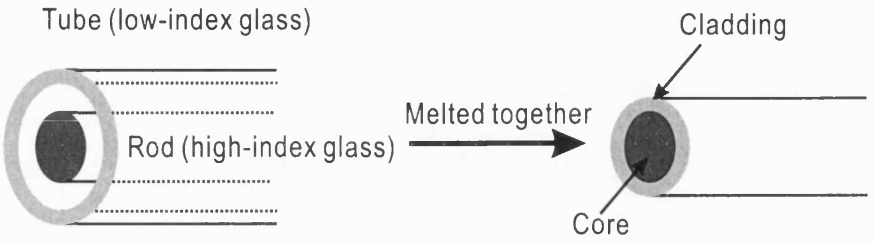

Figure 2.8: Schematic of preform fabrication process with rod in tube method.

To reduce the fibre transmission loss, the core-cladding interface must be very clean and smooth. This requires that the external surface of the rod and the internal surface of the tube be thermally or chemically polished to remove any surface roughness. Mechanical polishing cannot be used because, though giving a surface that looks smooth to the eye, it is in fact covered in tiny scratches and cracks, and some polishing debris may remain after cleaning. If the core-cladding interface is contaminated in any way, light scattering will occur, degrading transmission. Fibres produced by this method usually have high attenuation and are used for short-distance image transmission and illumination.

2.4.2 Chemical-vapour deposition

The MCVD process [16] is based on the high temperature oxidation of reagents inside a rotating tube which is heated by an external heat source. A schematic of the process is shown in Fig.2.9. Chemical reagents are first entrained in a gas stream in controlled amounts by either passing carrier gases such as O_2, Ar, or He through liquid dopant sources, or by using gaseous dopants. Halides which have reasonably high vapor pressures at room temperature are typically used and include $SiCl_4, SiF_4, GeCl_4, BCl_3, BBr_3, PCl_3$ and $POCl_3$.

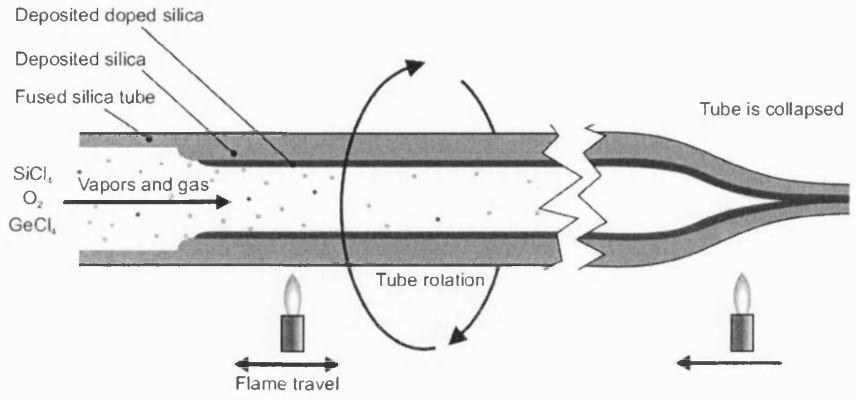

Figure 2.9: Schematic of the procedure for fabricating a conventional optical fibre preform by modified chemical vapor deposition (MCVD).

The high purity gas mixture is injected into a rotating tube which is mounted in a glass working lathe and heated by a traversing oxyhydrogen torch in the same direction as the gas flow. The reagents react by a homogeneous gas phase reaction at high temperatures to form glassy particles which are subsequently deposited downstream of the hot zone. The heat from the moving torch fuses the material to form a transparent glassy film. Typical deposition temperatures are sufficiently high to sinter the deposited material, but not so high as to cause distortions of the substrate tube. The torch is traversed repeatedly in order to build up, layer by layer, the desired amount of material. In practice, a thin cladding layer is first deposited. This serves as a barrier to the diffusion of any impurities, such as OH^-, which could increase the optical attenuation. After the cladding is deposited, the core material is laid down by adding index-raising dopants, such as $GeCl_4$ and PCl_3, with a programmed chemical delivery rate.

The main chemical reactions in the hot tube are:

$$SiCl_4 + O_2 \overset{>1300^oC}{\rightarrow} SiO_2 + 2Cl_2 \quad (2.37)$$

$$GeCl_4 + O_2 \overset{>1300^oC}{\rightarrow} GeO_2 + 2Cl_2 \quad (2.38)$$

Following deposition, the tube and deposit are collapsed to a solid rod called a preform by heating to temperatures sufficient to soften the substrate tube. The preform is then transferred to a fibre drawing apparatus where it is drawn and coated. The structure of the fibre closely replicates the perform.

2.4.3 Fibre drawing process

Fibre is formed from a preform by the drawing process on a fibre tower, which is illustrated in Fig.2.10. The preform is fed from the top of the tower into the furnace with a low speed, usually several mm/min, and pulled at the bottom of the tower with a speed of several m/sec. The furnace comprises a water-cooled jacket that surrounds an electrically heated graphite element. The furnace chamber is purged with purified argon whilst irises at the furnace entry and exit prevent any atmospheric or other contamination from taking place. Glass drawing temperatures used are typically between 1800^oC and 2100^oC. The final diameter of the fibre is determined by the ratio of the feeding to the pulling speed. Once the fibre has left the furnace, the dimensions and position of the fibre are monitored continuously by means of lasers to control the pulling speed via a feedback loop which in turn corrects for any diameter fluctuations. Freshly drawn fibre has a very high strength, which rapidly degrades unless action is taken to exclude the external atmosphere and avoid mechanical damage. Because of this, coatings of polymer are applied after the diameter monitor. The polymer is applied to the fibre via a polymer-coating die as a liquid, and this liquid is cured usually by ultraviolet radiation.

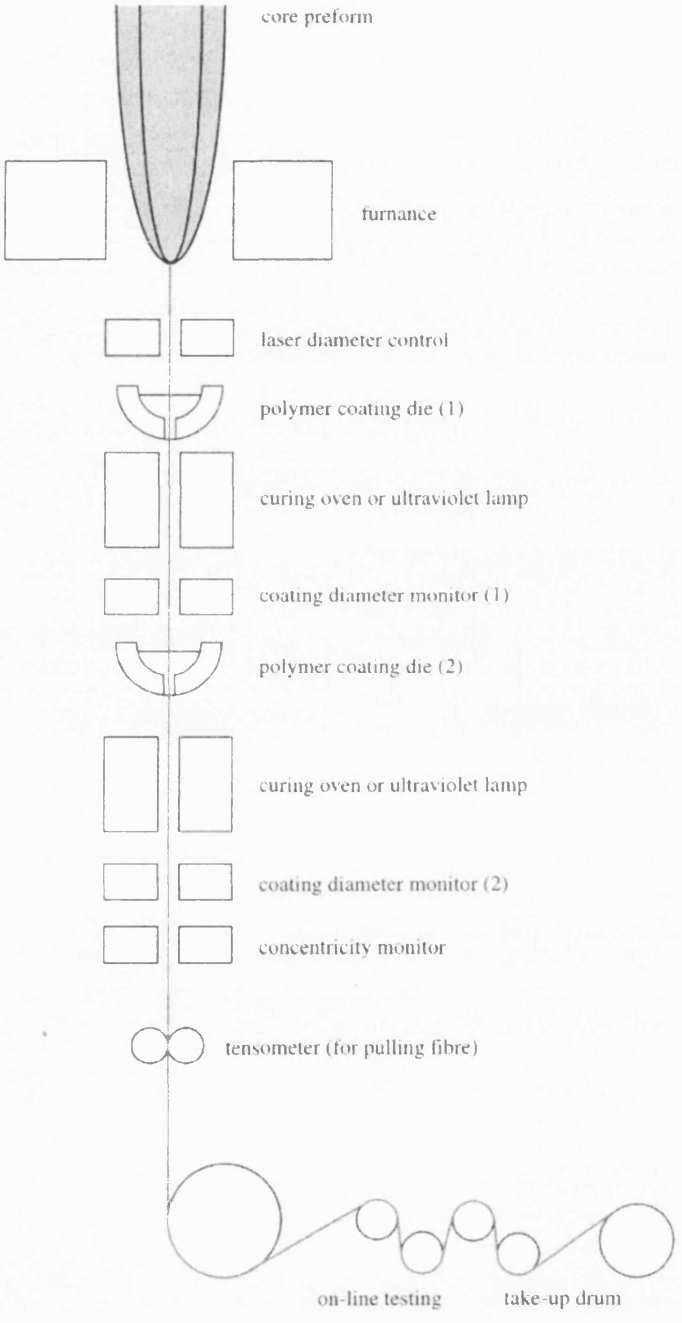

Figure 2.10: A schematic diagram of the fibre-pulling process.

Chapter 3

Progress on photonic crystal fibres

After the first demonstration of index guiding PCF [17], photonic crystal fibre has attracted great research interest from all over the world. In this Chapter, we will review the major progresses in both index guiding PCFs and band-gap fibres, following a description of the fabrication methods used in making PCFs.

3.1 Fabrication process for PCFs

3.1.1 Stack and draw

The commonest method to fabricate silica-air microstructured fibres is the stack and draw process [17], as shown in Fig. 3.1. Unlike conventional fibre fabrication shown in Chapter 2, PCF fabrication starts with a stack that is perhaps 20mm in diameter and a metre in length, formed by stacking a number of capillary silica tubes and rods to form the desired air-silica structure. The finished stack is drawn into meter-long preforms with a diameter range from several millimetres to several centimetres. After the desired preform is constructed, it is drawn into fibre on a conventional drawing tower (Fig.2.10), and hair-thin photonic crystal fibres are readily produced in kilometre lengths. Through careful process control,

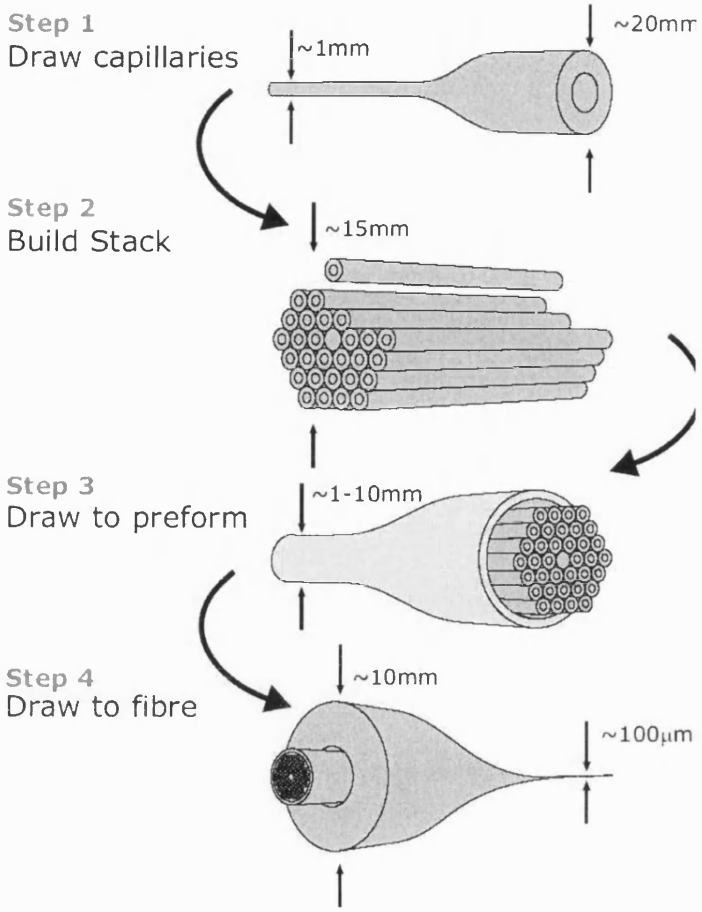

Figure 3.1: The basic stack and draw PCF fabrication technique. Silica capillaries and rods are stacked into a hexagonal array, and progressively reduced in diameter until the structure has the required wave guiding characteristics.

the air holes retain their arrangement all through the drawing process and even fibres with very complex designs and high air filling fraction can be produced.

In the drawing process, many factors should be carefully controlled to get the ideal structure. Among these factors, the draw down ratio, the drawing temperature, the drawing speed and the pressure applied on the preform are the most important ones.

This method has its advantages as well as disadvantages. The advantages include: the facilities designed for conventional fibres are ready to use with little changes; no doping process is involved; and it is straightforward to make long lengths of uniform structured fibres. The disadvantages include: the contaminations in the

stacking process could make the final fibre lossy, and the complexity of the fibre profile is limited by the stacking process.

3.1.2 Extrusion

The photonic crystal fibre concept not only gives us extra freedom in fibre design but also makes it possible to make fibres from a wide range of materials other than silica-based glass. Recently, PCFs drawn from other glasses [18][19][20], plastics [21] and polymers [22][23] have been reported. In most of these demonstrations, extrusion technology is employed because fabrication by the stack-and-draw process is not suitable for such a variety of materials due often to their limited availability, high cost (stack-and-draw typically uses large quantities of glass) or inconvenient thermal properties. Extrusion is now a well-known process in the technology of metals and plastics, for the manufacture of rods, tubes and other more complex profiles. The basic principle of extrusion is as simple as squeezing toothpaste out of a tube, where pressure applied to the closed end of the tube forces the paste to flow through the open end. The continuous shape, or profile, of the paste as it emerges reflects the shape of the opening or aperture through which it has been forced, and can be as simple or as complex as required. Fig.3.2 schematically shows the extrusion process. A piece of solid glass is heated in the furnace to become soft and forced to flow through a profiled die under a pressure from the top. Out of the die, the fibre is drawn down to canes at constant speed by a pulling wheel. Extrusion is particularly useful for glasses with steep viscosity-temperature behaviour.

3.2 Progresses in PCFs

Fig.3.3 outlines some of the major steps in the development of PCFs. I will go through most of these progresses with some examples.

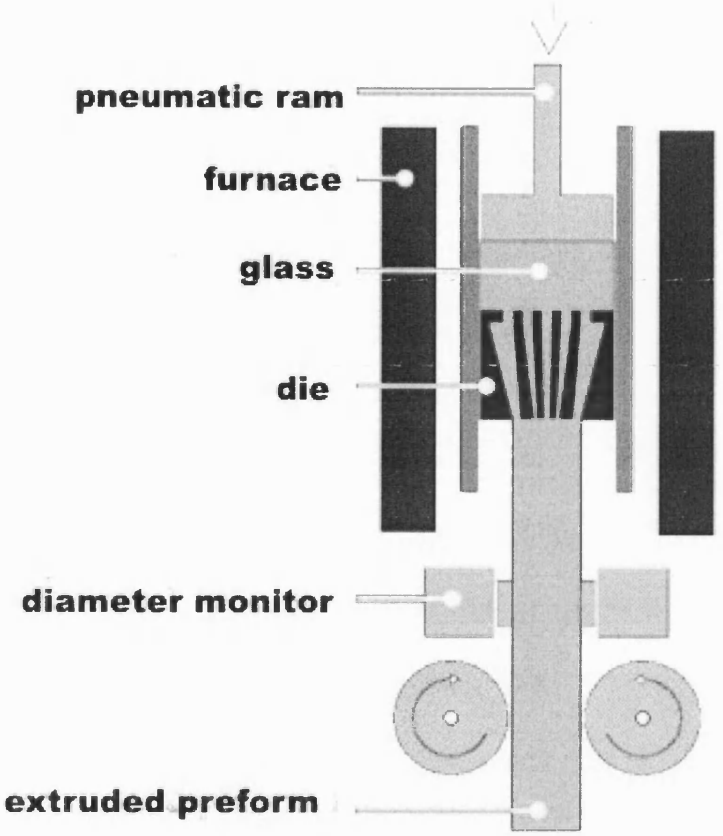

Figure 3.2: Sketch of the extrusion process

3.2.1 Progress in index-guiding PCFs

One of the first demonstrated characteristics of PCFs is the remarkably wide wavelength range in which the fibre can remain single-mode [6]. As explained in Section 2.1.3, a silica-air index-guiding PCF will become single mode for all wavelengths when the cladding structure satisfies the condition $d/\Lambda < 0.45$ [8]. Fig.3.4 shows the first endlessly single mode PCFs. The idea of controlling the mode capacity of index-guiding PCFs by changing the d/Λ value of the cladding is not limited by the operating frequency or material system, which enables us to make single mode fibre using other materials with special optical properties.

By making a cladding structure with only 2-fold rotational symmetry, we can get a fibre with high birefringence. Such fibres have been realised by several

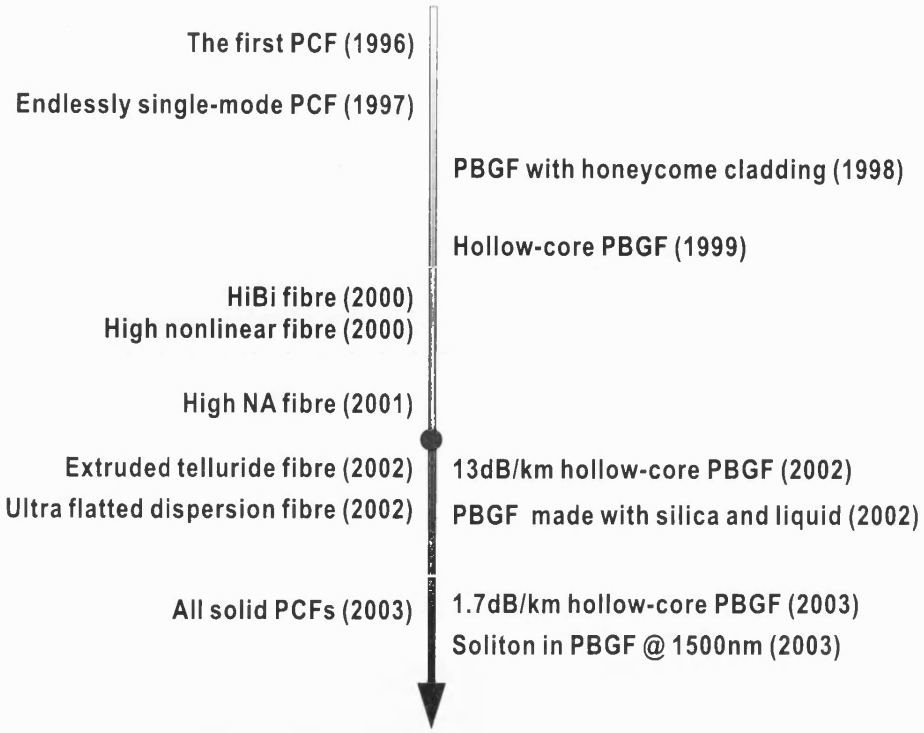

Figure 3.3: The time line of PCF progresses. The spot indicates the time when I started my Ph.D. research.

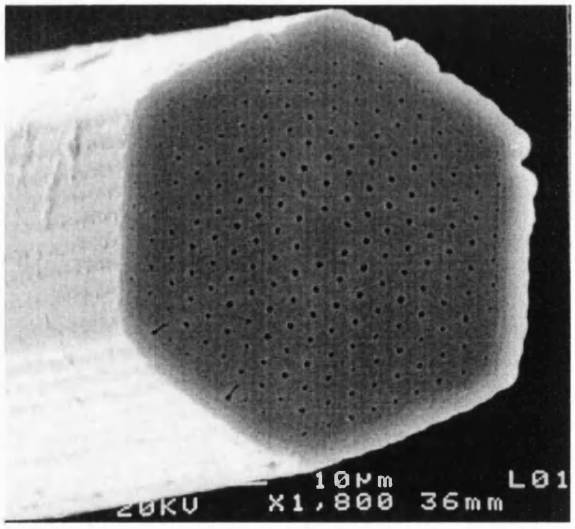

Figure 3.4: Scanning electron microscope image of the end of a photonic crystal fibre, showing the central core where a hole has been omitted. The pitch $\Lambda = 2.3\mu$m, and the fibre is 40μm across.

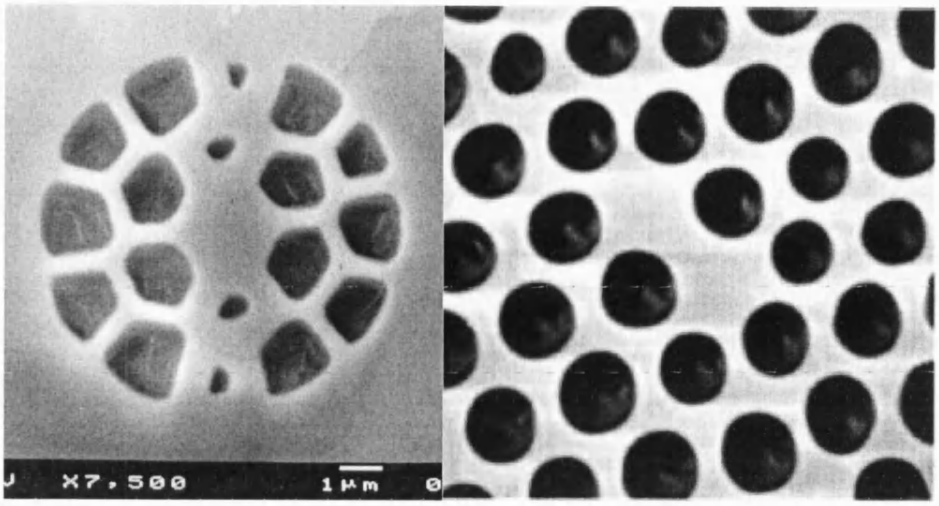

Figure 3.5: Left:Scanning electron micrograph showing detail of the cross-section of the core region of the fibre used in [24] having a line of smaller holes across the cladding. Right:Scanning electron micrograph of a Hi-Bi PCF with a highly elliptical core [25].

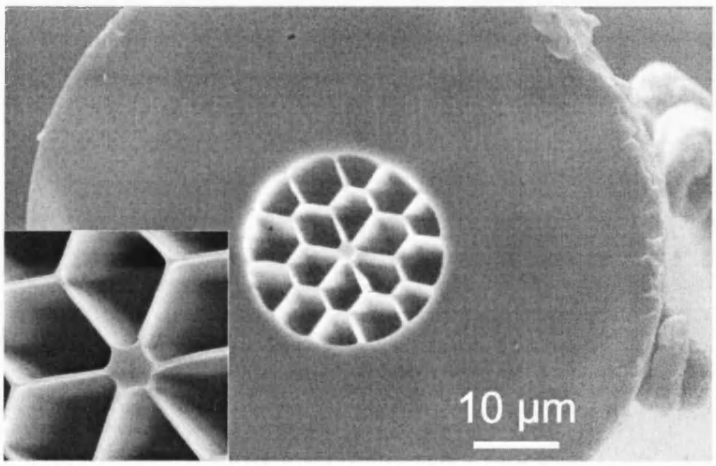

Figure 3.6: A scanning electron micrograph of a "cobweb" PCF (Fibre fabricated by, and picture courtesy of, Dr. W.J. Wadsworth)

research groups [24][25][26]. They broke the rotational symmetry of the fibre by either introducing holes with different sizes near the core or having an elliptical core as shown in Fig.3.5. Without further optimisation, these demonstrations have already achieved a modal birefringence $|n_x - n_y| > 10^{-3}$, which is 10 times bigger than that have been achieved with conventional techniques [27]. High birefringence PCFs was systematically studied in [28].

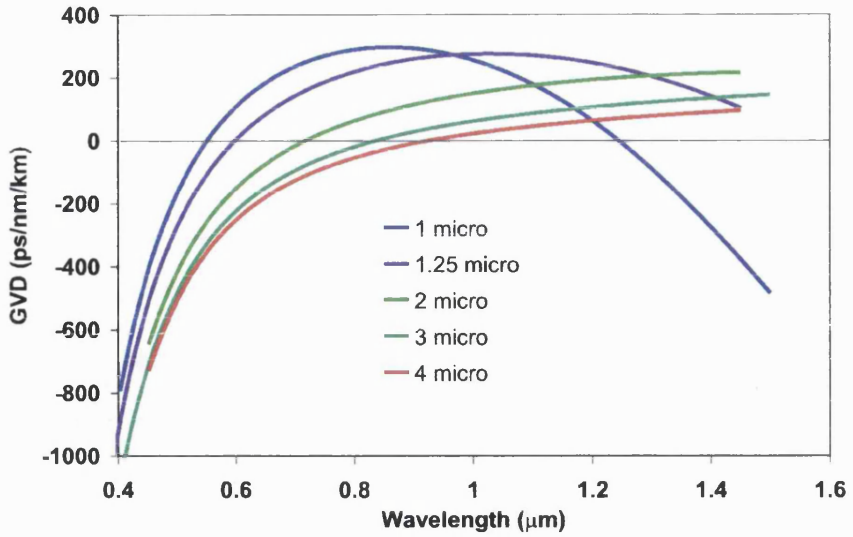

Figure 3.7: GVD curves of silica strands with different diameter in air.

Index-guiding PCFs having cladding with a large d/Λ (resulting in a large index step) can confine the light tightly in the core even when the core size is very small, which implies a high nonlinearity. Such a fibre can be considered as a small silica strand surrounded by air and is called "Cobweb" PCFs as shown in Fig.3.6. The dispersion of Cobweb PCFs, determined by the core size, is very different from the material dispersion. As shown in Fig.3.6, the frequency range with anomalous GVD is pushed towards to the high frequencies as the core size becomes smaller. Such a level of dispersion control, which has never been achieved with conventional fibre, combined with the high nonlinearity leads to some interesting new phenomena [29] (see Chapter 7).

At the other extreme from cobweb PCFs is PCFs with small d/Λ ratio. In this case, the dispersion slope can be reduced by finely tuning the pitch Λ and the d/Λ ratio. A wonderful demonstration of this is [30], which presents an ultra-flattened dispersion fibre with very small dispersion as shown in Fig.3.8. The nonlinearity in such dispersionless artificial materials has been explored [31]. Dispersion flattened PCFs were systematically studied in [32].

In order to achieve a large NA, one must arrange for the core and cladding materials to have widely differing indices. Unfortunately, the range of indices available in transparent solids (including glass and plastics) is relatively small. NAs above 0.4 are very uncommon in silica fibres. PCF techniques make it

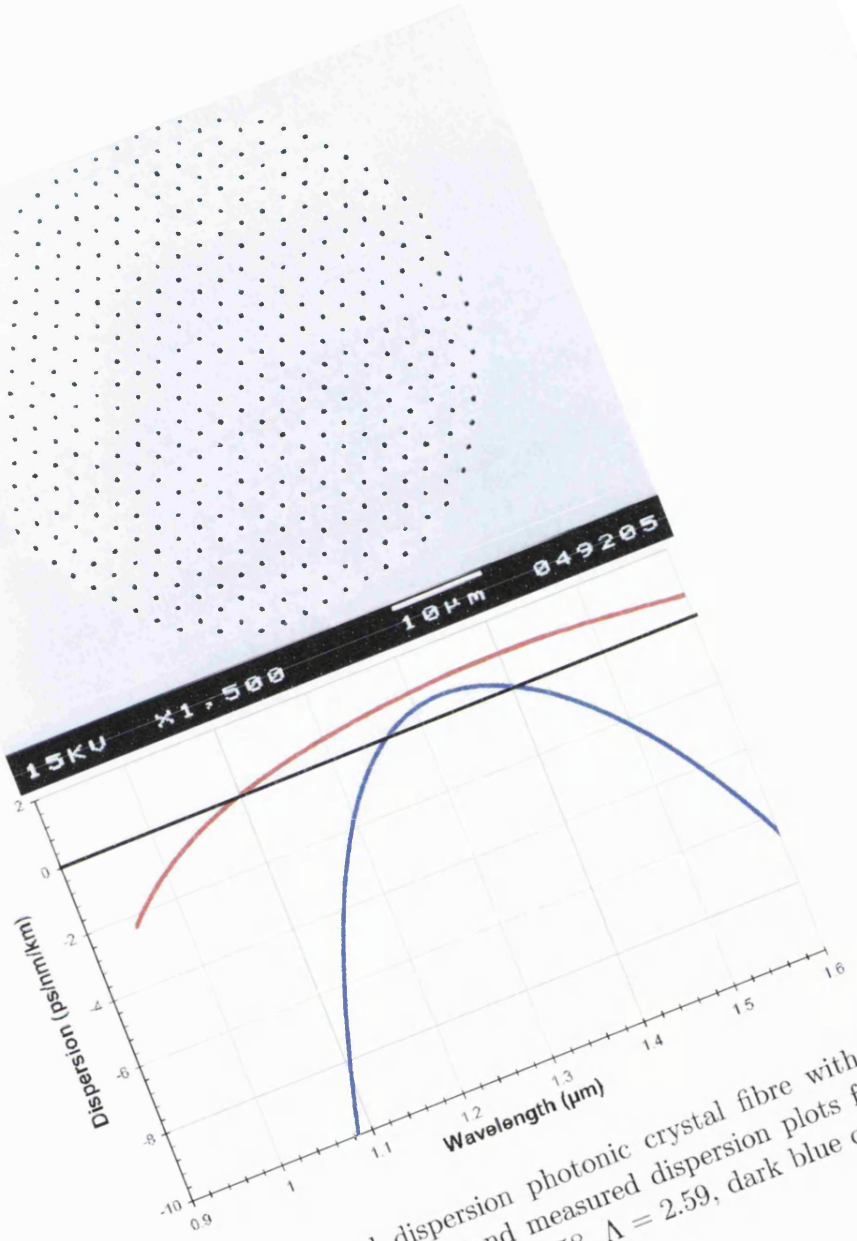

Figure 3.8: Ultra-flattened dispersion photonic crystal fibre with 11 periods ($\Lambda = 2.47\mu$m and $d = 0.57\mu$m), and measured dispersion plots for ultra flattened dispersion PCF. (Red curve: d=0.58, $\Lambda = 2.59$, dark blue curve: d=0.57, $\Lambda = 2.47$)

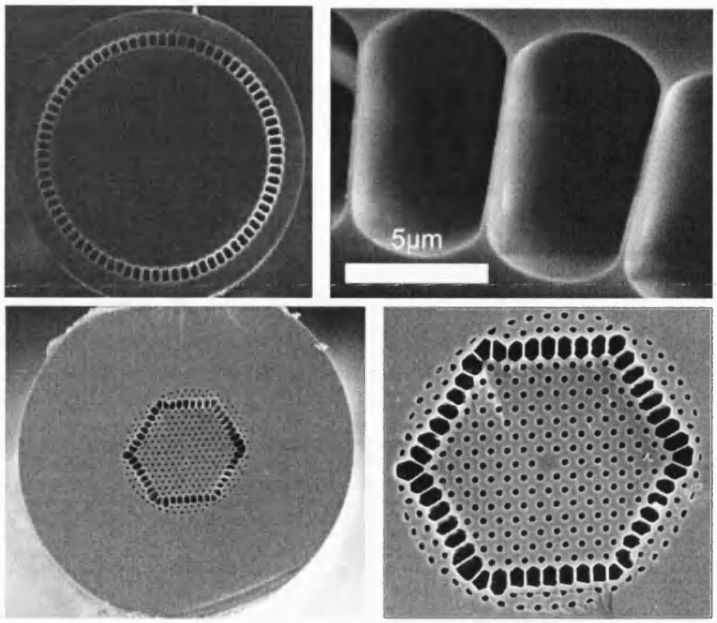

Figure 3.9: Above: doubleclad fibre with a conventional solid silica fibre core and inner cladding, suspended in air. Below: doubleclad fibre with a PCF core [33]

possible to support a silica core with a cladding of very thin silica strands whose effective index could be close to 1. In [33], people analysed theoretically and experimentally the features required in an air-silica structure in order to yield a high NA fibre. In particular, by making the silica strands thinner than $\lambda/2$ ($\lambda = 1.54\mu m$), they demonstrated PCFs (Fig.3.9) with measured NAs as high as 0.9 at 1.54μm over 41m of fibre. These high NA PCFs are very useful for cladding pumped high-power fibre lasers [34][35][36].

An all-solid index-guiding PCF composed of two types of silicate glasses was demonstrated in 2003 [37], as shown in Fig.3.10. For this, two types of silicate glasses, high index glass B1 and low index glass H1, with good compatibility in terms of mechanical, rheological, thermodynamic and chemical properties were drilled into tubes and rods by using an ultrasonic drill. Using the rod-in-tube method, a H1 glass rod was inserted within a B1 glass tube. Approximately 10 meters of uniform cane with B1 cladding and H1 core were drawn from this preform. These canes were then stacked within a B1 glass jacket tube using the conventional capillary-stacking technique. The structured preform was then drawn into fibres.

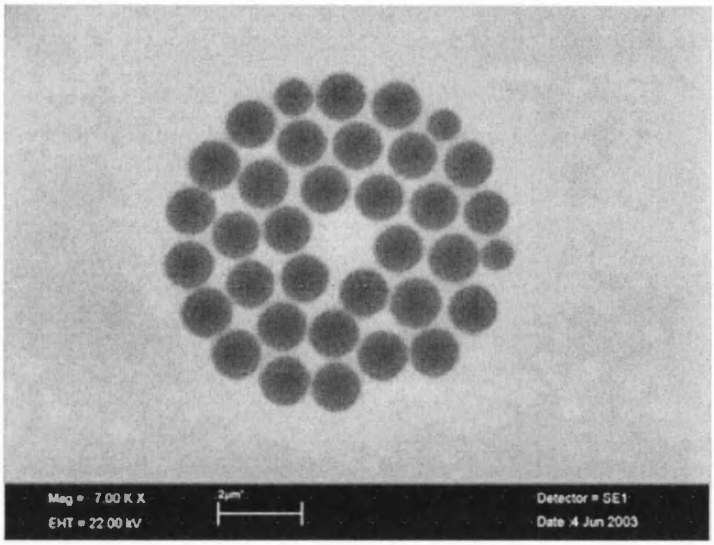

Figure 3.10: Back-scattered electron image of an all solid PCF [37]. Dark area indicates high index glass B1.

3.2.2 Progresses in Photonic bandgap fibres (PBGFs)

The guidance light using bandgap effects with silica-air structures, predicted in 1995 [38], was first demonstrated in 1998 [39]. The fibre, as shown in Fig. 3.11, was fabricated by stacking a few hundred solid silica rods and silica capillary tubes by hand in a hexagonal arrangement to form a fibre preform, which was then drawn down to fibre. A honeycomb structure is created by individual positioning of rods as well as capillaries in the stacking stage. An extra air hole is introduced into the centre of the honeycomb pattern by replacing a single solid rod with a hollow capillary. This "low-index defect" ensures that there are no index guiding effects. The observed guided mode is shown in Fig. 3.11(B)and(C).

Although the first photonic band gap fibre(Fig.3.11) was reported in 1998, hollow-core guidance had to wait until the technology had advanced to the point where larger air-filling fractions, required to achieve a photonic band gap for incidence from vacuum, became possible. The first such fibre [40] had a simple triangular lattice of holes, and the hollow core was formed by removing seven capillaries (producing a relatively large core that improved the chances of finding a guided mode). Optical and electron micrographs of a typical hollow-core PCF are shown in Fig.3.12. Launching white light into the fibre core resulted in the excitation

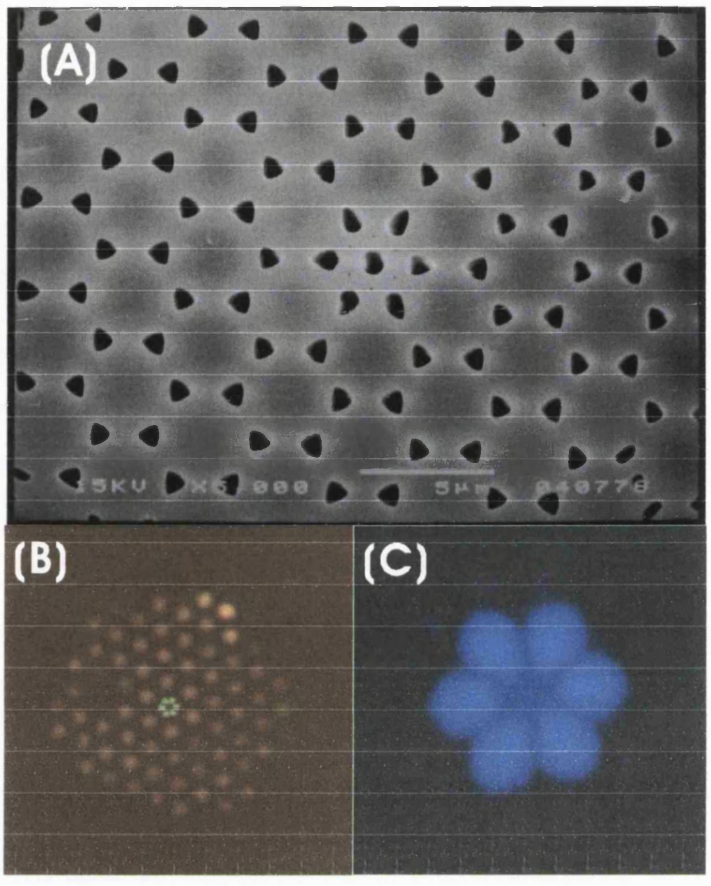

Figure 3.11: (A)Scanning electron micrograph of the surface of a cleaved PBGF. (B)Optical micrograph of a PBGF. (C)A photograph of the observed far-field pattern.

of variously coloured modes, indicating that guidance existed only in restricted bands of wavelength, coinciding with the photonic band gaps.

After the first demonstration, many efforts were made to reduce the loss of hollow-core PBGFs by improving both the fabrication control and the theoretical understanding. Meanwhile, I started my Ph.D. research work in Oct. 2001 to study the properties of PBGFs. The following chapters will present most of the results I had in the last three years. Some important results from others will also be discussed and compared with mine.

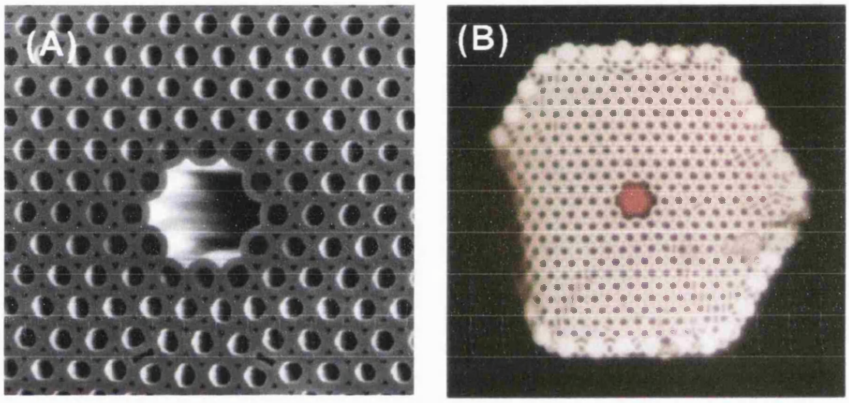

Figure 3.12: The first reported hollow-core photonic band gap fibre [40]. (A) a scanning electron micrograph. (B) a photograph of the nearfield of the fibre shown in (A) when illuminated with white light.

Chapter 4

All solid photonic bandgap fibres

In this chapter, we describe a new type of PBGF which has a solid core and an array of unconnected high-index rods in a low-index background as the cladding. Compared with most reported hollow-core photonic bandgap fibres (HC-PBGFs) (consisting of a central air core surrounded by a periodic array of air holes in a silica background), this new type of PBGF has some extraordinary properties. For example it has an ideal cladding structure for PBGFs; its core is formed by a "natural" defect which is free from "surface modes", and it exhibits multiple bandgaps. Such fibres have been demonstrated by putting high index fluid into a short length of standard solid-core silica-air PCF [41][42][43]. However, those fibres are hard to use and have an intrinsically limited length, as well as being unstable with respect to temperature and other environmental effects. Here we report the realization and characterization of a PBGF based on two thermally matched silicate glasses. This provides an opportunity to study the basic features of photonic bandgap guidance in an "idealised" structure. In the following text, we refer to this new type of fibre as the solid-core photonic bandgap fibre (SC-PBGF) to distinguish it from the hollow-core photonic bandgap fibre (HC-PBGF).

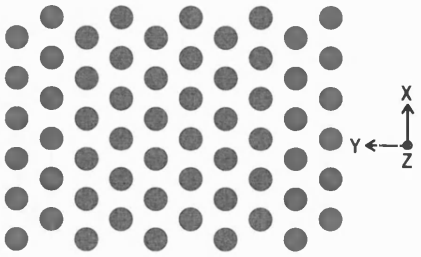

Figure 4.1: A sketch of a cladding structure composed of an array of high index rods in a low index background.

4.1 Anti-resonance guiding mechanism

Fig.4.1 shows a sketch of a cladding structure composed of an array of high index rods in a low index background. The bandgaps of such a cladding structure are easily seen to arise from the anti-resonance of each individual high index cladding rod [44][45]. To understand the anti-resonance guiding mechanism, let us consider a single high index (n_1) rod in a low index (n_2) background first and then we will find out the effects of putting many of such high index rods in a low index background periodically. Fig.4.2 illustrates the mode behaviour of a single high index rod in a low index background against frequency. At the high frequency limit ($k_0 \rightarrow \infty$), the light tends to be confined in the high index rod, so the $\beta - k_0$ curve tends to join the line of $\beta = n_1 k_0$, where k_0 is the wave number in free space. At the other extreme, the low frequency limit ($k_0 \rightarrow 0$), light spreads out of the high index rod so that β tends to join the line of $\beta = n_2 k_0$. To study the bandgap behaviour, we are interested in the narrow strip along the line of $\beta = n_2 k_0$, indicated by the red box in Fig.4.2. In order to concentrate the calculation efforts into the area we are interested in, we use a re-arranged density of states (DOS) plot [46][47].

The DOS is defined to be the number of states between β and $\beta + \delta\beta$ for a given k_0. In practice, the "$\beta - k$" plane is divided into a uniform grid and each grid unit is filled with a certain colour which is determined by the numbers of allowed β values within the grid unit. To focus on the narrow strip along the line of $\beta = n_2 k_0$, we replace the axis 'β' with '$\beta - n_2 k_0$' (or sometimes with '$\beta^2 - n_2^2 k_0^2$'). The re-plotted red box in Fig.4.2 is shown in Fig.4.3. Here we normalised both β and k_0 with the diameter of the high index rod d, because such a normalisation is valid for the Maxwell equations [1]. The light fields of those modes located on

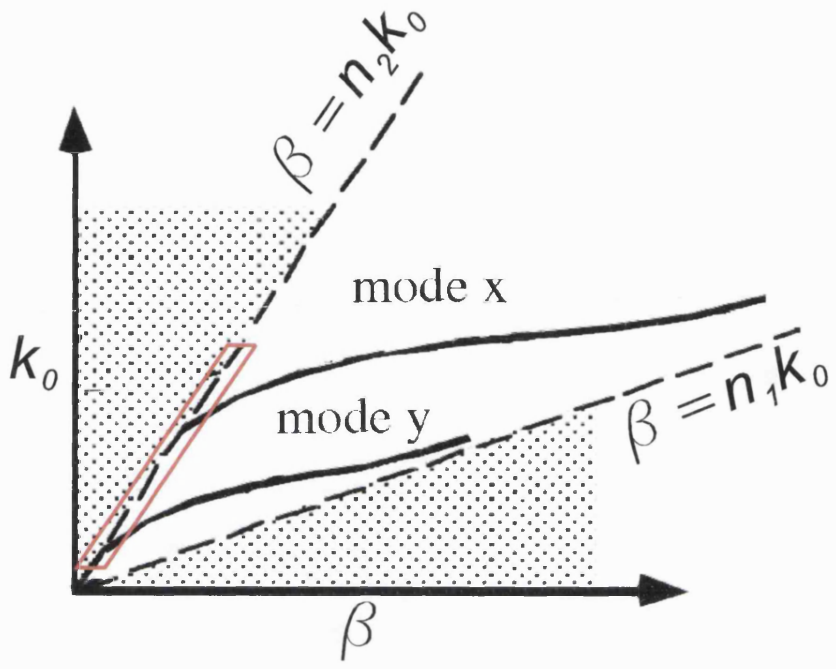

Figure 4.2: Modes of a single high index (n_1) rod in low index (n_2) background. The red box shows the area we are interested in for the discussion of band-gap effects.

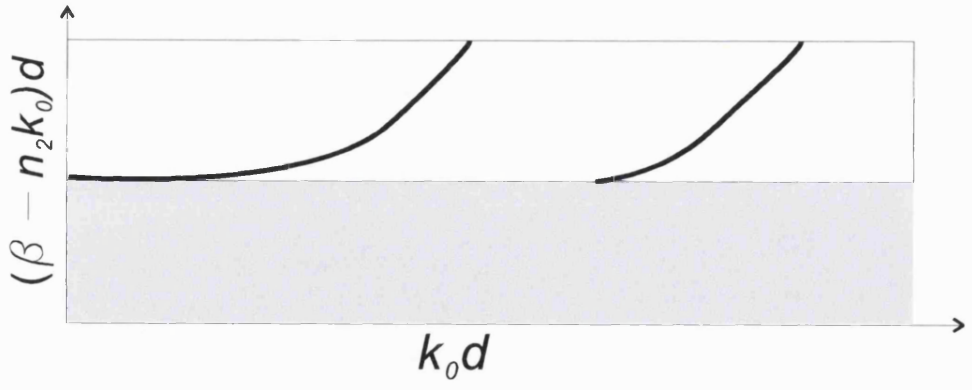

Figure 4.3: The same as Fig.4.2, but we focus on the red box with re-arranged axes.

the $\beta(k)$ curve (black curves in Fig.4.3), called resonant states, are concentrated in the high index rod and evanescent in the low index background. The grey area represents those waves that radiate into the infinite low index background. The large white area has zero-DOS, which means that those states located within the white area (called anti-resonant modes) cannot exist in the structure.

To deal with a more complex situation (for example an array of high index rods in a low index background), a proper numerical method is needed to calculate the DOS. The Plane-wave method (PWM) is widely used for the calculation of the band structure and DOS of a periodic cladding [1]. However, calculating the DOS efficiently along the line of $\beta - n_2 k_0$ by using the PWM is not straight forward, because it is more appropriate in this case to calculate the limit few extremal β values. My colleagues, Mr. T.D.Hedley and Dr. D.M.Bird, have developed a modified PWM to solve the problem [46]. Based on this modified PWM, they have also written a program to enable us to plot the re-arranged DOS map of a given PBGF structure.

Now let us consider a infinite array (for example a triangular lattice) of high index rods in a low index background just like the cladding structure of the band-gap fibres we are going to study. Fig.4.4 shows the DOS plots of identical rods placed at different distances from each other. Here we use red to fill the area which has zero DOS and a greyscale area to show non-zero DOS (a darker area has lower DOS).

Comparing the plots in Fig.4.4, we notice that as those high-index rods get close to each other there are two distinctive changes. First, originally well defined $\beta(k)$ curves expand into strips; second the anti-resonance region (i.e. the red area) expends across the line of $\beta = n_2 k_0$. We will discus them separately.

The expansion of the $\beta(k)$ curves is due to the coupling between the arrayed high-index rods. From coupled waveguide theory [5], we know that when two identical waveguides are coupled together the propagation constant β will split into two values $\beta \pm \Delta$, where Δ is the mutual coupling coefficient per unit length. The nearer the distance between the waveguides, the bigger the splitting of β. The coupling of many of these identical waveguides will expand the original β to a "conduction band" centred at β, and Δ is a good measure of its width. From Fig.4.4, we notice that the grey strips become narrower and narrower as they

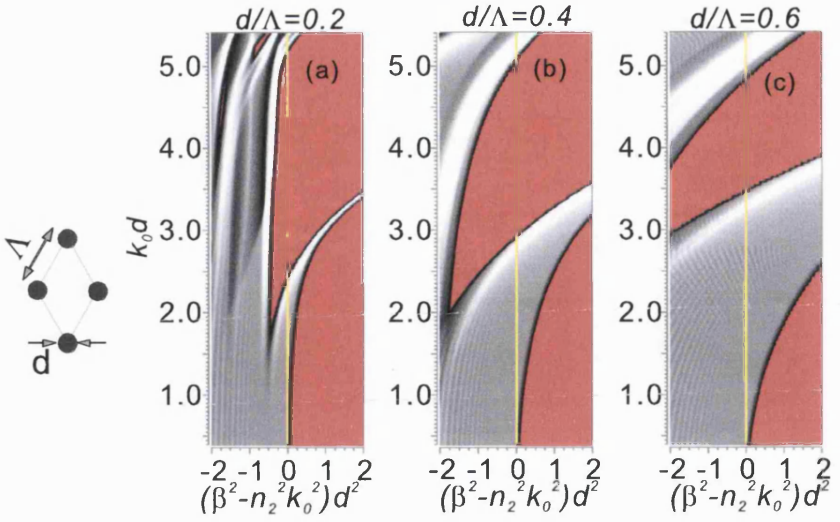

Figure 4.4: DOS plots of identical high index rods placed at different distances from each other, with the white regions having zero DOS. The background index was set to $n_2 = 1.54$, and the index of the rods was $n_1 = 1.79$. Here we employ the material indices of the glasses that we are going to use in our experiment.

more away from the line of $\beta = n_2 k_0$. This is because when β is close to $n_2 k_0$, the light field is extended outside of the high-index rods so the coupling between the rods is particularly strong resulting in a bigger Δ. As β moves away from $n_2 k_0$, light is more confined in each individual high-index rod and Δ becomes smaller.

The extension of the anti-resonance region is because of the presence of the array of identical high index rods. For the photonic states between the resonance stripes of the high index rods, the only way to exist in the structure is to propagate in the low index background. When there is only one high index rod, to propagate in the infinite low index background the wavevector of the light field does not need a transverse component. So the maximum β between the resonance stripes of the high index rod is equal to the absolute value of the wavevector in the low index material, i.e. $n_2 k_0$. When there is an array of high index rods, the light fields that are not resonant with the high index rods have to run through the space between the high index rods and need a non-zero transverse component of the wavevector (i.e. $k_\perp \neq 0$). So in this case $\beta = \sqrt{n_2^2 k_0^2 - k_\perp^2} < n_2 k_0$. The minimum $k_\perp \neq 0$ needed for the light to run through the space between the high index rods is determined by the pitch Λ. The smaller the Λ, the bigger the $k_\perp$. This is the reason why in Fig.4.4 the anti-resonance region is extended below the line of $\beta = n_2 k_0$, which is critical in enabling us to introduce guided modes into

such a cladding structure.

With our understanding of the mode behaviour in the cladding (the grey area in Fig.4.4), we can put core modes, which must be located in the red area in Fig.4.4, forbidden to the cladding modes, into the structure by introducing a defect. In this work we will simply remove some of the high index rods from the low index background to form the central core. Then the indices of the core modes are expected to be below but very close to the material index n_2. So the core modes would be located in the red area that is below the line of $\beta = n_2 k_0$ in Fig.4.4. After the discussion above, we should emphasise that it is the properties (size and index difference) of each individual high-index intrusion that determines the positions of each band-gap, and the distance between these intrusions (pitch Λ) only affects the shape (width and depth) of the band-gaps.

4.2 manufacture process of SC-PBGFs

4.2.1 glass properties

To make SC-PBGFs we use two different glasses. Before choosing the right glasses, we need to know something about how the glass properties change in the drawing process. Fig.4.5 shows the glass viscosity and expansion rate at different temperature. The expansion rate ($\Delta L/L$) of glasses increases with increasing temperature (T), i.e.

$$\frac{\Delta L}{L} = \alpha \Delta T \tag{4.1}$$

where α is the linear thermal expansion coefficient and is represented as the tangent of the curve in Fig4.5. We can see that the whole temperature range can be divided into three sections and in each of them α can be approximated as a constant. At low temperature, α has the smallest value and is denoted as $\alpha_{-30^oC-+70^oC}$. From room temperature to the glass transformation point T_g, α increases to $\alpha_{+20^oC-+300^oC}$. Beyond T_g, glasses deform under pressure and stresses can be relieved, so the value of α in this temperature range is not important for our purposes. To make a structure with two different glasses, both glasses must have about the same $\alpha_{-30^oC-+70^oC}$ and $\alpha_{+20^oC-+300^oC}$. Otherwise great stress will build up inside the structure when it cools down and the structure will be too

	refractive index @1060nm	$\alpha_{-30-+70^oC}/\alpha_{+20-+300^oC}$ $(10^{-6}/K)$	$T_{10}^{13}/T_{10}^{7.6}$ (^oC)
LLF1	1.53	8.10/9.20	448/628
SF6	1.77	8.10/9.00	423/538

Table 4.1: Thermal properties and material indices of commercial glasses SF6 and LLF1 from Schott Ltd.

fragile to handle.

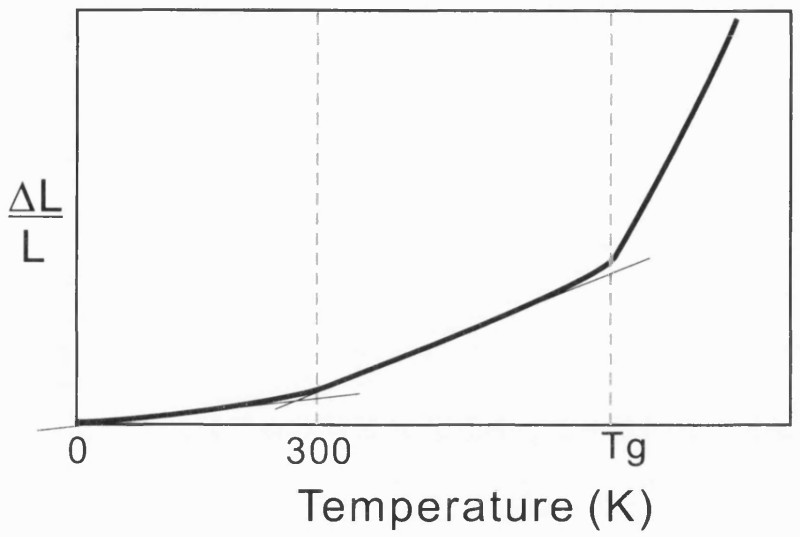

Figure 4.5: Typical curve for the coefficient of thermal expansion

Another important issue of putting two glasses into the structure is whether they can be drawn at the same temperature. The viscosity decreases by orders of magnitude as the temperature increases (shown in Fig.4.6). At the drawing temperature, the viscosity is in the range of $10 - 10^3$ Pa·s. Although the drawing temperature is often not available from the data sheets of commercial glasses, we can estimate the trends of the viscosity curve from the annealing temperature (T_{10}^{13}, where stresses can be relieved) and the softening temperature ($T_{10}^{7.6}$, where glasses deform under their own weight), which are usually listed in the data sheets. Normally, a big overlap in the temperature range between T_{10}^{13} and $T_{10}^{7.6}$ implies a similar viscosity curve in that range.

Apart from thermal properties, of course, the two glasses must have some index contrast. From the scaling law [47] of the Maxwell equations we know that if the material indices n_1 and n_2 vary, the photonic states will scale so that the value

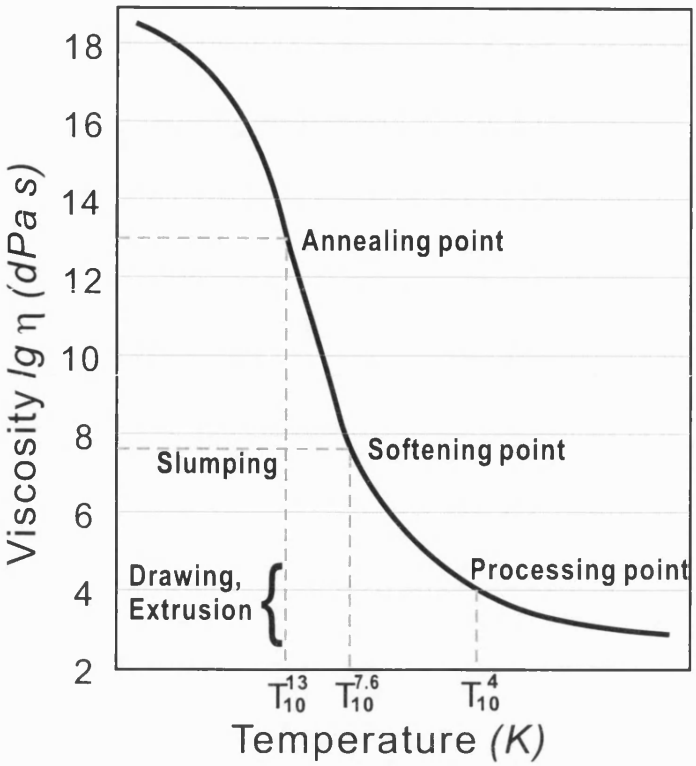

Figure 4.6: General trend of viscosity as a function of temperature. Viscosity ranges for important finishing operations and fixed points are shown.

of $d^2(n_1^2 - n_2^2)k_0^2$ is invariant. If we choose two glasses with a bigger material difference, then the fibre has to end up with a smaller d (the diameter of the high-index rods in the cladding) to keep the band-gap position fixed. The thermal properties and material indices of the glasses that we are going to use are shown in Tab.4.1.

4.2.2 Rod in tube method

Based on the stack-draw method, we made SC-PBGFs in two different ways: the rod-in-tube method and the multiple stack method. The rod-in-tube method, as described in Section 2.4.1, was the manufacturing method of silica fibre in its early age and is still used to make special fibres. Each of the fabrication steps is shown Fig.4.7. First we use the extrusion method to turn the low index glass LLF1 rods (diameter=15mm) into tubes (outer diameter OD=3mm; inner diameter

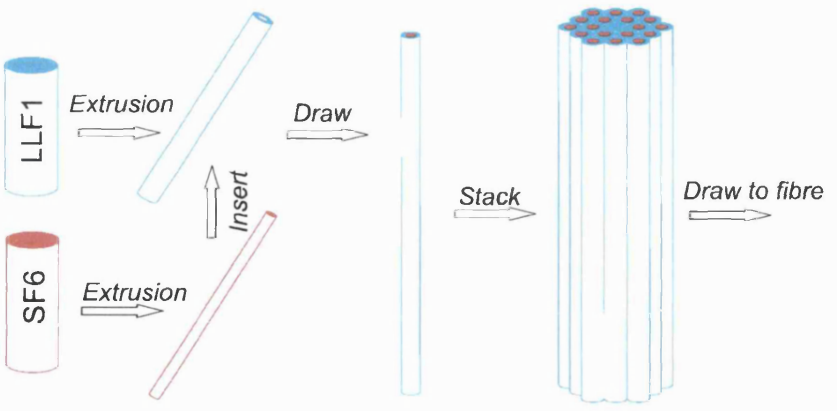

Figure 4.7: Rod-in-tube method

ID=1mm) and draw the high index glass SF6 rods to smaller size to fit into the LLF1 tubes. By drawing LLF1 tubes with SF6 rods inside down to 0.8mm diameter using the rod-in-tube method, we then have solid canes composed of two different glass. The subsequent steps are those for "stack and draw", which is similar to the fabrication process for normal PCFs. In the stack the central cane is replaced by a pure LLF1 rod to make the core.

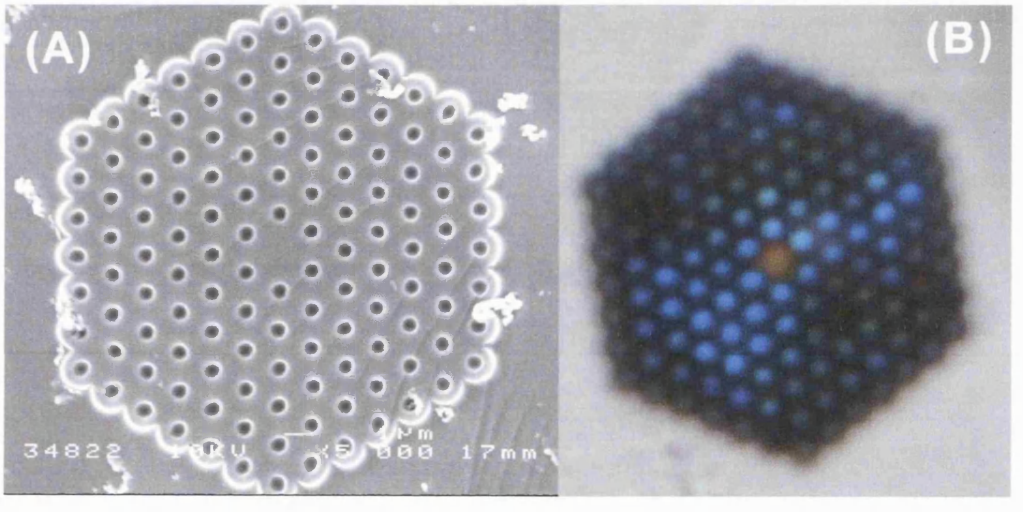

Figure 4.8: (A) SEM and (B) optical image of a fibre sample made by rod-in-tube method. The fibre was etched by dilute HF (20:1) for 10 seconds for taking the SEM images.

A scanning electronic microscope (SEM) image of a fibre sample resulting from the rod-in-tube method is shown in Fig.4.8. Before taking the SEM, we etched the

end face of the fibre sample in dilute hydrofluoric acid ($1HF : 20H_2O$) for several seconds. The differential etching speed of the two materials gives us a contour image: the higher level represents LLF1 and the lower level represents SF6. From the SEM image we can see that the geometric shape of the stack was preserved and that there is no obvious deformation. However, the attenuation of the fibre was so high that it is not possible to measure its optical properties. The high attenuation was caused by imperfections, such as air bubbles, crystallized glass particles and dust, lying on the glass interfaces, especially the interface between LLF1 and SF6, where the extruded surface of an LLF1 tube introduces more imperfections. Although some of the air bubbles can be seen under microscope, most of the imperfections cannot be observed in the SEM image (Fig.4.8), because all the bubbles at the glass interfaces are merged into the holes left by the etched SF6. Despite the failure of the first trial with the rod-in-tube method, we still think of this method as the first choice for our purpose. For the time being, it is not possible to improve the quality of the extruded tubes in a short time, so we turn to the other method.

4.2.3 Multiple stack method

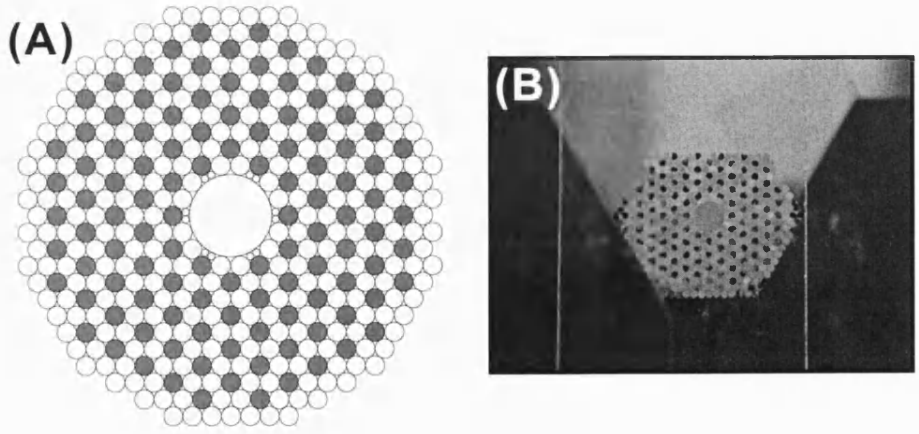

Figure 4.9: (A) The schematic of the stack. Grey rods are SF6 and white rods are LLF1. There are LLF1 fibres inserted between the core and the cladding to fill the gaps. (B) Photograph of the finished stack.

In order to reduce the imperfection-introduced loss we adopt the multiple stack method. The multiple stack method avoids the extrusion step by isolating each of the SF6 rods by 6 LLF1 rods instead of an LLF1 tube, so no tubes were

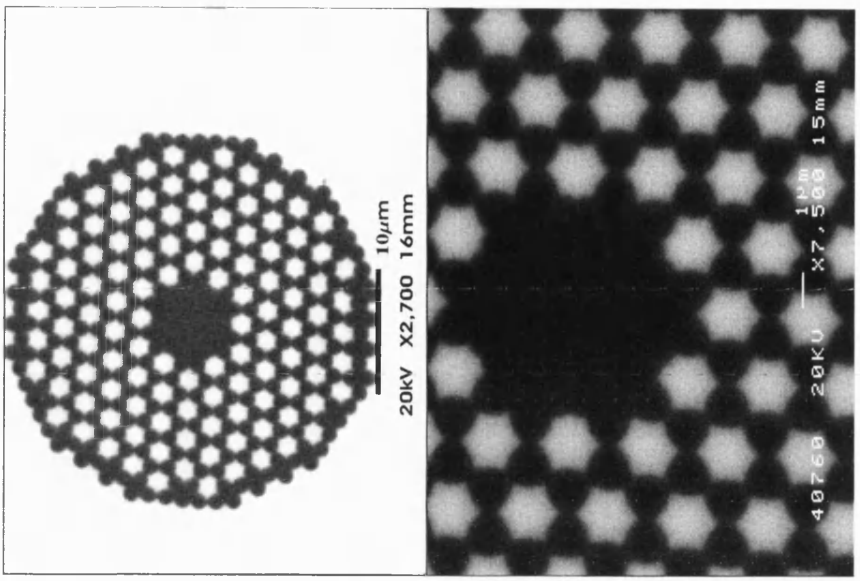

Figure 4.10: Back-scattered electron(BSE) images

needed in the fabrication process. A schematic of the stack and a photograph of the finished stack are shown in Fig.4.9, where SF6 rods are marked with grey. In the actual stack the diameter of each individual rod is 0.8mm. The central area, which would have contained 7 SF6 rods and 12 LLF1 rods, was replaced by one big LLF1 rod to form the core. Such an arrangement leads to a core composed of 7 missing unit cells in the final structure. We put 12 thin LLF1 fibres into the gaps between the central LLF1 rods and the cladding structure to avoid trapping any air in it. The bigger core, compared with the structure in Fig.4.8, will improve the coupling efficiency and make the fibre characterization easier. The stack was drawn to fibre in two stages, between which a thick SF6 jacket was added. Fig.4.10 shows a back-scattered electron (BSE) image (also known as composition image) of a fibre sample made by this method. The BSE signal, sensitive to the average atom number of the sample material, can monitor the material difference even on a flat sample surface, and without etching, the imperfections on the glass interface could be kept and observed. In Fig.4.10 the lighter regions are SF6 and the darker areas are LLF1. We can see that the SF6 rods turn into star shapes uniformly, because at the drawing temperature SF6 is softer that LLF1. In terms of the mechanical properties, both the rod-in-tube and the multiple-stacking methods are quite successful. The resulting fibres are strong and easy to cleave. The strain between the two different glasses in the fibre is not noticeable unless the fibre is tightly bent. We characterize the linear

properties of this type of fibres as shown in Fig.4.10 in the following sections.

4.3 Linear properties of SC-PBGFs

4.3.1 modelling the real structure

To analyse the effect of the deformation of high index rods, we carried out a DOS calculation on the cladding structure derived from electron microscope images of real fibre to compare with the undeformed case as shown in Fig.4.11. The modelled structure consists of an array of touching low-index circles superimposed on a high-index background. The diameter of the undeformed high index rod was chosen so that it has about the same area as the star shaped high index rod. From here onwards we use the pitch Λ instead of the diameter of the rods d to normalise k_0 and β. This is valid only because in the drawing process the pitch and the size of the rods scale together. But we should always keep in mind that the band-gap position is fixed by the size of the rods (for fixed materials) and not the pitch. The deformation of the rods made it difficult to define their size, so the use of pitch here is just for the sake of convenience.

Fig.4.11 shows that the shape of the high index rods has a relatively small effect on the position and shape of the photonic band-gaps, especially at the low frequency side, at which the light field is not sensitive to the tiny features of the deformed rods. As the frequency increases, the light field is increasingly sensitive to the corners of the deformed high index rods. The change of light field distribution introduces more coupling between adjacent rods (compare with the undeformed structure), which leads a visible narrowing of the bandgaps at the high frequency side. The band-gap with the lowest frequency is called the fundamental band-gap. Other band-gaps with higher frequencies are called higher-order band-gaps.

4.3.2 Transmission

We measured the transmission spectrum by coupling a supercontinuum white light source into two different fibre samples of length about 20cm. The transmit-

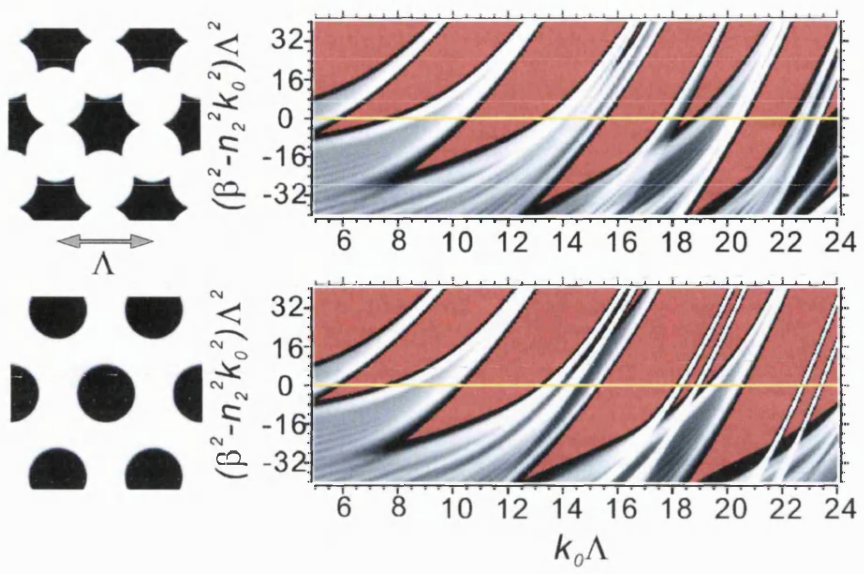

Figure 4.11: Comparison of bandgap plots for the idealized array of circular high-index rods and for the array of star-shaped high-index rods found in the actual fibers. High-index material is represented in black.

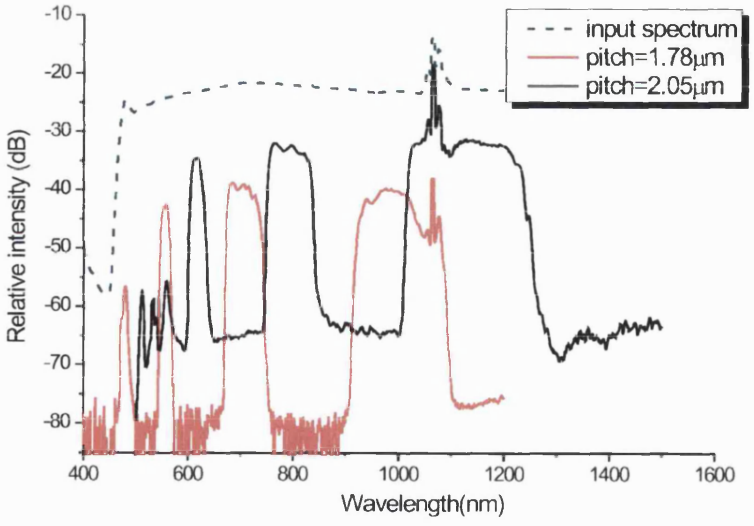

Figure 4.12: Transmission spectra with different pitches. The spikes near the 1064-nm wavelength are the residual pump that was used to form the supercontinuum (the grey curve) for the measurement.

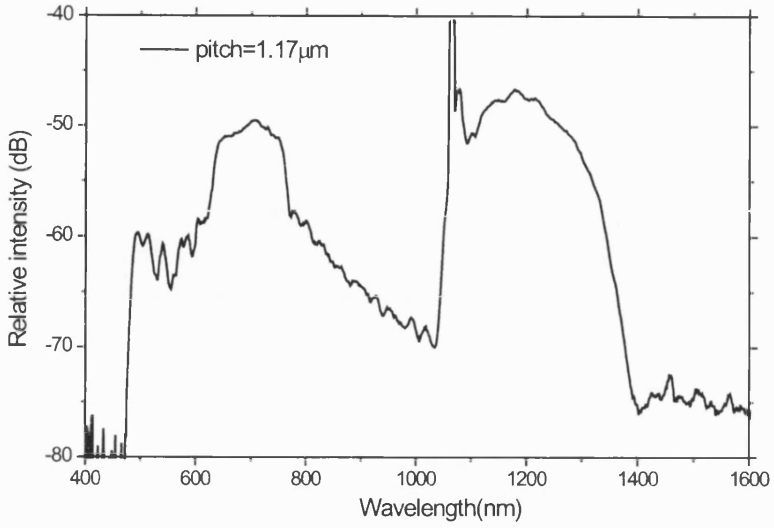

Figure 4.13: The transmission spectrum of a fibre sample with 1.17μm pitch. The fundamental band is centred at 1200nm.

ted spectra, as shown in Fig.4.12, has several low-attenuation windows, which stand out from the background up to 30dB. We can see that as the pitch gets smaller the band-gaps shift to higher frequency to satisfy the scaling law [47]. From the numerical simulation (see below), we can identify the orders of the band-gaps. In Fig.4.12, the 2nd-order band is the lowest-order transmission band that can be observed with our optical spectrum analyser (OSA). By drawing the fibre down to even smaller size ($\Lambda = 1.17\mu m$), we observed the fundamental band shown in Fig.4.13. The central wavelength of the fundamental band is twice that of the 2nd-order band, which makes it very difficult to have good optimum coupling for both bands. In Fig.4.13, the optimum coupling wavelength was 1200nm.

Simulations were also carried out to compare with the experimental results. At first the measured spectrum did not fit well with the calculated transmission band position (Fig.4.11), which is caused by the fact that material dispersion was not taken into account in the initial simulation. In order to model the structure more precisely, we performed computations based on the real structure over a broad frequency range, and included the material dispersion of the two component materials. The result is shown in Fig.4.14. For the sake of clarity,

only the DOS along a line of $\beta = n_2 k_0$, which is very close to the propagation constant of the fundamental mode, was plotted in the figure. By comparing the computed DOS and the observed transmission bands, the low-loss regions observed experimentally are seen to correspond to the second, third and fourth order band-gaps respectively (see Fig.4.11). Fig.4.14 shows great consistency in the simulated and measured position and relative width of each band-gap. We should notice that in this figure we used commercially-available data on n_1 and n_2 and their dispersions, and structural information ($\Lambda = 1.79\mu m$) was directly measured from the electron microscope images. There were no adjustable parameters in the fit.

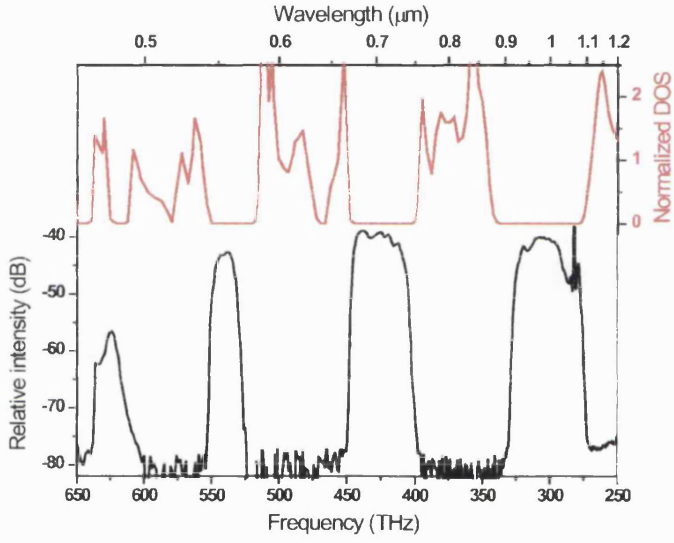

Figure 4.14: Comparison of the transmission spectrum measured through a fiber sample ($\Lambda = 1.79\mu$m) of 20cm length with the normalized density of states computed along the line $\beta = n_2 k_0$. The spikes near the 1064nm wavelength are the residual pump that was used to form the supercontinuum for the measurement.

We have measured the attenuation in our fibre using a cut-back technique, and find it rather high at around 18dB/m at the bandgap centre. The intrinsic attenuation of the core material is less than 1dB/m over the wavelength range of visible and near-IR, so our fibre suffers from substantial extrinsic attenuation. We attribute this to the presence of bubbles at the glass interfaces, which arise during our multiple-stacking process, and which are visible in some fibres. We be-

lieve that improvements in fabrication procedures will make it possible to reduce or virtually to eliminate this effect.

4.3.3 Dispersion

We used low-coherence interferometry to measure the group index of the fibre. Fig.4.15 shows a schematic diagram of the experiment setup, which employs a Michelson interferometer. One arm contains the fibre under test and a fixed mirror. The other, the reference arm, has dispersion compensation lenses and a mirror mounted on a computer controlled linear translation stage. The position of the translation stage should make the translation range cover the point at which the two arms has the same optical path. The input is a tunable 3nm bandwidth source obtained by passing a supercontinuum generated from a 1064nm pump source through a monochromator. The interference signal was detected by a high gain detector which is AC coupled to a lock-in amplifier. The lock-in amplifier was triggered by a chopper between the fibre sample and the reflection mirror to pick out the right reflection signal. At each wavelength, by scanning the mirror we recorded the envelope of interference signal which was peaked at mirror positions x that make the group delay of the two arms equal. x is a linear function of the group index, i.e. $x = (n_g - 1)L + x_0$ where L is the fibre length and x_0 is the mirror position without fibre sample. The dispersion was then derived from the group index curve by using $D = \frac{1}{c}\frac{dn_g}{d\lambda} = \frac{1}{cL}\frac{dx}{d\lambda}$. The measurement accuracy of x is determined by the coherence length of the input light, which was tens of microns in our experiment, therefore the error of the measurement of the group index, about 1%, mostly comes from the measure of fibre length.

The measured group index and dispersion are shown in Fig.4.16. As expected, the group index curve in each band drops to a minimum before rising again, which is similar to the reported behaviour of the group indices of HC-PBGFs [48]. The measured group indices over two transmission bands of the SC-PBGF show the possibility of matching the group indices at widely different wavelengths, which could lead to some interesting applications. The shape of the group index determines the GVD of the fibre. The GVD becomes increasingly anomalous (normal) as the wavelength moves to the low (high) frequency side of the transmission band. The difference of the GVD between SC-PBGFs and HC-PBGFs is that the material dispersion must be taken into account in SC-PBGFs. We will discuss this

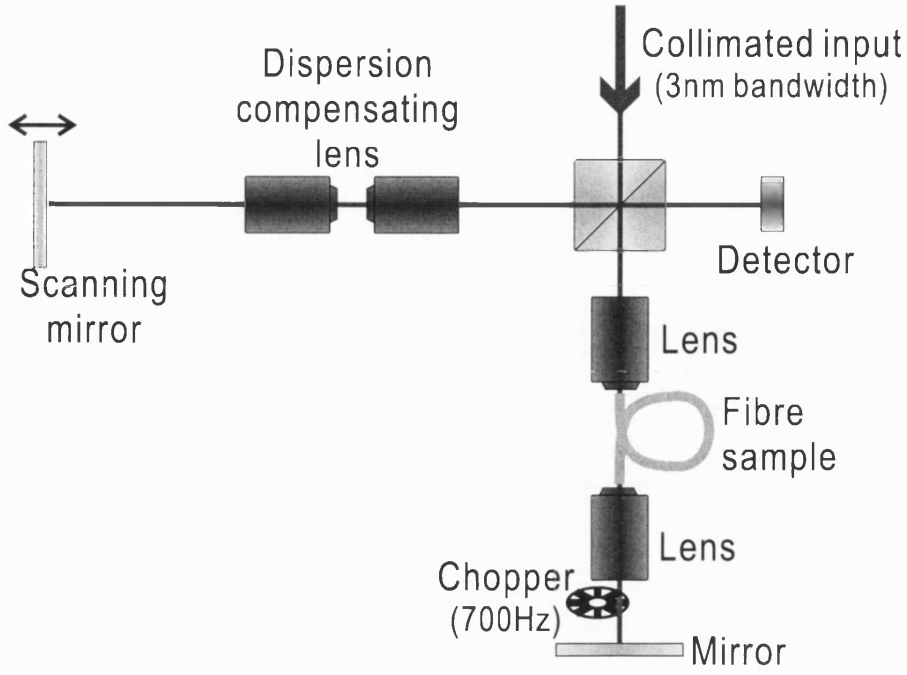

Figure 4.15: The experimental setup for the group index and dispersion measurement.

in more detail in Section 5.2.5. In some fibres, we have observed a small splitting of the fundamental guided band due to polarization effects, but these are always rather weak.

4.3.4 Nearfield patterns and Optical images

Fig.4.17 shows the optical images of short (about 4cm) fibre samples with different size. It is clear that light is well confined in the core area. We have also observed the propagation of higher-order core modes in our fibres by imaging the near-field as shown in Fig.4.18. The number of guided modes in photonic bandgap fibres is determined by the depth of the band gap and the core size: for our cladding design, we would need a considerably smaller core to guide just a single mode. However, fibres with smaller cores are difficult to excite efficiently, and have higher attenuation. Experimentally, we can easily excite purely the fundamental mode in the fibres described here, and the fundamental mode does not couple to higher-order guided modes even when the fibre is disturbed. It is worth noting

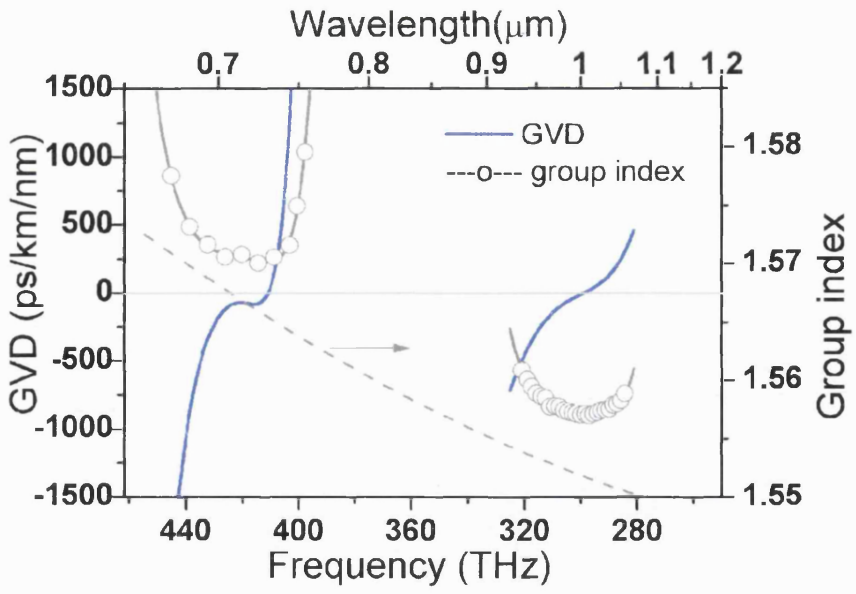

Figure 4.16: Measured group index and dispersion

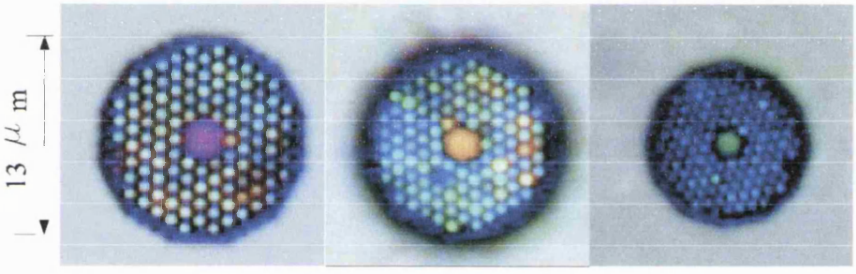

Figure 4.17: Optical images

that exclusively higher-order modes are observed near the long-wavelength edges of the transmission bands where the fundamental mode first joins the cladding modes. This effect is shown schematically in Fig.4.19

4.4 Conclusion

In conclusion, all solid photonic band-gap fibres have been successfully made and characterized. We have observed transmission through the first five bandgaps in these fibres, and attribute the bandgap formation to anti-resonances of the high-index strands in the cladding. The structures of this all solid PBGFs represent

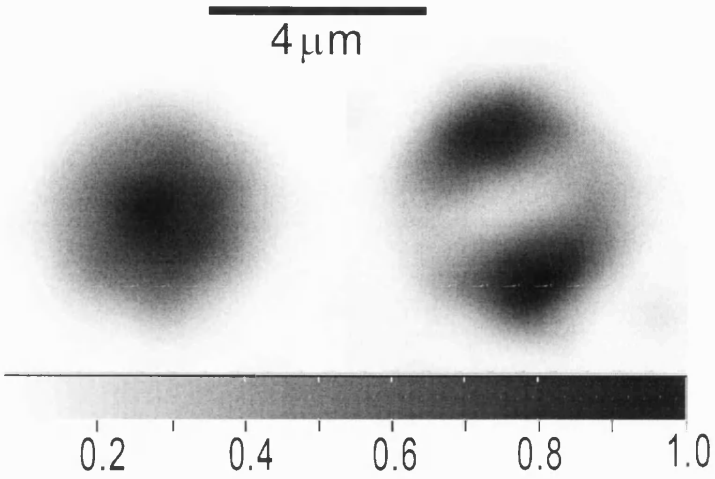

Figure 4.18: Near-field patterns. The left image was taken at 690nm and the right image was 575nm

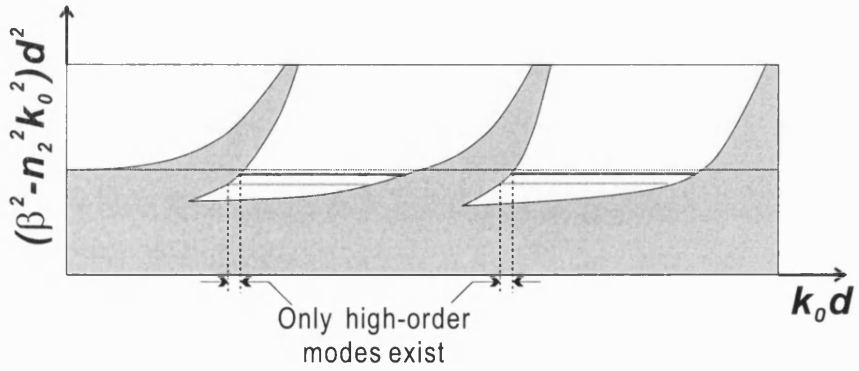

Figure 4.19: A schematic plot to show the effect that only high-order modes can be observed at the low frequency sides of the band edges.

photonic bandgap fibres in their ideal case, with isolated high-index rods in a low-index background, and do not exhibit effects from surface-modes (see Section5.3) because of the detail of the core/cladding interface.

Chapter 5

Linear properties of hollow-core photonic bandgap fibres

The ways of fibres with solid cores limits the fibre transparency, dispersion behaviour and nonlinear response to roughly the corresponding values in the bulk materials. This has had a profound influence on the development of fibre optics: for example, the spectral dependence of the attenuation and dispersion of bulk silica led to the development of optical telecommunications in the 1.3μm and 1.5μm wavelength bands. In Chapter 3, we showed the recent progress on guiding light through a hollow-core photonic bandgap fibre (HC-PBGF). Photonic bandgap fibres guide light at a low-index "defect" site within the photonic crystal lattice which forms the cladding. HC-PBGFs are potentially of enormous importance in that they may free fibre performance from material constraints. During the period of my research, low-loss HC-PBGFs designed for use at a wavelength of 1.5μm were reported [48][49]. In this chapter we present work in which the wavelength range of fundamental-bandgap guidance is extended to cover the 850nm wavelength band and we also report, for the first time, on many of the linear properties of such fibres. Fabricating fibres for use at 850nm is more challenging because the dimensions of the fibre microstructure, which are proportional to the guiding wavelength, have to be reduced to roughly half of those required for fibres for 1550nm. The larger draw-down ratio results in more deformation of the fibre structure, while the stronger surface tension forces associated with the smaller features make the structure less stable during drawing. However, fabricating fibres for shorter wavelengths is worthwhile, because the properties of

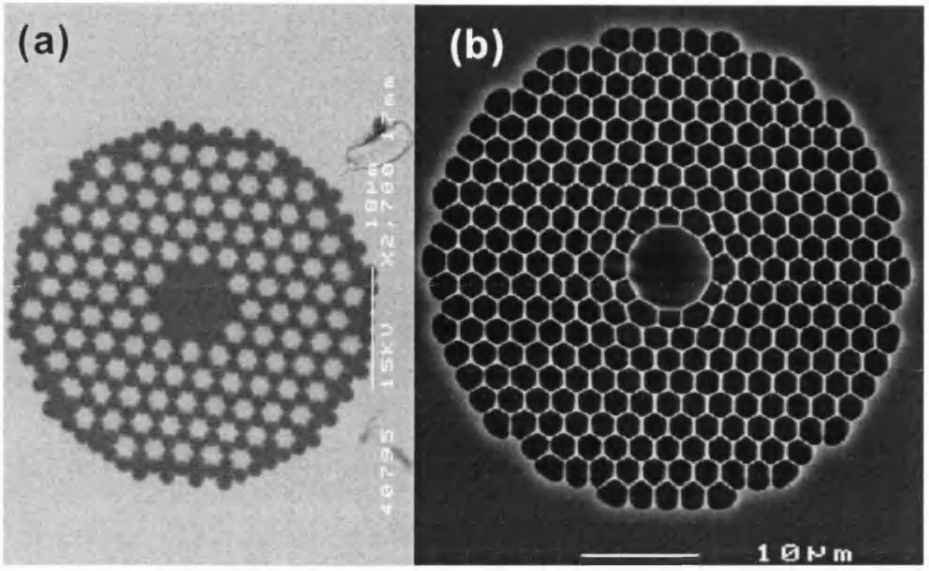

Figure 5.1: Comparison of the SEM images of a SC-PBGF and a HC-PBGF. (a) SC-PBGF. Light grey areas represent high index material. (b) HC-PBGF (Photo courtesy of BlazePhotonics Ltd.). The isolated black areas represent holes.

hollow-core fibres should make them useful for delivering high power ultrashort optical pulses.

5.1 The guiding mechanism

As a comparison, we show SEM images of a solid-core PBGF and a hollow-core PBGF in Fig.5.1. Contrary to solid-core PBGFs, in which high index material is isolated by the low index material, in hollow-core PBGFs the low index material, air, is isolated by the high index (silica) mesh. Despite the differences of these two types of structure, they share the same guiding mechanism as that based on the anti-resonance of high index intrusions. In Fig.5.1(b), we can see that there is a blob at each intersection of three neighbouring glass strands. Fig.5.2, DOS plots of cladding structures, with the same silica strands but different blob size, show the importance of these blobs. It can be seen that when the blobs are absent the bandgap is very narrow and shallow; when the blobs are present the band gap is relatively wide and deep. The position of the bandgap is largely dependent on the blob size.

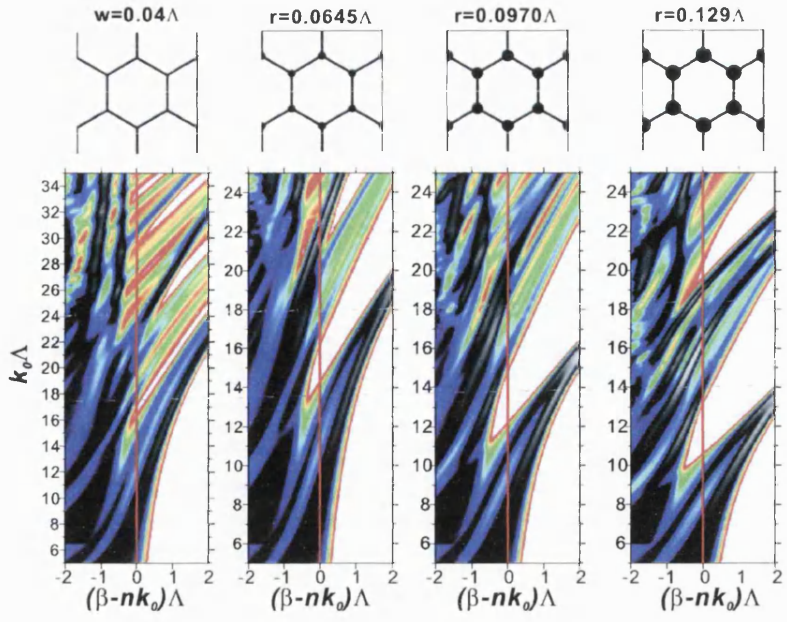

Figure 5.2: DOS plots of cladding structures that have different blob sizes. In all these plots, the widths of the silica strands are fixed to be 4% of the pitch (Λ). r is the radius of the blob in the structure.

The effects of the thin supporting strands on the bandgap are shown in Fig.5.3, in which we turn the structure into an array of isolated identical silica intrusions in the background of air by breaking the strands and then change the coupling strength by a 60^o rotation of each silica intrusion. We can see that the breaking and the rotation of the silica strands do not change the position of the fundamental bandgap and the high-order bandgaps begin to open up as a result of reduced coupling between the silica intrusions. This indicates that the antiresonance of these silica intrusions is the guiding mechanism of HC-PBGFs. The thin silica strands are really a result of a compromise between performance and feasibility. The fibre performance would be improved if the connecting strands of silica were even thinner or completely absent, but such a structure is not self-supporting.

5.2 Measured properties of HC-PBGFs

The fibre sample we studied was provided by BlazePhotonics Ltd. Fig.5.4 shows a SEM image of the fibre, which was fabricated by using the stack-and-draw

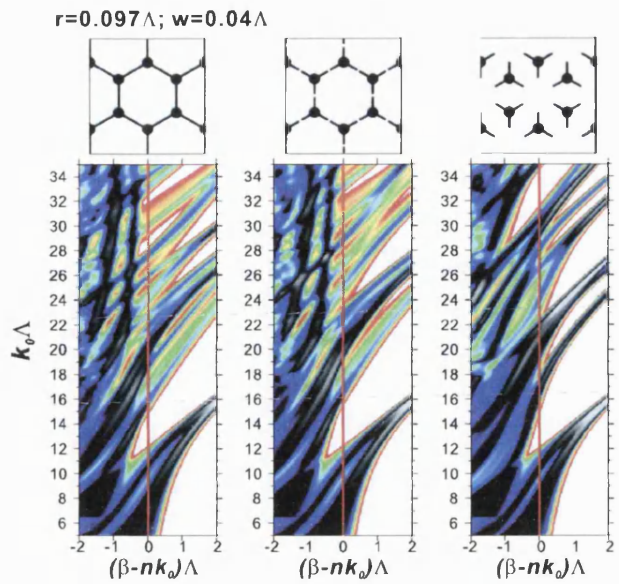

Figure 5.3: DOS plots of structures with broken silica strands.

method. Deformations around the core are from the drawing process in which the big hole (the core) tends to expand and makes the holes around it collapse. Carefully controlled gas pressure inside and outside the preform is applied to reduce the deformation. In the following subsections, I will present the measured linear properties of this fibre sample.

5.2.1 Loss

The optical attenuation of the fibre shown in Fig.5.4 was measured with a broadband light source using a cut-back technique. The light source was a tungsten-halogen lamp and the spectral analysis was performed using a commercial optical spectrum analyser (OSA). The fibre was wound in a single layer on a spool of 16cm diameter. The measurements were done by holding the fibre in standard bare fibre adaptors connected directly to the light source and the OSA. The fibre length was cut from 56m to 20m. The shorter length was chosen to be 20m because the broadband light source used in this measurement resulted in substantial cladding-mode and surface-mode [50] excitation. The attenuation of the fibre as a function of wavelength is shown in Fig.5.5. The fibre guides light in a low-loss band of roughly 70nm width, centred at a wavelength of 850nm. Outside of this

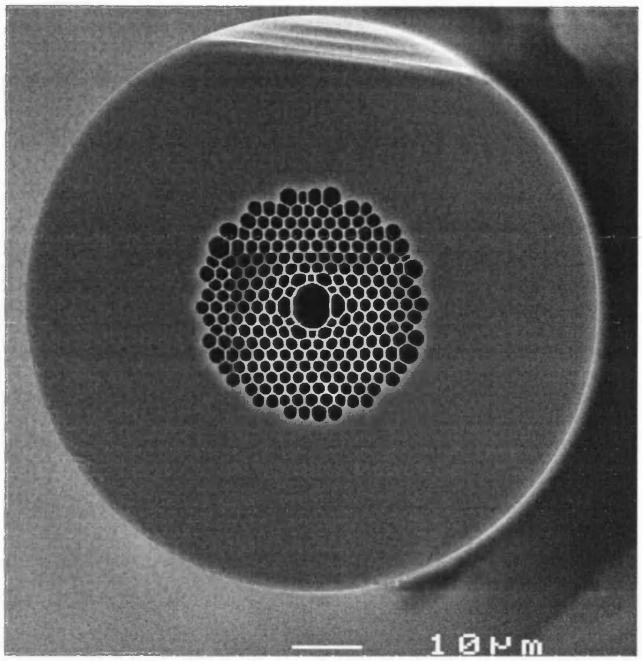

Figure 5.4: Scanning electron micrograph of the 850 nm air-core fibre used in this work. The spacing between the holes in the cladding (the pitch Λ) is 1.94μm, and the elliptical core has major and minor axes of 7μm and 6μm length. The air filling fraction in the cladding is over 85%. Photo courtesy of BlazePhotonics Ltd.

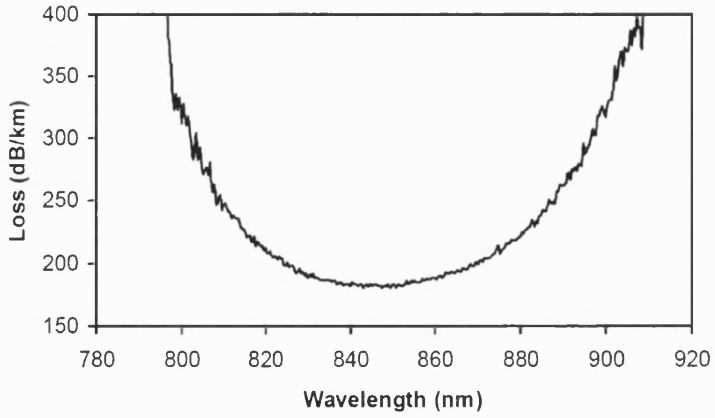

Figure 5.5: Attenuation recorded via a cutback measurement on 56m of the fibre sample used in the following experiments.

low-loss band, the attenuation increases rapidly. No other low-loss transmission bands were found in a wavelength range spanning 500nm - 1600nm. The lowest loss recorded in this fibre was 180dB/km at a wavelength of 847nm, although we have measured similar fibres with losses in this wavelength band as low as 130dB/km whose transmission curves were not as attractive in terms of symmetry and bandwidth. In principle, it is possible to form fibres with a somewhat broader transmission band than this fibre by improving the fibre structure, and it is certainly possible to form fibres with different central wavelengths in this band simply by scaling the microstructure.

The attenuation in hollow-core fibres is expected to be limited by similar mechanisms to those found in conventional fibres: confinement, bend loss, micro bending, Rayleigh scattering, and local imperfections. Clearly, the contributions of these to the overall loss, and the level of each of them, will differ from those in conventional fibres, as will their dependence on wavelength. In the current fibre, calculations suggest that the intrinsic cladding thickness is sufficient to reduce confinement loss to well below the observed level. On the other hand, the microstructure forming the cladding is imperfect (see Fig.5.4), so that confinement loss is a likely mechanism limiting the fibre loss. Support for this supposition is found in the variation in the fibre loss between nominally identical 50m lengths of fibre, which can vary by an order of magnitude with very little change in the bandwidth or central wavelength.

Bending the fibre macroscopically does not measurably increase the attenuation: in our experiments we have wound 100 turns of fibre around a mandrel of 5mm diameter, and the additional loss caused by such bending is not measurable. Bending the fibre more tightly does not lead to catastrophic bend loss either, until the fibre snaps at a bend radius less than 2mm. Bulk Rayleigh scattering in hollow-core fibres will be substantially reduced when compared to the bulk scattering from silica, because over 95% of the light of the guided mode is propagating in air. On the other hand, there is an unknown contribution from surface scattering, which will have a different spectral dependence to bulk scattering. Variations in the structure along the fibre over length scales of meters to microns will cause loss and scattering out of the fundamental mode: we know such variations are present (we detect variations in the outer fibre diameter of a fraction of a percent during the draw) but we have not quantified their contribution to the overall loss. As for previous air-core fibres [40] we believe that structural vari-

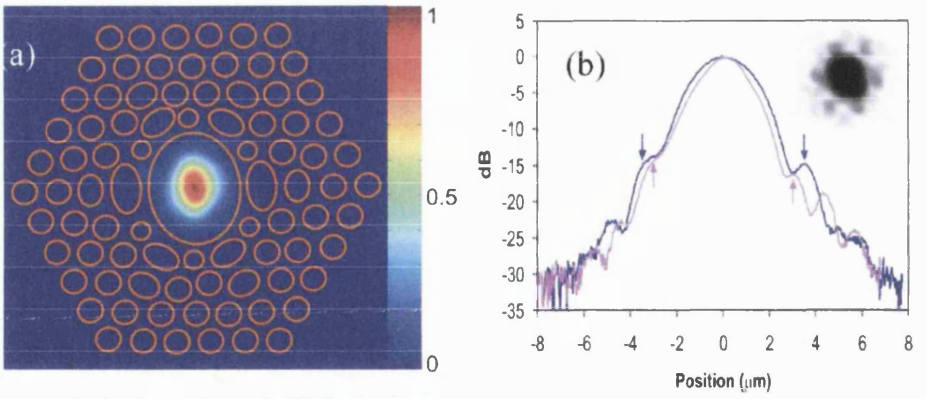

Figure 5.6: (a) Near-field pattern of the guided mode, recorded at a wavelength of 848nm after transmission through 60m of fibre (linear scale). The location of the first few rings of air holes are represented schematically as the orange outlines. (b) Line plots through the two axes of the elliptical core, in a logarithmic scale, with arrows indicating the positions of the core wall. The inset shows the far-field pattern, as recorded on infrared photographic film.

ations within the fibre cross-section and along the fibre length are the limiting factors in the samples used in this work.

5.2.2 Observed guided modes

We have used near-field imaging to study the guided-mode pattern as a function of wavelength. Light from a Ti:Sapphire laser was introduced into the core of a 60m length of the fibre using an objective lens, and the output face was imaged (with suitable attenuation) using a 40× objective onto a 12-bit digital camera. The pattern observed at a wavelength of 848nm (at the centre of the guiding band) is shown in Fig.5.6.

In order unambiguously to identify the relative orientation and scale of the fibre structure, we have illuminated the output face of the fibre with a small portion of the laser beam using a beamsplitter, and so simultaneously imaged the fibre output face. This enables us to place the locations of the holes in the fibre in relation to the guided-mode pattern, and a few rings of (not always circular) air holes are shown schematically as orange outlines in the figure. The guided mode is very well confined within the air core, and is roughly Gaussian in shape.

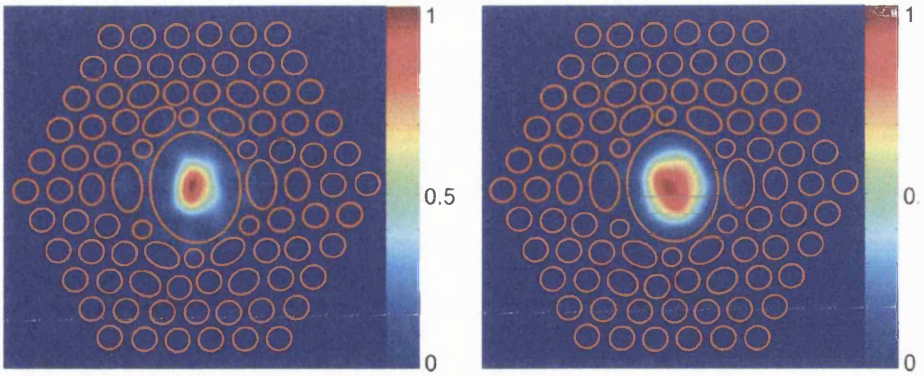

Figure 5.7: Near-field patterns observed after transmission through 60m of fibre on the edges of the guided wavelength range at 790nm (left) and 898nm (right), plotted on a linear scale. The locations of the air holes in the first few rings around the core are shown schematically.

Fig.5.6(b) shows line scans through this plot along the two principal axes of the elliptical core (plotted on a logarithmic scale). Numerical analysis of Fig.5.6(a) shows that more than 90% of the guided mode is in the core. Using photographic film, we recorded the far-field intensity pattern shown in the inset to Fig.5.6(b) at a wavelength of 850nm with no optics between the fibre endface and the film. The film is saturated in the centre to show the far weaker features on the edges, which are more than 20dB below the main peak. The measured numerical aperture (NA) of this mode was 0.17 at 848nm, taken at the 5% intensity points.

The observed patterns do not change as the input is varied, nor as the fibre is moved about. We have scanned the wavelength over the guidance band, and find only rather small changes in the modal field pattern over the 100 nm band centred on 850nm, as shown in Fig.5.7. We can couple more than 60% of the power of our Ti:Sapphire laser beam into this "fundamental" mode at 850nm, and this could probably be increased with more precise matching of the NA.

When this experiment is repeated using a shorter length of fibre (1m) and a higher power coupling lens (numerical aperture roughly 0.3), a range of different output field patterns can be seen (Fig.5.8). We attribute these to the excitation of higher-order guided modes, which experience much higher loss than the fundamental mode because of larger overlap with the silica, and a higher transverse wavevector component. The fibre is not intrinsically single-mode, and computations on similar structures (done by BlazePhotonics Ltd. using the FDTD

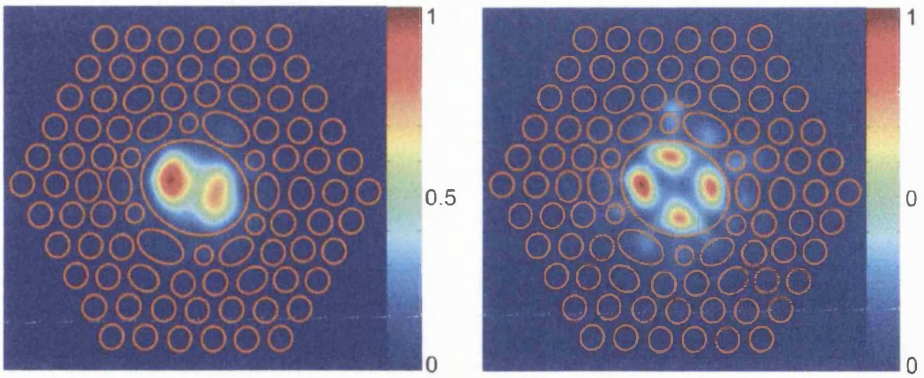

Figure 5.8: Near-field patterns of higher-order modes excited in a short piece of fiber (1m length) at a wavelength of 882nm, plotted on a linear scale. The two plots correspond to different excitation conditions. The locations of the air holes in the first few rings around the core are shown schematically.

method) reveal that one can expect several localized modes to be within the bandgap. However, the corresponding differential losses are found to be substantial, and as in strongly-guiding solid-core photonic crystal fibres [51], and the bend-induced coupling between the low-loss mode and the higher modes is very weak. It is worth noting that a high differential loss means that bend-induced modal coupling would manifest as transmission loss through a long piece of fibre, which is not observed in our bending experiments. Unlike previous work at longer wavelengths [52], we cannot observe higher-order mode patterns in lengths of longer than a few meters. Consequently, the fibre can be used as if it were single-mode.

5.2.3 Properties of the low-loss mode: birefringence

The fibre used in these experiments has an elliptical core (ratio of axes 0.85 : 1) due to unintentional but almost uniform deformation during the drawing process. The ellipticity is introduced mainly through deformations in the innermost ring of air holes surrounding the core. The deformations are apparent in Fig.5.4, and the effect of ellipticity on the modal field patterns is visible in Figs.5.6-5.8. It is of interest to consider the polarization-mode splitting of the fundamental mode which arises as a result of this deformation, and the extent to which light introduced into one polarization mode of the fibre is coupled to the other by

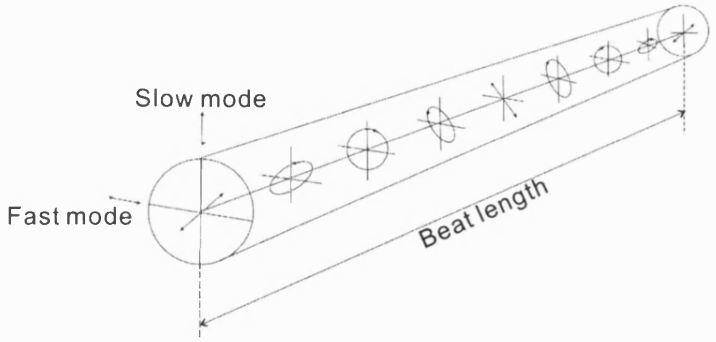

Figure 5.9: Schematic illustration of the evolution of light polarization along a birefringent fibre when the input beam is linearly polarized at 45^o with respect to the axes

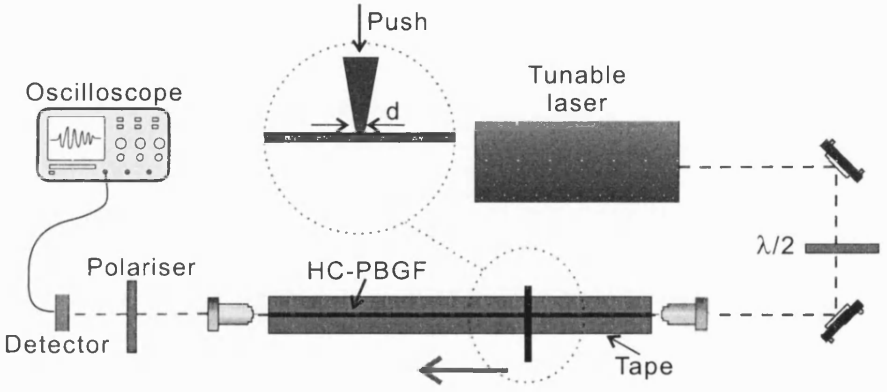

Figure 5.10: Experimental setup for the lateral force technique. d≈1.0mm

bends and twists along the fibre length.

To this end we have measured the polarization beat length, by introducing a localized mechanical deformation of the fibre cross-section [53] as shown in Fig.5.10. We used a half-wave waveplate to align the polarised laser light at 45^o to the polarization axes at the fibre input, and a polariser aligned to one of the polarization axis at the output. We then introduced localized mode coupling by sliding an object of around 1mm diameter along the fibre length, with a force of a few Newtons. We observed high-visibility oscillations in the light transmitted through the polariser as shown in the inset to Fig.5.11. By repeating this measurement at different wavelengths, we found that the beat length ranges from 4mm to 13mm over the guiding band (Fig.5.11). We confirmed the measurement at long wavelengths by cutting the fibre back in short lengths of approximately

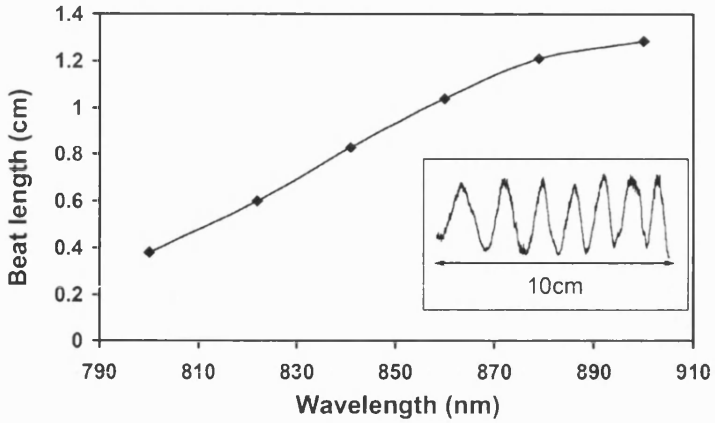

Figure 5.11: Measured beat length for the fundamental polarization modes as a function of wavelength across the guidance wavelength band. Inset shows an example of the data used to measure the beat length, showing the intensity transmitted through the polariser as the mechanical disturbance is slid along the fibre length. The fringes are not uniformly spaced only because the speed of the mechanical disturbance was not constant.

1mm, and studying the output polarization state, which gave results in good agreement with the mechanical perturbation method.

Although the observed level of mode splitting is already significant, changes in the fibre design rather than simply deformation of existing designs will be required in order to make a very highly birefringent air-core fibre without an very elliptical mode [54],

5.2.4 Properties of the low-loss mode: dispersion

We have studied the dispersion of the guided mode through the low-loss region using a time-domain method, followed by a low-coherence interferometry method. With the time domain method we measured the GVD directly by putting a short pulse into the fibre sample and measuring the output pulse length as a function of wavelength. We used an autocorrelator to measure pulse lengths using 200fs input pulses from a mode-locked Ti:sapphire laser. In order to maintain a measurable output pulse length, we used a fibre length of 0.67m. In deriving dispersion values from output pulse lengths, we assumed that the pulse propagation was linear, consistent with our observation that there were no observable spectral changes in

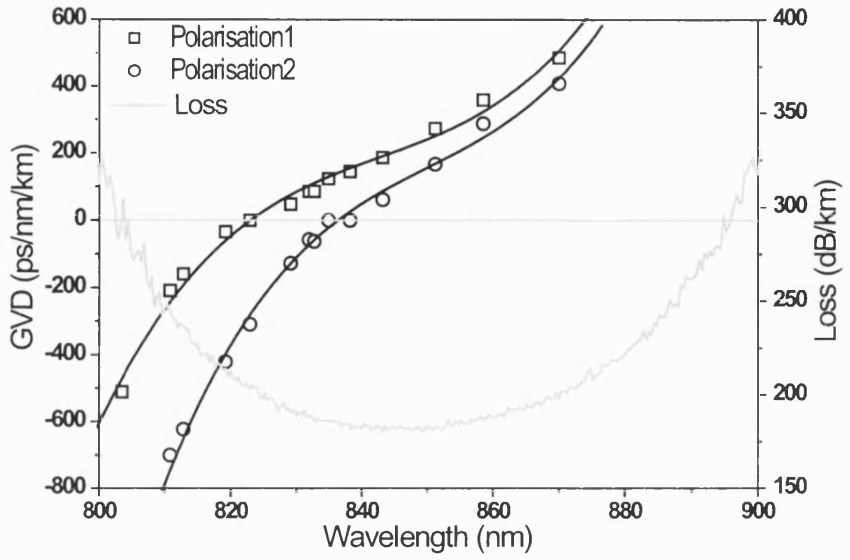

Figure 5.12: Group velocity dispersion curves measured for the two polarization modes using the time-domain technique. Output pulse lengths were measured with an autocorrelator, and the sign of the dispersion was obtained from the low-coherence data. The attenuation curve is shown here for ease of reference.

the output at the powers used. We also found that the measured autocorrelation trace width was independent of the input power. The pulses were measured independently for the two polarization modes of the fibre, by using a half-wave plate between the laser and the fibre.

Assuming the input pulses are transform limited Gaussian pulses with FWHM pulse length T_0, we know that after a linear propagation the output pulses are chirped Gaussian pulses whose FWHM pulse length T_1 is determined by [10]:

$$T_1 = T_0 \sqrt{1 + \left(\frac{L\,|\beta_2|}{0.361 T_0^2} \right)^2} \tag{5.1}$$

where L is the fibre length. From Equ.5.1 and Equ.2.8 we get the absolute value of the dispersion (D parameter). According to the low-coherence interferometric GVD measurement, which is shown below, we know that D is always increasing as wavelength increases. We can then determine the sign of the D parameter. The resultant GVD curves are shown in Fig.5.12.

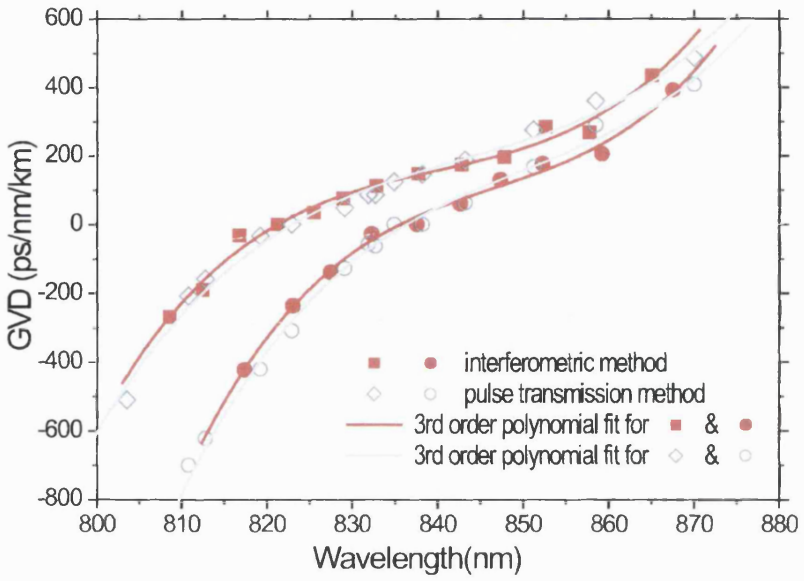

Figure 5.13: Comparison of the GVD measured by the interferometric method and the pulse transmission method.

To examine the accuracy of the GVD measured by the time-domain method, we also measured the GVD with the low-coherence measurement, which is the same as the one we used to measure the SC-PBGFs' GVD in Chapter 4, which was performed using a white-light source and 3nm band pass filter in conjunction with a Michelson interferometer. A comparison of the GVDs measured by these two methods is shown in Fig.5.13, which shows rather good agreement with each other. The relatively small discrepancy may come from the fact that the input pulses in the time-domain method were not exactly transform limited.

Fig.5.12 and Fig.5.13 show that the GVD crosses zero within the low-loss window, and is anomalous over much of the guidance band. The dispersion slope around the minimum-loss wavelength is less than 10ps/nm^2/km for both modes, comparable to that previously reported at 1300nm [55]. This slope may be reduced through refinements in the fibre-making process, suggesting that linear transmission of ultrashort pulses through lengths of many meters of fibre with low dispersion will be feasible. In our preliminary experiments, we transmitted 200fs, 4nJ pulses through 20m of fibre at the zero-GVD wavelength. The auto-

correlation width of the output pulse was then broadened to roughly 3.5 times that of the input pulse, partly due to modest spectral deformation. Improvement can be expected by working away from the zero-GVD wavelength and using a compensation or pre-chirping scheme. The fact that the GVD is anomalous over much of the wavelength range is expected to enable the formation of solitons in the fibre at relatively high peak powers and we will investigate the soliton effect in hollow-core PBGFs in the next chapter.

The measured group indices of the two fundamental polarization modes are presented in Fig.5.14(a). As expected, the group index is close to but slightly above unity and increases as the wavelength moves away from the centre of the transmission band. In the same wavelength band, the value of the group index reflects the confinement ability of the fibre. The smaller the group indices, the better the confinement of the fibre. Fig.5.14(b) shows the measured group indices of a fibre sample with less deformation produced later by BlazePhotonics Ltd. The minimum group index of this fibre is only different from the unity by an amount of 0.0059 which is 55% smaller than the one show in Fig.5.14(a). The birefringence effect in this fibre is very weak as a result of the less deformed structure.

5.2.5 Intuitive explanation of dispersion in PBGFs

Upon comparing the dispersion of HC-PBGFs (Fig.5.13) and SC-PBGFs (Fig.4.16), we can see similarities as well as differences. A simple explanation [48] is helpful to understand these dispersion curves. The common features are at the band edges. In both cases, the absolute value of dispersion is increasing dramatically as the wavelength moves towards the band edge and the sign of the dispersion is always anomalous(normal) at the long(short) wavelength edge. This feature can be explained by the fact that as the wavelength moves towards to the band edge the guided mode starts to penetrate into the cladding where the high index intrusions are located and as a result the group index (n_g) of the guided mode increases. The derivative of n_g, proportional to the dispersion D, will give us the dispersion behaviour at the band edges(Fig.5.15(a)). In the central part of the band where the dispersion introduced band-gap effects is flat and small, other effects including waveguide dispersion and material dispersion have to be taken into account.

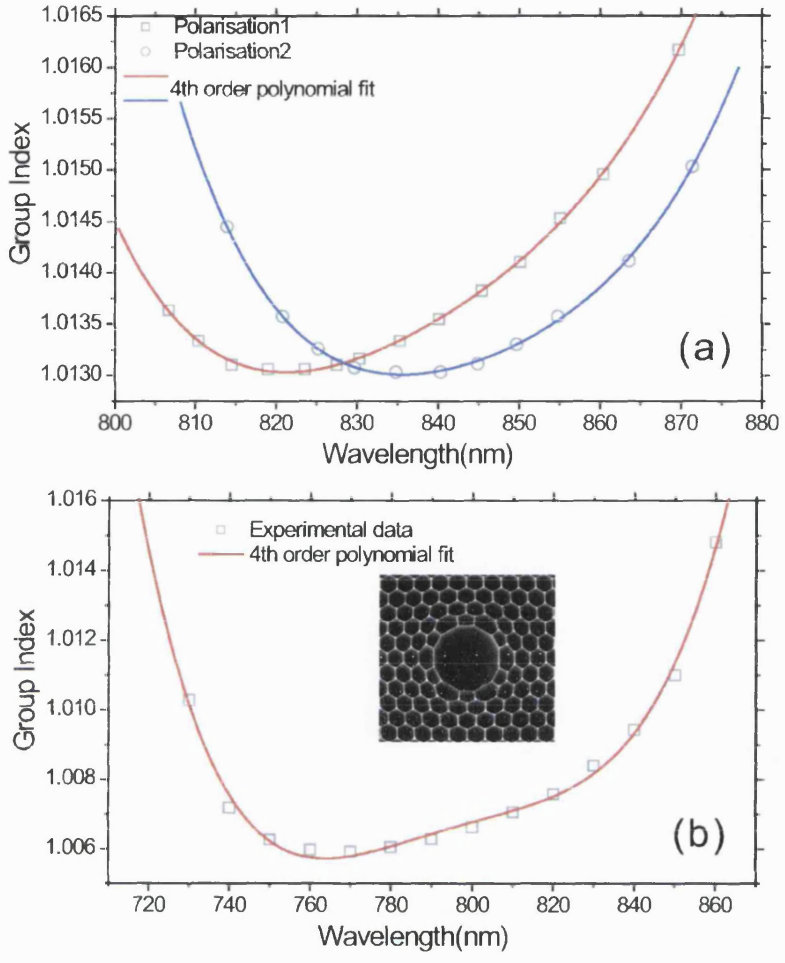

Figure 5.14: (a) Measured group indices of the fibre shown in Fig.5.4. (b) Measured group indices of a fibre with less deformation. The inset shows a SEM of the core area of the fibre sample.

Waveguide dispersion is caused by the fact that the light is propagating in a confined space. A hollow waveguide inside an ideal conductor is a simple example to illustrate such effect. Suppose the hollow waveguide has a circular cross section with radius a. The boundary conditions require that the light field is zero at the interface of the hollow core and the ideal conductor. So we have:

$$a\sqrt{k_0^2 - \beta^2} = j_0$$

where j_0 is the root of the first kind of Bessel function $J_0(x)$ [5]. From the above

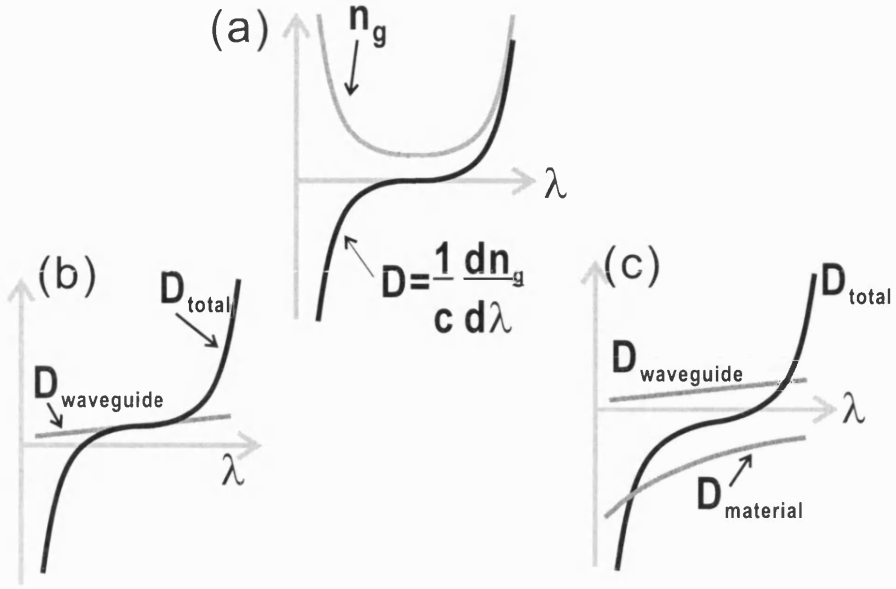

Figure 5.15: Schematic plot to explain the dispersion effects in band-gap fibres

equation we can find out the GVD:

$$\beta_2 = \frac{d^2\beta}{d\omega^2} \approx -\frac{cj_0^2}{a^2\omega^3} \quad or \quad D \approx \frac{j_0^2}{4\pi^2 a^2 c}\lambda$$

where c is the speed of light in the vacuum. Here we assumed that $\sqrt{k_0^2 - \beta^2} << k_0$. We can see that waveguide dispersion, caused by the size of the core, is always anomalous. In HC-PBGFs, the material effects can be neglected and the waveguide dispersion is dominant in the central part of the bandgap(Fig.5.15(b)) which leads to the zero-GVD wavelength being blue shifted. For the case of SC-PBGFs, in the wavelength range of our investigation, the core material has a big normal dispersion which is dominant in the central part of the bandgap and it has a red-shifted zero-GVD wavelength(Fig5.15(c)).

5.3 Low-loss HC-PBGFs and Surface modes

During the time of my Ph.D. research, the attenuation of HC-PBGFs dropped dramatically, especially in the wavelength band of 1500nm. Fig.5.16 shows two extraordinary examples [48][49] of low-loss HC-PBGFs.

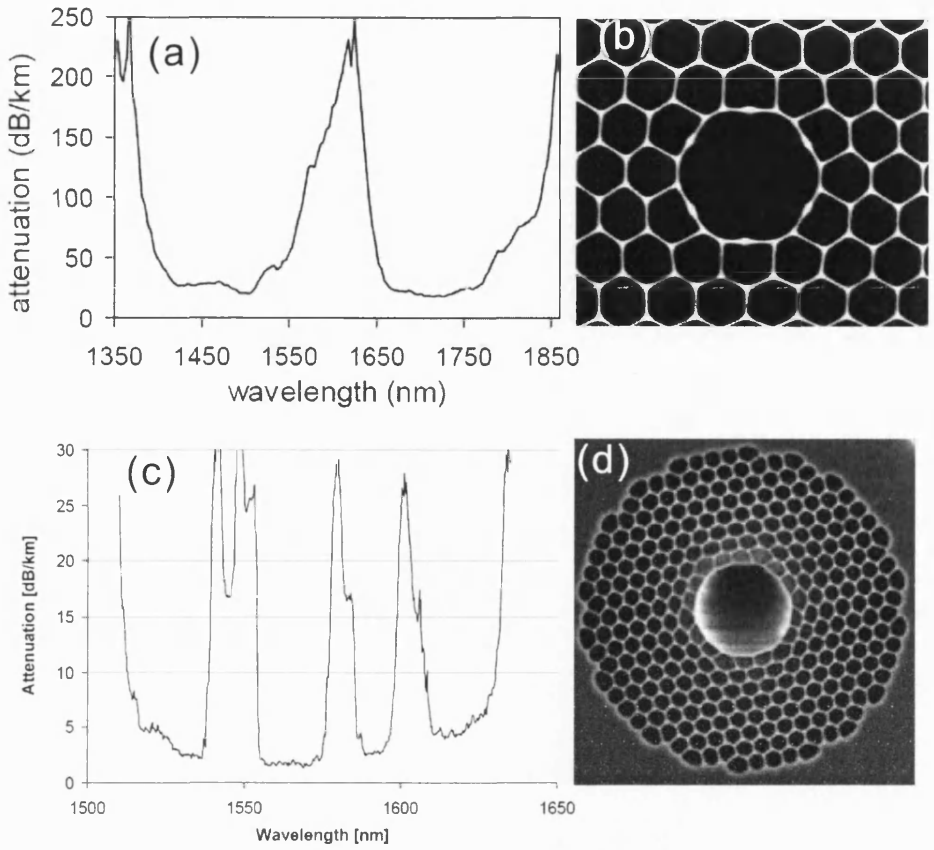

Figure 5.16: (a) and (b) A low-loss HC-PBGF from Corning Ltd. (a) Optical attenuation as a function of wavelength for the 65m long HC-PBGF. The loss feature between 1550nm and 1650nm is attributed to surface modes [50]. (b) SEM of the HC-PBGF profile [50]. (c) and (d) A 1.7dB/km HC-PBGF with a bigger core from BlazePhotonics Ltd. [49]. (c) Attenuation of a 200m long HC-PBGF with a 19-cell core. (d) a SEM of the 19-cell HC-PBGF.

Although the fibres shown in Fig.5.16 have different core structures, they have something in common. In both cases there are some high attenuation peaks within the transmission band. These high attenuation peaks are caused by the core structure and deformation of the cladding around the core. In Fig.5.3, we have shown that the cladding structure of HC-PBGFs can be seen as many identical resonators (composed of one blob and three strands). This uniformity was broken around the core area where some resonators with abnormal shapes must be introduced to form the core boundary. Some of the resonant modes introduced by those abnormal resonators, called surface modes, are located in the bandgap and cross with the guided core modes. At crossing points (corresponding with those high attenuation peaks), strong coupling occurs between core modes

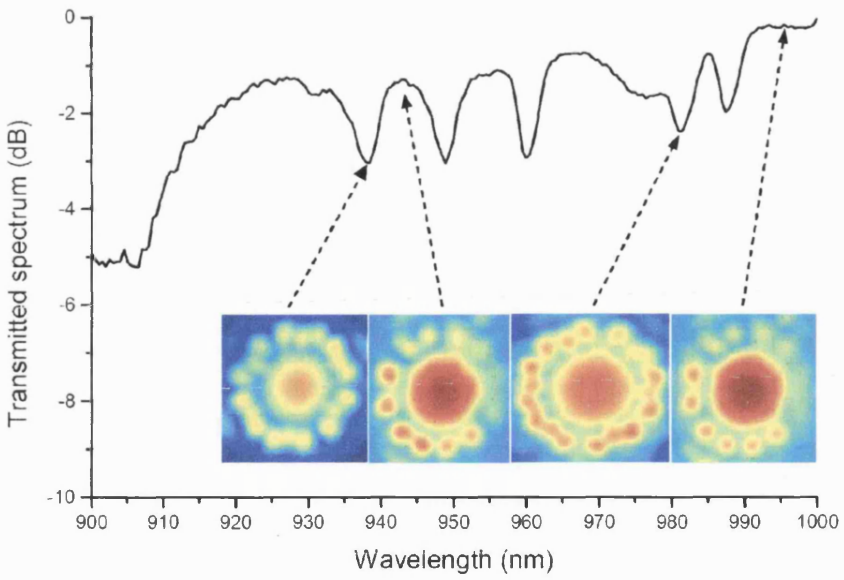

Figure 5.17: Surface mode effects of a HC-PBGF with guidance band at 1000nm [56]. The inset shows the observed near-field intensity maps at the fibre output at wavelengths corresponding to some of the intensity minima and maxima.

and surface modes which are expected to be lossy because of the scattering effects in the silica structure. Fig.5.17, from my colleague Dr. G. Humbert who has done a lot of experimental investigation on surface modes [56], shows the surface mode effects of a fibre sample with transmission band centred at 1μm.

Surface modes are an intrinsic problem of all HC-PBGFs with a circular core boundary. There are fibre core designs [50][57][58] that have been proposed for avoiding the existance of the surface modes while other proposals have been made to utilise these surface mode effects to exploit novel nonlinear effects in HC-PBGFs [59][60]. On the other hand, SC-PBGFs as shown in Chaper 4 should be free from surface mode effects because there are no defects between the core the cladding. The fact that surface mode features cannot be seen on the transmission spectrum of our fibre (Fig.5.5) does not mean that the fibre has no surface modes. The surface modes of our fibre sample may be located near the band boundary where the attenuation level is high, which makes the attenuation peaks caused by surface modes invisible.

5.4 Summary

Photonic bandgap air-core fibres can be fabricated for operation at wavelengths as short as 850nm. Losses in these fibres are already at an acceptable level for many applications, and are expected to fall further with improvement in the fabrication processes. The lowest loss mode has a quasi-Gaussian field pattern, and is strongly peaked in the air core. Higher-order modes can be observed in short fibre lengths, but have substantially higher losses. Coupling from the fundamental to the higher-order modes is weak, even when the fibre is bent or twisted. A core ellipticity of $10-15\%$ causes a splitting between the fundamental polarization modes of the order of a 10^{-4}.

The width of the bandgap in these fibres makes them suitable for delivery of ultrashort optical pulses from laser systems in this wavelength band. The GVD of the low-loss mode is low and anomalous over most of the low loss band, passing through zero towards the shorter-wavelength edge of the band gap. Although higher-order dispersion will ultimately limit linear delivery of ultrashort pulses along HC-PBGFs with simple structures, it is likely that more sophisticated designs can be devised in which higher-order dispersion can be more finely controlled.

Chapter 6

Soliton propagation in hollow-core photonic bandgap fibres

As described in Chapter 5, HC-PBGFs display a range of unusual optical properties. One of the unique properties is that more than 90% of the total transmitted power is confined in the hollow core. As a result, the performance of such fibres is substantially free from nonlinearities, one of the limitations imposed by the solid core material found in all conventional fibres. In conventional fibres, ultra-short high-power laser pulses are very rapidly torn apart by self-phase modulation and Raman scattering, combined with the group-velocity dispersion (GVD) of the fibre. In this chapter we will discuss the nonlinear effects of HC-PBGFs and demonstrate the delivery of ultra-short high-power laser pulses by using the soliton effect in HC-PBGFs in a spectral region centred at 800nm , where the material dispersion of bulk silica is such as to preclude the transmission of short optical pulses through any significant length of solid-core fibre, even in the absence of nonlinear effects.

At the same time we were performing our soliton experiments in HC-PBGFs at an 800nm wavelength, Ouzounov et al, cooperating with Corning Ltd., reported a demonstration of soliton pulse delivery over a short piece of HC-PBGF without significant temporal distortion at 1500nm wavelength [61]. We chose on 800nm wavelength, at which suitable HC-PBGFs for soliton experiments were very dif-

ficult to make at that time, because not only are Ti:sapphire lasers the most widely used ultra-short laser sources but also the potential of applications in this wavelength range is huge.

6.1 Properties of the fibre

The linear properties of PBGF's for the 800nm band have been described in Chapter 4. In this section we just focus on those fibre properties which are directly relevant to the experiments being described, specifically the GVD and the Kerr nonlinear effect of self-phase modulation. A SEM image of the fibre used in the experiment is shown in Fig.6.1. The GVD in our fibre is shown in Fig.6.2, along with the attenuation and the measured group index. The attenuation was measured by using the cut-back method with a tungsten-halogen lamp and an optical spectrum analyser. The minimum attenuation, at a wavelength of 800nm, is about 270dB/km which is much higher than the attenuation previously reported for a similar type of fibre at a 1500nm wavelength [49][48] because of the strong inverse dependence of the scattering processes on wavelength [62]. The effective area of the guided mode is about 27μm. The group index was measured using a low-coherence Michelson interferometer equipped with a supercontinuum source as described in Section 3.4.3. The minimum of 1.006 is located on the short-wavelength side of the low-loss band, and the index increases slowly towards the centre of the transmission band. The GVD curve is derived from a fit to the measured group index data, and is anomalous (with positive slope) over most of the low-loss window, enabling soliton propagation over much of this band. Our experiments were performed around 800nm, where the GVD was around 140ps/nm/km (or 47.5ps^2/km) and the dispersion slope was 3ps/nm^2/km.

6.2 SPM at zero-GVD wavelength

Before the soliton experiment, we launched 200fs pulses from an unamplified Ti:Sapphire laser at the zero-dispersion wavelength to observe the self-phase-modulation (SPM) effect from which we could estimate the value of the nonlinear coefficient γ. The zero-GVD wavelength of the fibre sample shown above is below

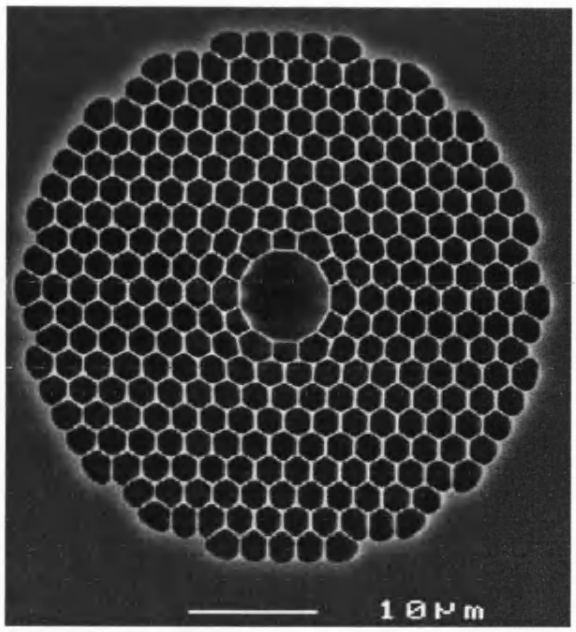

Figure 6.1: SEM image of the fibre used in the soliton experiment

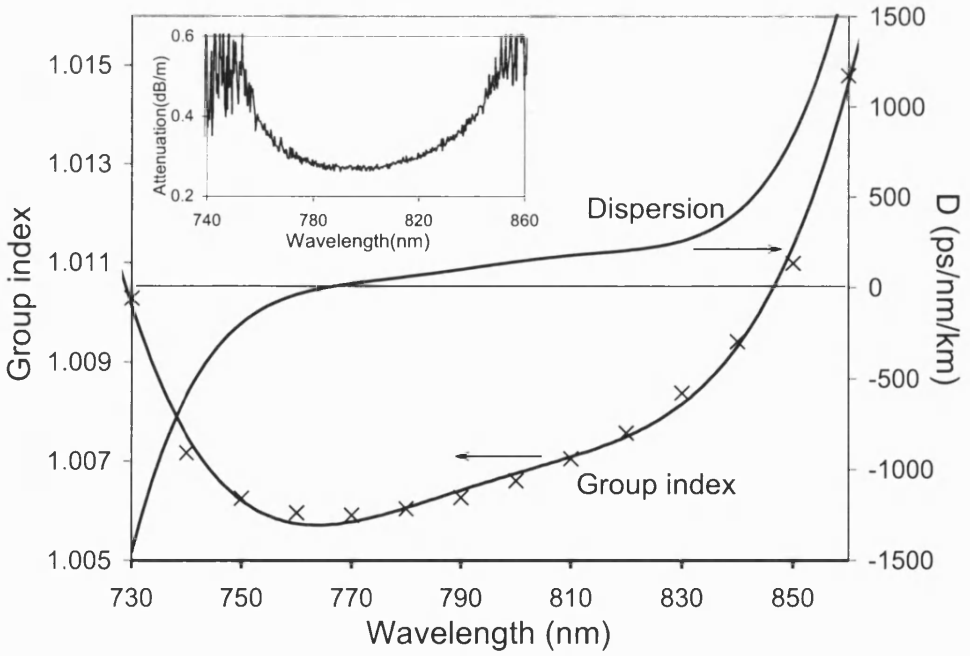

Figure 6.2: Measured group index and group-velocity dispersion (GVD), with inset showing the fibre attenuation. The measured group index points are indicated by crosses: the line is a fit to the data points and is used to derive the dispersion curve.

760nm, where our Ti:Sapphire laser is unstable without changing components, so we used a similar fibre sample with shifted zero-GVD wavelength (793nm) instead. Both of the fibre samples were drawn from the same preform and they have very similar linear properties. Fig.6.3 shows the output spectrum after transmission along 2m of fibre at different input powers. The most notable feature is the splitting of the output spectrum. The higher the input power, the greater the spectral splitting. As the central wavelength of the input pulses is changed slightly, the splitting point stays at the zero-GVD wavelength. As shown in section 2.3.4, the nonlinear phase shift caused by SPM is:

$$\phi = \gamma P_0 L_{eff} \tag{6.1}$$

where L_{eff} is the effective length, which is not only limited by the loss of the fibre, but also the dispersion length. In our case the L_{eff} is less than 2m. Away from the zero-GVD point the absolute value of the fibre's dispersion increases quickly, and the dispersion length becomes very short and the nonlinear phase shift decreases dramatically. This is the reason why the spectrum splitting point, where the biggest nonlinear phase shift accumulates, is fixed by the zero-dispersion wavelength. The asymmetry of the spectrum splitting is because of the presence of high-order dispersions [63]. Compared with the typical spectra of SPM in [10], the spectrum splitting in Fig.6.3 represents a nonlinear phase shift of about 1.2π, which gives us an estimated nonlinear coefficient γ of about 0.1/W/km.

6.3 Soliton experiments

By using the γ estimated from the SPM experiment, we need at least a 10^2kW peak power to observe soliton effects in our fibre, which is beyond the capability of our Ti:Sapphire system, so our experiments were done by using a Q-switched regeneratively amplified Ti:Sapphire laser system at Heriot-Watt University.

Fig.6.4 shows the experiment setup. The pulses from the regenerative amplifier have a repetition rate of 5 kHz and a pulse length of 136fs. The output pulse length from the laser was roughly 1.5 times bandwidth limited. The central wavelength used was 796nm. The pulse power was controlled in our experiments(Fig.6.4) using a half-waveplate($\lambda/2$) and a polarizing beamsplitter

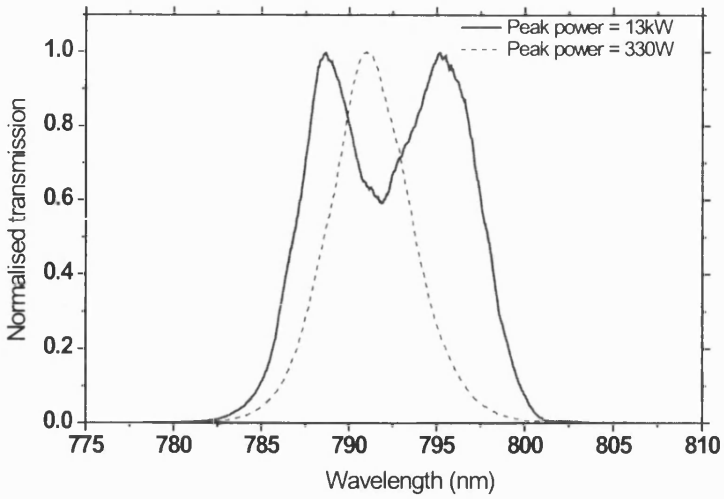

Figure 6.3: SPM-induced spectrum splitting

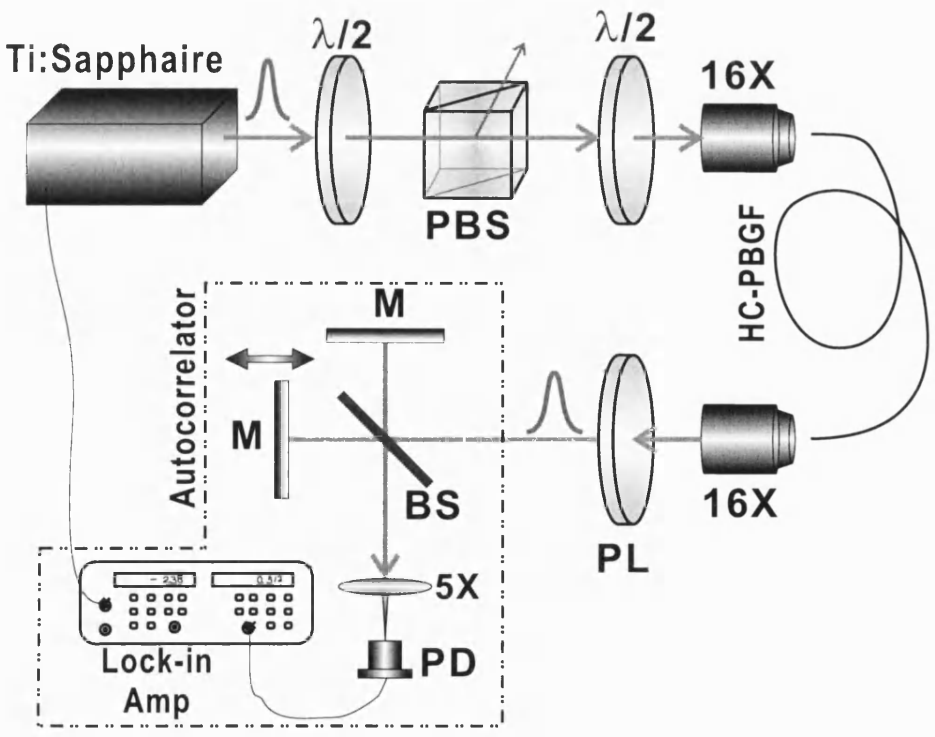

Figure 6.4: Experiment setup of the soliton transmission experiment.

(PBS). Although the core structure of the fibre used here is much more symmetrical than the one shown in Chapter 5, a small pulse splitting caused by the low birefringence can still be observed in the fibre, so another half-waveplate($\lambda/2$) was used in front of the fibre to rotate the polarisation of the input pulse to one of the principle axes of the fibre. Light was coupled into 5m of HC-PBGF via a 16× AR-coated aspheric lens(NA=0.25) from Newfocus. The coupling efficiency obtained was $25-30\%$ and the maximum output pulse energy was 320nJ after transmission through 5m of fibre before the fibre end was damaged. The experiments described here were performed at output pulse energies of up to 120nJ. At the fibre output, the beam collimated by an other 16× AR-coated aspheric lens was sent into an autocorrelator [64] before which a polariser (PL) was used to get a cleaner autocorrelation trace.

The autocorrelator, based on a Michelson interferometer (Fig.6.4), had a GaAsP photodiode (PD) as a 2-photon detector [65][66]. Because of the low repetition rate of the regenerative amplifier, the average 2-photon signal was very low and had to be amplified by a lock-in amplifier which was triggered by the regenerative amplifier. The moveable mirror was mounted on a translation stage with 5μm resolution. As we manually scanned the mirror position, which is proportional to a time delay of the two arms of the Michelson interferometer, the amplified 2-photon signal was recorded to form the intensity autocorrelation trace. The measured full widths at half maxima (FWHM) of the autocorrelation traces as a function of the output pulse energy and a comparison of the pulse profile of the soliton and the input pulse are shown in Fig.6.5.

The 5m length of PBGF used in our experiments had an effective length of 4.2m and a dispersion length for 136fs pulses of 0.15m. At low power, linear pulse propagation is expected to lead to an output pulse length of over 5ps because of the GVD of the fibre. As the input power is increased we observe dramatic pulse shortening to a minimum autocorrelation width of around 450fs at an output pulse energy of 60nJ. The output pulse length then remains almost constant towards higher pulse energies. Assuming a hyperbolic secant squared ($sech^2$) pulse shape which has a deconvolution factor of 1.55, we estimate an output pulse length of about 311fs, which is 2.3 times longer than the input pulse length 136fs (assuming a Gaussian shape, deconvolution factor 1.41). Observed output spectra for selected energies are shown in Fig.6.6. The spectra show both a solitonic and a dispersive component indicating that the short pulse sits on a pedestal of dis-

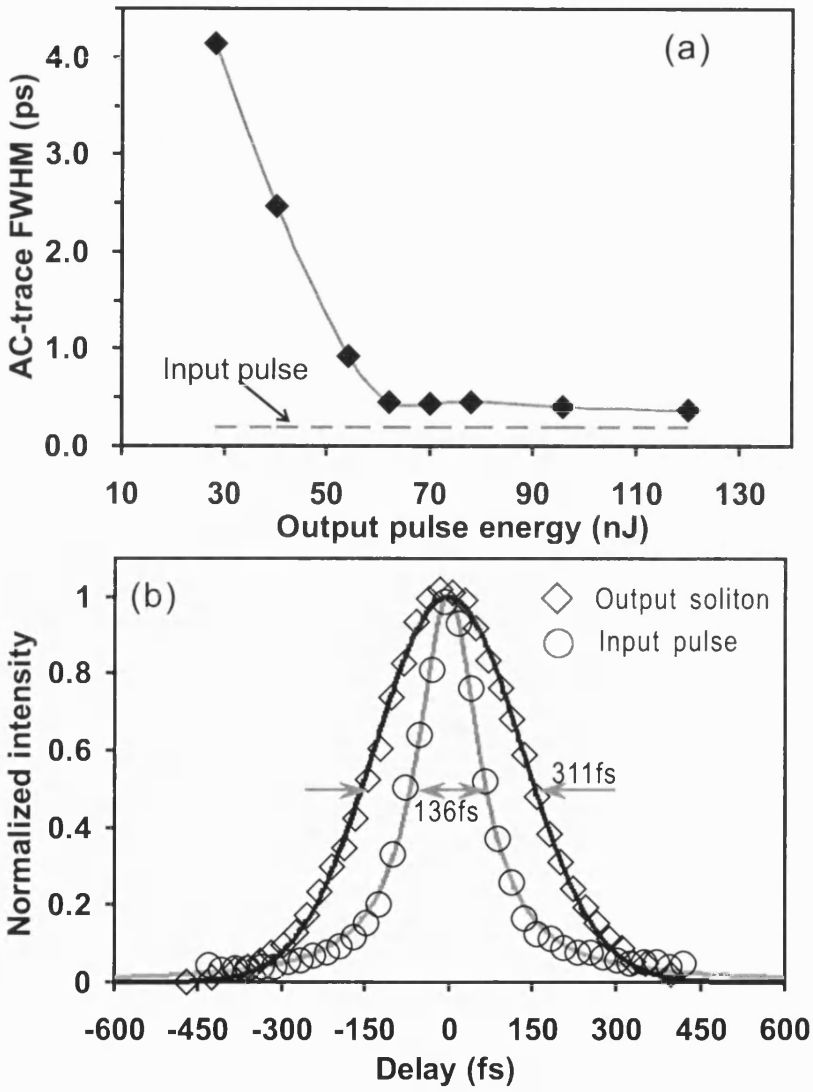

Figure 6.5: (a) Measured pulse autocorrelation FWHM as a function of output pulse energy. (b) Comparison of the input and soliton profiles.

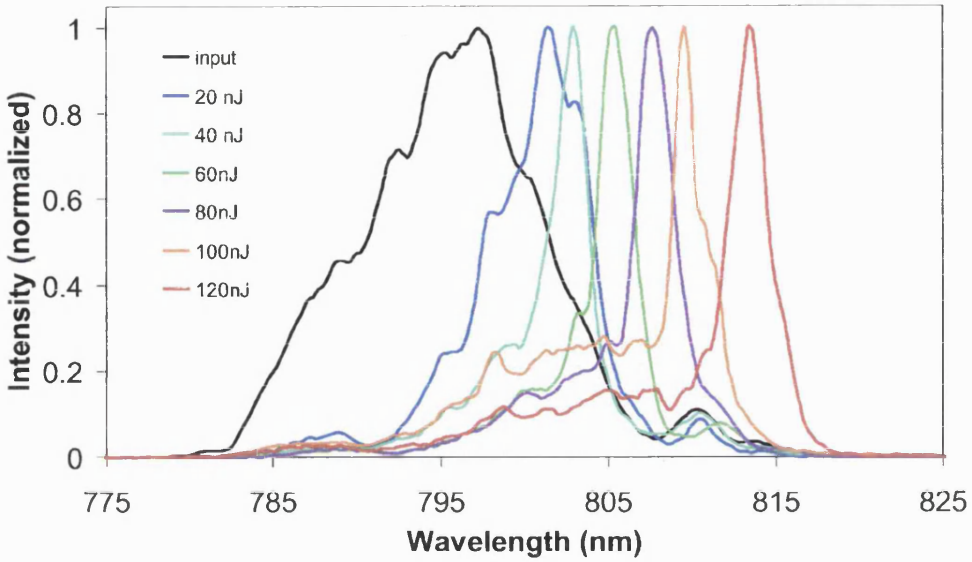

Figure 6.6: measured spectra at different output power

persed energy which is related to the Raman effects [10]. The solitonic component has a bandwidth of roughly 3nm, resulting in a time bandwidth product (TBP) of 0.36. Comparing this with the transform limited TBP of a $sech^2$ pulse which is 0.31, it implies that the compressed pulses shown in Fig.6.5 are virtually chirp free. From the spectral distribution, we estimate that more than 80% of the input energy is coupled to the soliton at a 60nJ pulse energy. The solitonic component is shifted to lower frequencies due to the intrapulse Raman scattering [67][13][14], higher power resulting in a greater wavelength change. However, even over 5m of fibre and at 120nJ output power, the soliton remains well within the low-loss window of the PBGF.

6.4 Contribution from silica to nonlinearity

From the result of the soliton experiment, we know that the fundamental soliton energy in our fibre is about 60nJ. By using Equ.2.33 and the parameters of our fibre, we can again evaluate the nonlinear coefficient γ of our fibre, which is about 0.02/W/km. This value is much lower than the 0.1/W/km estimated from the SPM experiment (Section 6.2). Although the two γ values were estimated in

different experiments using different fibres, the difference between the two γ is out of the experimental error range. There must be something to explain such difference.

Unlike in conventional fibre, the guided mode of a HC-PBGF covers both silica and air regions, which have widely differing values of n_2. The nonlinear phase shift in hollow-core fibres has been variously attributed to exclusively the nonlinear refractive index of air [61] ($n_2 = 2.9^{-23} m^2/W$) and that of silica [68] ($n_2 = 2.4^{-20} m^2/W$). As the light is concentrated mainly in the air, which has a much lower value of n_2 than the silica, it is not obvious a priori which material contributes most to the observed nonlinear phase shift. To make it clear, we have to go back to the original expression of nonlinear phase shift as shown in Equ.2.23:

$$\begin{aligned}\Delta n_{NL} &= \frac{3}{8n}|A(z,t)|^2 \iint_{-\infty}^{\infty} \chi^{(3)} |F(x,y)|^4 \, dxdy \\ &= \frac{3}{8n}|A(z,t)|^2 (\chi^{(3)}_{air} \iint_{air} |F(x,y)|^4 \, dxdy + \chi^{(3)}_{silica} \iint_{silica} |F(x,y)|^4 \, dxdy)\end{aligned}$$

or:

$$\Delta n_{NL} = P \sum_i \frac{n_2^i}{A_{eff}^i} \quad (i = silica, air) \tag{6.2}$$

where

$$P = |A(z,t)|^2 \quad n_2^i = \frac{3}{8n_i}\chi_i^{(3)} \quad A_{eff}^i = \frac{1}{\iint_i |F(x,y)|^4 \, dxdy}$$

$F(x,y)$ is the normalised field distribution function and A_{eff}^i is the material effective area which is normalised by the peak power of the light field. For the part of the light travelling in air, $A_{eff}^{air} \approx (\iint_{-\infty}^{\infty} |F(x,y)|^4 \, dxdy)^{-1}$, which is the effective area that we had in the case of conventional fibre or index-guiding PCFs, and can be approximated by πw^2 if a Gaussian distribution is assumed (w is the width parameter). For the light travelling in silica, $A_{eff}^{silica} = (\iint_{silica} |F(x,y)|^4 \, dxdy)^{-1}$ which is orders of magnitude larger than A_{eff}^{air}. So A_{eff}^{silica} is only a physical definition but not the real silica area covered by the guided light. Part of the reason for the enlarged effective area in silica is that Eqa.6.2 uses only the peak power of the whole light field P, which is much bigger than that inside silica, so a much enlarged effective area of silica has to be used as a compensation.

Eq.6.2 enables us independently to compute the contribution to the nonlinear

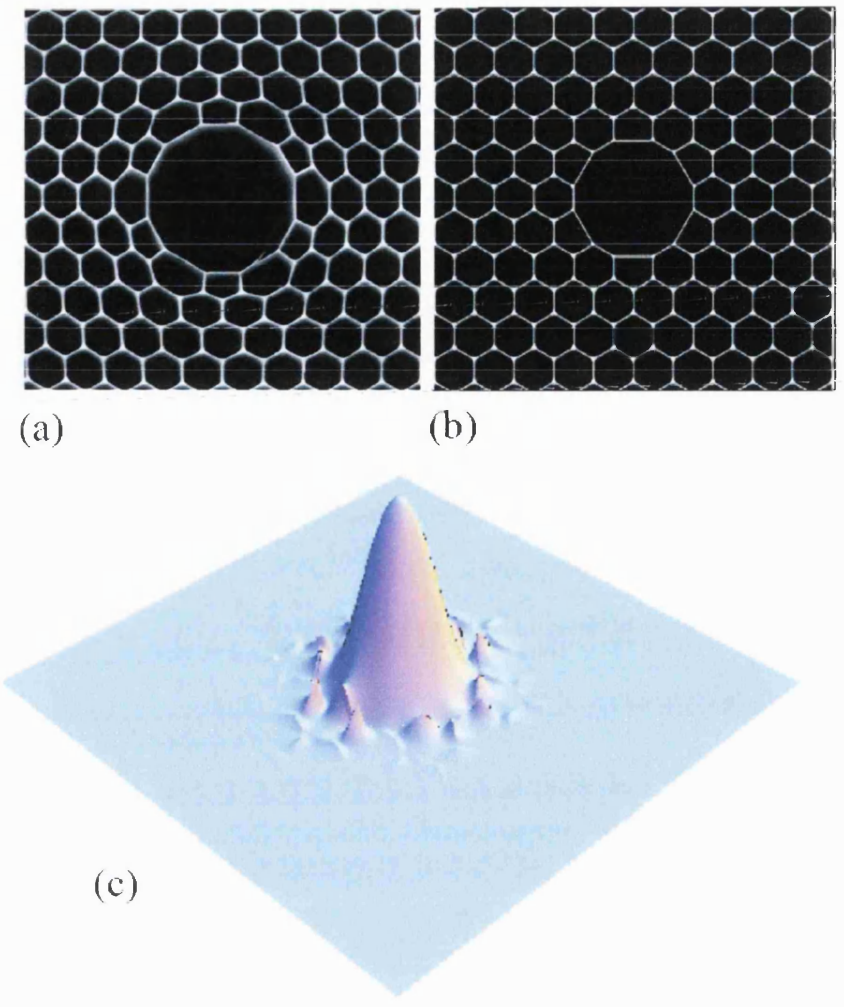

Figure 6.7: Actual (a) and modelled (b) fibre cross-sections, showing the region around the core. (c) shows the intensity pattern of the fundamental guided mode used in the modelling of the nonlinear response

phase shift arising from the glass and from the air numerically. Our collaborators from BlazePhotonics Ltd. modelled our fibre by using the structure shown in Fig.6.7(b) which is derived from the real structure shown in Fig.6.7(a). The modelled structure has a 92% air fraction in the cladding and a core formed by a seven-unit-cell defect. The pitch in the cladding was taken as 2.33μm and the thickness of the struts in the cladding was 70nm. The silica interstices seen in the actual fibres were reproduced in the model using arcs of circles. The core wall thickness was defined to be 76nm. The core of our experimental fibre became distorted during the fibre draw, which resulted in a rather larger core

than seven unit cells, but this distortion was neglected in the numerical modelling. Modelling of the structure in Fig.6.7(b) gives a band gap in imperfect agreement with the experimental observations, but within the uncertainties of the structural parameters. The modelled bandgap covered the wavelength range from 780nm to 970nm, and had an avoided crossing of a surface mode in the middle. This surface mode was not observed experimentally (Fig.6.2 inset), perhaps because of the distortions around the core. The intensity pattern of the fundamental core-guided mode in the structure is shown in Fig.6.7(c), at a wavelength of 801nm. 99% of the energy travels in air, with just 1% of the energy located in the glass. The highest intensity occurring in the glass is 16% of the peak intensity in the centre of the hollow core.

Evaluation of Equ.6.2 using the data shown in Fig.6.7(c) gives us

$$\frac{\Delta n_{NL}^{silica}}{P} = 1.28 \times 10^{-12} W^{-1} \quad and \quad \frac{\Delta n_{NL}^{air}}{P} = 1.78 \times 10^{-12} W^{-1}$$

By using

$$\gamma = \frac{k_0}{P} \sum_i \Delta n_{NL}^i$$

we have a γ value of 0.024/W/km which is in agreement with our soliton experiment result within the uncertainties of the structural parameters. The discrepancy of γ values evaluated from the SPM experiment and the soliton experiment can be attributed to the fact that the air and the glass appear to be making roughly equal contributions to the nonlinearity of our fibre, because the part of nonlinearity from silica is very sensitive to the change of A_{eff}^{silica}, which is a function of wavelength. At the zero-GVD wavelength where the SPM experiment was done, the loss is higher than that at the bottom of the band where the soliton experiment was done. As discussed in Section5.2.1, the main loss mechanism in our 800nm HC-PBGFs is the surface roughness of the silica structure. The increased loss at the zero-GVD wavelength indicates that at this wavelength the core mode has more overlap with the silica structure, which makes the silica contribute more to the total nonlinearity of the fibre. Such nonlinear coefficient change with wavelength was not observed in the first demonstration of soliton formation in a HC-PBGF at 1500nm [61]. In their experiment, a low-loss (13dB/km) HC-PBGF was used, which implies that the guided mode has much less overlap with the silica structure. Therefore, the silica structure has little effect on the total nonlinearity of their fibre sample.

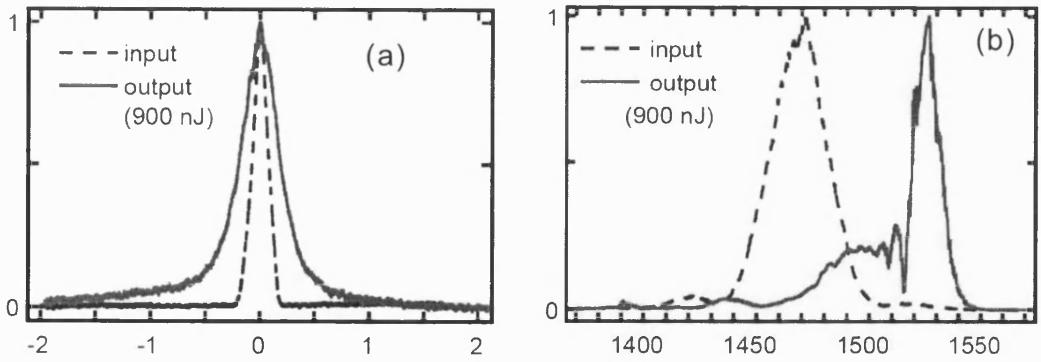

Figure 6.8: Some results from [61]. (a) Intensity autocorrelation traces of input and output pulses for a pulse energy of 900nJ. (b) Input and output pulse spectra for a pulse with an energy of 900nJ propagating in air.

6.5 The effect of pulse broadening caused by Raman gain profile of the air

Fig.6.8 shows the intensity autocorrelation trace and spectrum of the solitons observed in [61]. Comparing with our results (Fig.6.5 and Fig.6.6), we can see that in both experiments the Raman shifted optical solitons, compared with input pulses, were broadened in time and compressed in frequency. However, such phenomena disappeared when the HC-PBGF was filled with a noble gas (Xe) [61] which does not have Raman activity. This indicates that it is the Raman property of the gas in HC-PBGFs that limits the bandwidth of the solitons. Fig.6.9 shows a comparison of the Raman gain spectrum of silica and N_2 which is dominant within the bandwidth of the input pulses (about 4.4THz for a Gaussian 100fs pulse). The peak of the N_2 Raman gain spectrum is located at 1.8THz below the pump (corresponding to a wavelength width of 3.8nm at 800nm or 13.4nm at 1500nm), which is responsible for the observed soliton bandwidth (3.0nm in our case, 13.4nm in [61]).

6.6 Physical damage to the fibre end face

One of the limitations in this experiment is physical damage on the fibre end caused by the intense laser pulses. In the experiment, as we slowly increased the

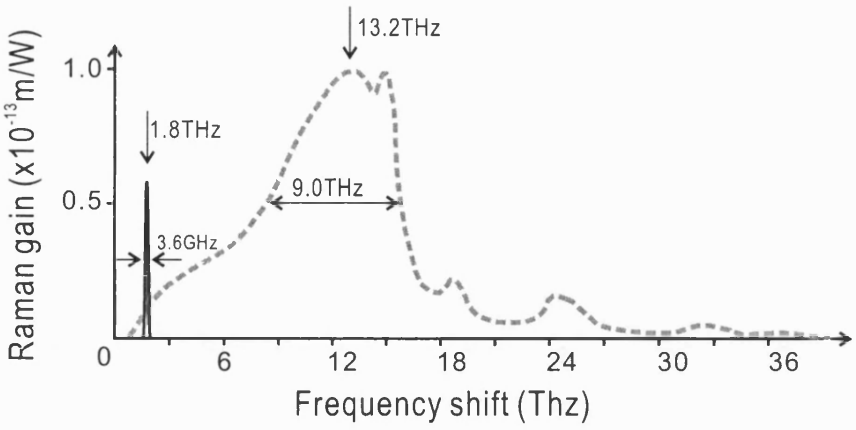

Figure 6.9: Raman gain spectra of pure silica (the dashed curve) and N_2 (the solid curve).

input power, at a certain point the output power suddenly dropped dramatically and it was not recoverable. Fig.6.10 shows what happened at this point. The extremely thin silica strand was broken by the laser pulse. One of the reasons is that the spatial profile of the laser pulses is not perfect(Beam Quality Factor $M^2 = 1.5$), so that not all the power couples into the core mode. Also the numerical aperture of the coupling lens is not perfectly matched with the fibre. All the uncoupled energy strikes on the thin silica strand and will cause physical damages at high power. By improving the coupling efficiency, the maximum transmitted power could be increased.

6.7 summary

We have demonstrated delivery of pulses from a regeneratively amplified Titanium-Sapphire laser system over 5m of HC-PBGF with an output pulse length of 300fs. The nonlinear phase shift required for soliton formation arises roughly equally from the nonlinear refractive index of air and the relatively small overlap of the guided mode with the more nonlinear silica. Based on our experimental and numerical results, we anticipate that it will be possible to deliver femtosecond pulses from an unamplified laser oscillator using a HC-PBGF with a somewhat smaller core and a lower air-filling-fraction cladding.

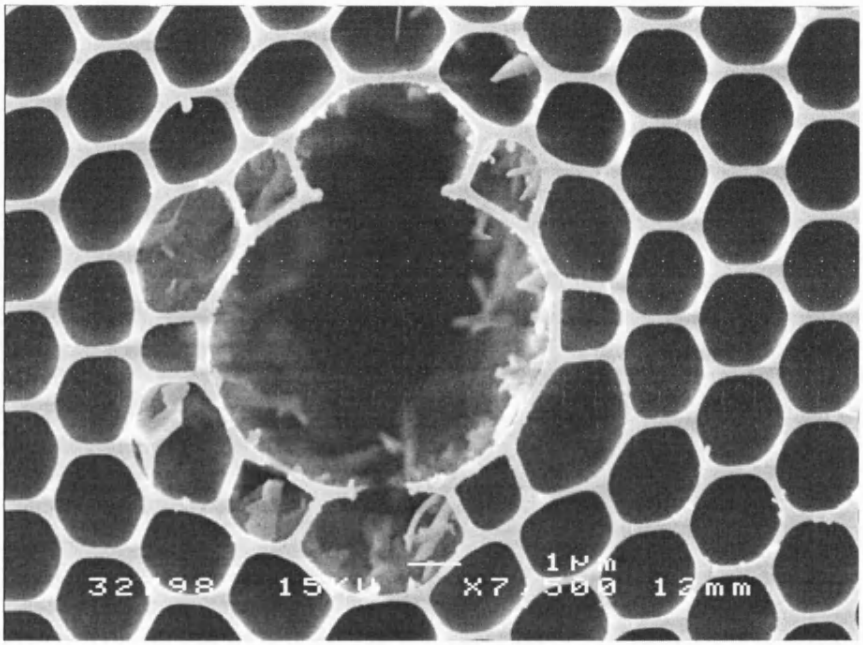

Figure 6.10: Damaged fibre end face. The pulse energy was about 300nJ when the damage was made.

Chapter 7

Soliton Self-Frequency Shift Cancellation in index-guiding Photonic Crystal Fibres

As described in Section 2.3.5, optical solitons are self-localized pulses with their temporal dispersion suppressed by the action of a nonlinear medium in which they propagate [69]. In a Raman-active medium, like silica, short ($<$ 1ps) solitons are continuously red-shifted [13] because the low-frequency spectral components of the soliton experience Raman gain due to being pumped by the high-frequency components. Although this has been considered an immutable feature of sub-picosecond soliton propagation in optical fibres, we show in this chapter that the soliton self-frequency shift (SSFS) can be cancelled in a silica-core index-guiding PCF with a suitably engineered dispersion profile.

7.1 Cherenkov radiation of a moving charged particle

Cherenkov radiation [70] is electromagnetic radiation emitted by a charged particle moving linearly in a dispersive medium at a constant speed greater than the phase velocity of light in the medium. Fig.7.1 illustrates the physical ex-

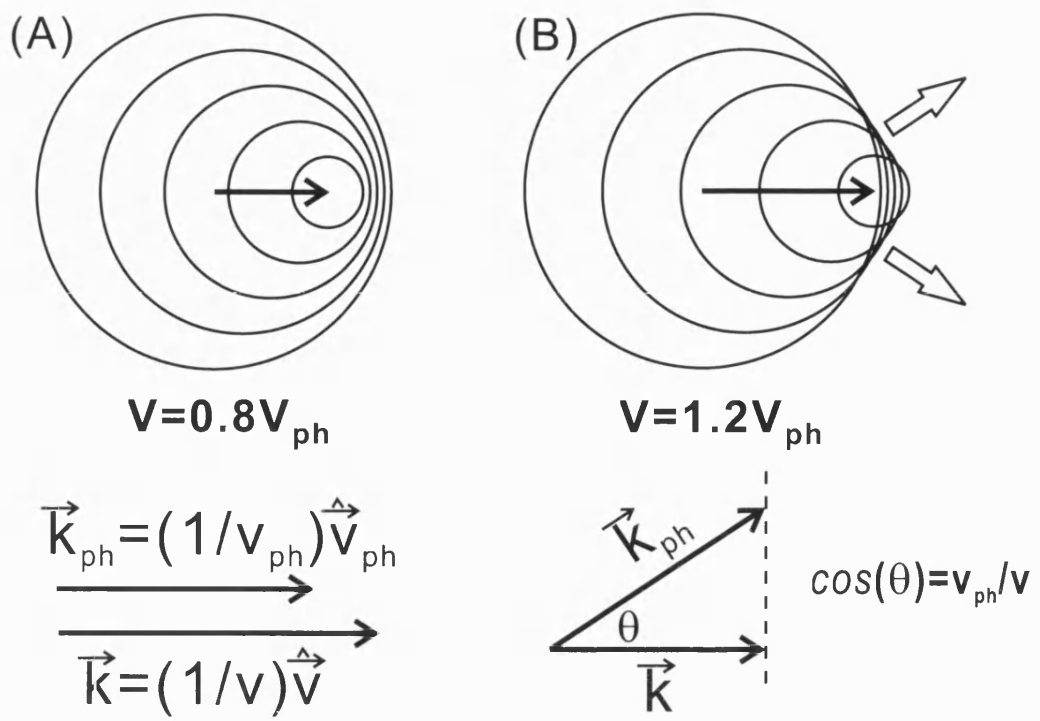

Figure 7.1: Schematic illustration of Cherenkov radiation.

planation of the Cherenkov radiation. As a charged particles travels, electrons in the atoms of the surrounding medium will be displaced and polarised by the passing charged particle. Each displaced electron, like a point source, will emit light waves as they restore themselves to equilibrium after the disruption has passed. All the light waves emitted by the disrupted electrons along the trajectory of the moving particle are coherent and they have to be added up to unveil the macroscopic effects. When the speed of the particle (v) is smaller than the phase velocity of the light in the medium ($v_{ph} = c/n$, c is the speed of light in the vacuum and n is the refractive index of the medium), all these light waves interfere destructively and no radiation is formed. However, when $v > v_{ph}$ the light waves interfere constructively and form a directional radiation. If we define a wavevector of the particle, $\vec{k}$, by $\vec{k} = (1/v)\hat{\vec{v}}$ ($\hat{\vec{v}}$ is the unit vector along the direction of movement of the particle), then the radiation direction θ is determined by the phase matching condition on the direction of the particle movement, $\hat{\vec{v}}$, i.e. $cos(\theta) = |\vec{k}|/|\vec{k_{ph}}| = v_{ph}/v$, where $\vec{k_{ph}}$ is the wavevector of the radiation wave.

7.2 Cherenkov radiation emitted by solitons in optical fibres caused by higher-order dispersions

From Section 2.3.5, we know that if we neglect higher-order (3rd-order and higher) dispersion and scattering process the governing equation to describe pulse propagation in a fibre is:

$$\frac{\partial A}{\partial z} + \frac{i\beta_2}{2}\frac{\partial^2 A}{\partial T^2} = i\gamma |A|^2 A \tag{7.1}$$

When the fibre has an anomalous dispersion ($\beta_2 < 0$), Equ.7.1 has a soliton solution:

$$A(z,T) = \sqrt{P} sech(T/T_0) e^{i\gamma P z/2} \tag{7.2}$$

where T_0 and P are the time duration and peak power of the soliton respectively and they satisfy $\gamma P T_0^2/|\beta_2| = 1$. When a soliton propagates along the fibre, only a collective phase, described by the argument of $e^{i\gamma Pz/2}$, changes. Such a collective phase, when divided by z, can be considered as an effective propagation constant of the soliton, i.e. $\beta_{sol} = \gamma P/2$. We should notice that β_{sol} is only proportional to the peak power of the soliton and does not change with frequency. The propagation constant of a linear wave in the fibre is described by the dispersion relation of the fibre, i.e. $\beta_{lin}(\omega) = \frac{1}{2}\beta_2(\omega-\omega_0)^2$ (ω_0 is the central frequency of the soliton). The linear part of the dispersion relation, $\beta_0 + \beta_1(\omega - \omega_0)$, does not appear in the expression of β_{sol} and β_{lin}, because ω_0 is used as the reference frequency and a retarded frame (a frame moving with the pulse) is adopted in Equ.7.1. It is apparent that $\beta_{sol} > 0 \geq \beta_{lin}$ (Fig.7.2(A)) or in other words the phase matching condition can never be satisfied when higher-order dispersions are absent. Therefore, no energy is transferred between the solitons and the linear waves. This is the main reason for the robustness of optical solitons.

In reality, higher-order dispersions are always present in optical fibres, and it is possible to fulfil the phase matching condition between solitons and linear waves. For example, if we include only 3rd-order dispersion (β_3) and neglect other higher-order dispersions, then the dispersion relation of the linear wave will be $\beta_{lin}(\omega) = \frac{1}{2}\beta_2(\omega - \omega_0)^2 + \frac{1}{6}\beta_3(\omega - \omega_0)^3$. Here we assume that compared with the 2nd-order dispersion effect the 3rd-order dispersion effect is small, i.e. $L_{D2} << L_{D3}$ (the mth-order dispersion length $L_{Dm} \equiv T_0^m/|\beta_m|$ is used as a

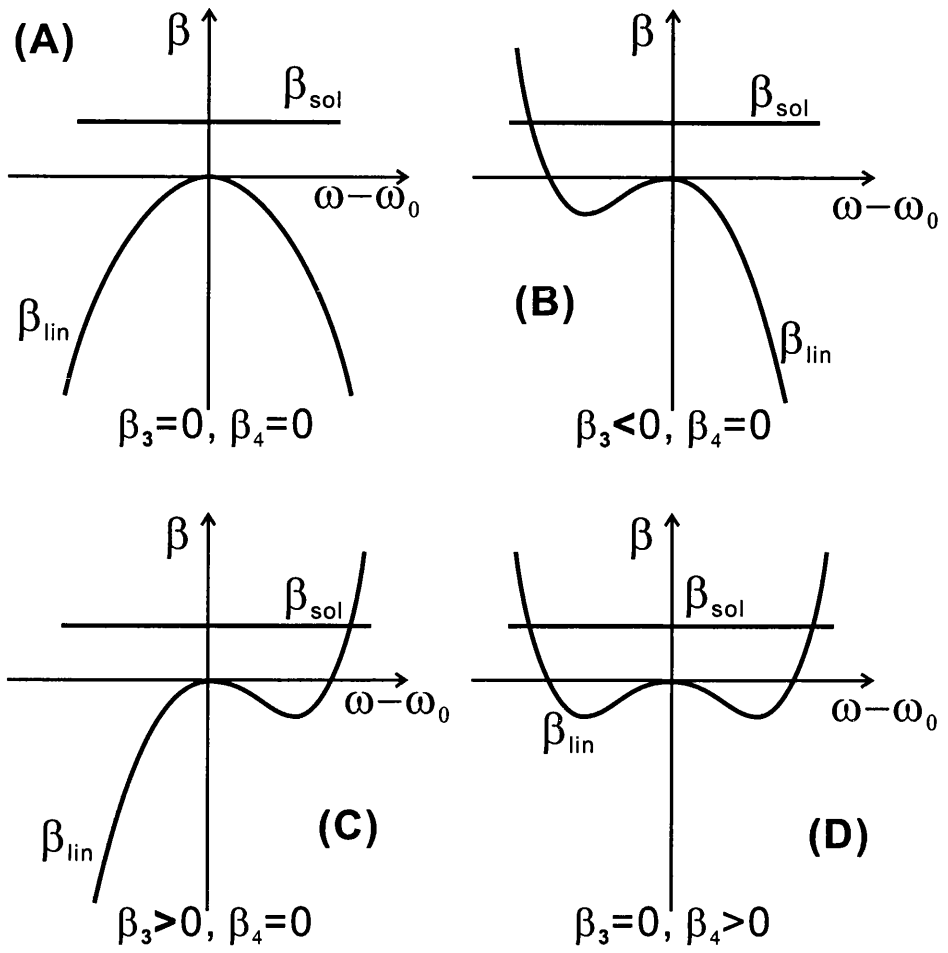

Figure 7.2: Phase matching plot under different conditions.

measure of the dispersion effects [10]), so we can treat the higher-order dispersions as perturbations. Under the perturbations of β_3, the first-order corrections to the soliton do not change its amplitude, width, and shape [71], so the effective propagation constant of the soliton $\beta_{sol} = \gamma P/2$ is also unchanged. Then the phase matching condition will be:

$$\frac{1}{2}\gamma P = \frac{1}{2}\beta_2(\omega - \omega_0)^2 + \frac{1}{6}\beta_3(\omega - \omega_0)^3 \tag{7.3}$$

The solution of the above equation is

$$\omega_r \approx \omega_0 + 3(\frac{|\beta_2|}{\beta_3} + \frac{\beta_3 \gamma P}{\beta_2^2}) \tag{7.4}$$

where ω_r is the phase matching frequency. Fig.7.2 shows schematically the disper-

sion relations of solitons and linear waves under different higher-order dispersion configurations to illustrate the phase matching process.

At the phase matching frequency, energy transfer between soliton and linear wave is unavoidable and manifests as a radiation. Theoretical analysis [72] shows that the intensity of this radiation is proportional to the intensity of the soliton at the radiation frequency ω_r, so it is the spectral tail of the soliton at ω_r that boosts the radiation.

Just like classical Cherenkov radiation, the radiated waves will have some impact on the soliton. In classical Cherenkov radiation, the interaction between the charged particle and the radiation wave is governed by the requirement of conservation of total momentum. The counterpart in the case of solitons propagation in fibre is the conservation of the spectral "centre of mass" (ω_c), i.e.:

$$\omega_c \equiv \frac{\int_{-\infty}^{+\infty} \omega |A(\omega, z)|^2 d\omega}{\int_{-\infty}^{+\infty} |A(\omega, z)|^2 d\omega} = constant \tag{7.5}$$

Here if we regard $|A(\omega, z)|^2$ as the "mass" distribution over ω, then Equ.7.5 is an equivalent of the conservation of "momentum" in the frequency domain. As a result, the soliton will be "recoiled" (in frequency) by the radiated linear waves [73][74]. For example, in Fig.7.2(B) with a negative 3rd-order dispersion ($\beta_3 < 0$), the radiation wavelength ω_r is located at the lower frequency side of the soliton, so the soliton will be recoiled to the higher frequency side. The "recoil force" is proportional to $(\omega_r - \omega_0)Q_r$ (Q_r is the radiation energy). If only even orders of higher-order dispersion are present in the fibre (Fig.7.2(D)), the soliton will radiate in both frequency directions symmetrically and the recoil force will be cancelled out, so the soliton does not shift in frequency.

7.3 Soliton self-frequency shift compensation by the Cherenkov radiation

It is important to note that the above discussion disregards the soliton self-frequency shift (SSFS) due to the Raman effect, which is a well known process in which photons cascade their energy to photons at a longer wavelength through

scattering from optical phonons. However, the Raman response of silica accounts for about 20% of the overall nonlinear response in case of femtosecond pulses [69], so it cannot be neglected.

When $|\omega_r - \omega_0| >> \Delta\omega_s$ ($\Delta\omega_s$ is the band width of the soliton), it has been shown theoretically [72] that solitons emitting Cherenkov radiation lose energy slowly (i.e., non-exponentially) with increasing propagation distance z, and the SSFS effect is dominant [75]. This is usually true when the soliton is well away from the zero-dispersion frequency. From Equ.7.4 we know that the frequency of the Cherenkov radiation ω_r approaches the central soliton frequency ω_0 close to the zero-GVD frequency, where energy exchange between the soliton and the resonant dispersive wave is expected to reach its maximum. This is because the amplitude of the emitted radiation is primarily determined by the spectral amplitude of the soliton at the radiation frequency ω_r and increases exponentially as ω_r approaches ω_0. Therefore, in the region around the zero-GVD frequency, both Cherenkov radiation and SSFS effects have to be taken into account. The overall effect is dramatically different depending on the slope of the GVD curve (i.e. the sign of β_3).

The situation for a positive GVD slope ($\beta_3 > 0$) near the zero-GVD frequency is relatively simple. When $\beta_3 > 0$, the radiation wave is at the high frequency side of the soliton (i.e. blue-shifted) and pushes the soliton to lower frequency, which is the same direction as that of the SSFS effect, so the Cherenkov effect and SSFS effect act cooperatively, driving the soliton away from the zero-GVD frequency (See Fig.7.3). As the soliton is away from the zero-GVD frequency, the Cherenkov effect can be neglected.

The situation for a negative GVD slope ($\beta_3 < 0$) is much more interesting. As shown in Fig.7.3, as the soliton approaches the zero-GVD frequency, the red-shifted radiation wave pushes the soliton toward the blue side of the spectrum, which is against the direction of the SSFS effect. Furthermore, the energy of the radiated wave has an exponential dependence on $1/|\omega_r - \omega_0|$ and increases dramatically as the soliton red-shifts toward the zero-GVD frequency because of SSFS, whose effect is directly proportional to $|\beta_2| z T_0^{-4}$ [10]. Thus, there exists the possibility of a balance between the red frequency shift due to the Raman effect and the blue frequency shift coming from the radiation pressure [29][75].

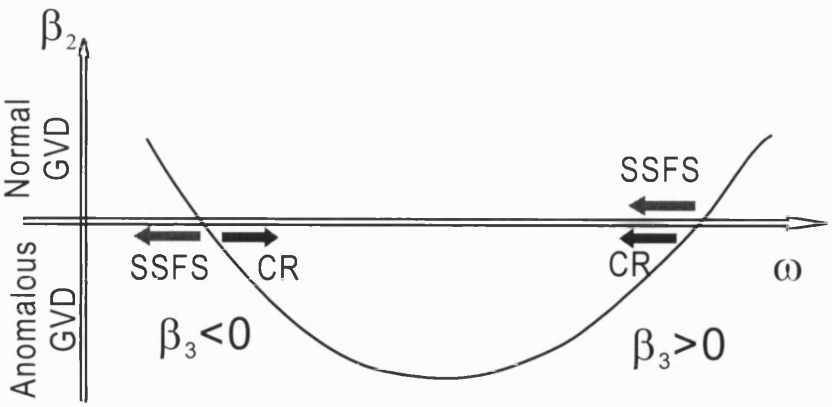

Figure 7.3: A sketch to show the effects of SSFS and Cherenkov radiation under different signs of β_3

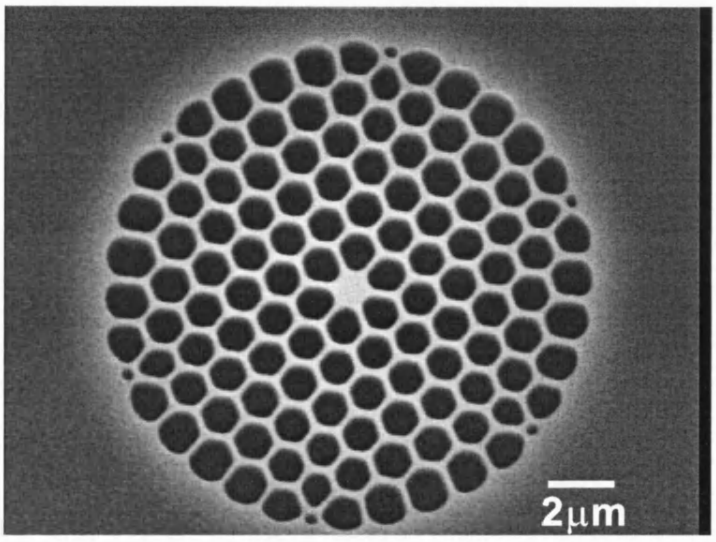

Figure 7.4: A SEM image of the PCF used in the SSFS cancellation experiments.

7.4 Experimental results

7.4.1 A fibre with large negative dispersion slope

In order to demonstrate the theoretically predicted effect of the compensation of SSFS by Cherenkov radiation, a fibre with negative dispersion slope crossing the zero-dispersion point is desired. Within the visible and near-IR frequency

range, conventional step index fibres have only one zero-dispersion point and the dispersion slope, dominated by the material dispersion, is overwhelmingly positive. Under such conditions, SSFS is inevitable. In Section 3.2, I have shown that a index-guiding PCF with very small core not only has a high nonlinearity but also has a pronounced waveguide dispersion, which gives the fibre one more zero-dispersion wavelength with negative dispersion slope. Fig.7.4 shows a SEM image of the PCF we employed in our experiment. The fibre has a very small core diameter of 1.2μm. Although the fibre has a relatively large d/Λ ratio, the loss measurement with bending does not show any cut-off effects, so the fibre is single mode within the frequency range we are interested in. Fig.7.5 shows the measured dispersion, which has two zero-dispersion wavelengths (0.57μm ($2\pi \times$ 526THz) and 1.31μm ($2\pi \times$ 229THz)).

7.4.2 Observation of strong Cherenkov radiation and SSFS compensation

We carried out a series of experiments in which we launched optical pulses into the small core PCF. The laser source used in the experiments was a mode-locked Ti:sapphire system emitting 200fs pulses at a wavelength of 0.86μm. A half-wave plate was used to rotate the polarisation of the input laser to one of the principle axes of the PCF, which has an intrinsic birefringence due to its small core and departure from perfect symmetry during the fabrication process. Then the fibre length was progressively reduced, and the output spectrum was recorded for each length with an optical spectrum analyser (OSA).

Fig.7.6 shows the measurement results for input pulses with peak powers of 75W propagating in the PCF from 0.4cm to 500cm. For the chosen pump wavelength, which is far away from the zero-GVD point, the dispersion slope is still positive, and the radiation fields are very weak, because of the large detuning from the soliton frequency. Therefore, the soliton dynamics shown in Fig.7.7 are dominated by the SSFS effect.

Fig.7.7 shows the measurement results for input pulses with peak powers of 230W propagating in the PCF from 0.4cm to 400cm. By increasing the soliton peak power, we effectively accelerate the SSFS process and enable solitons to approach

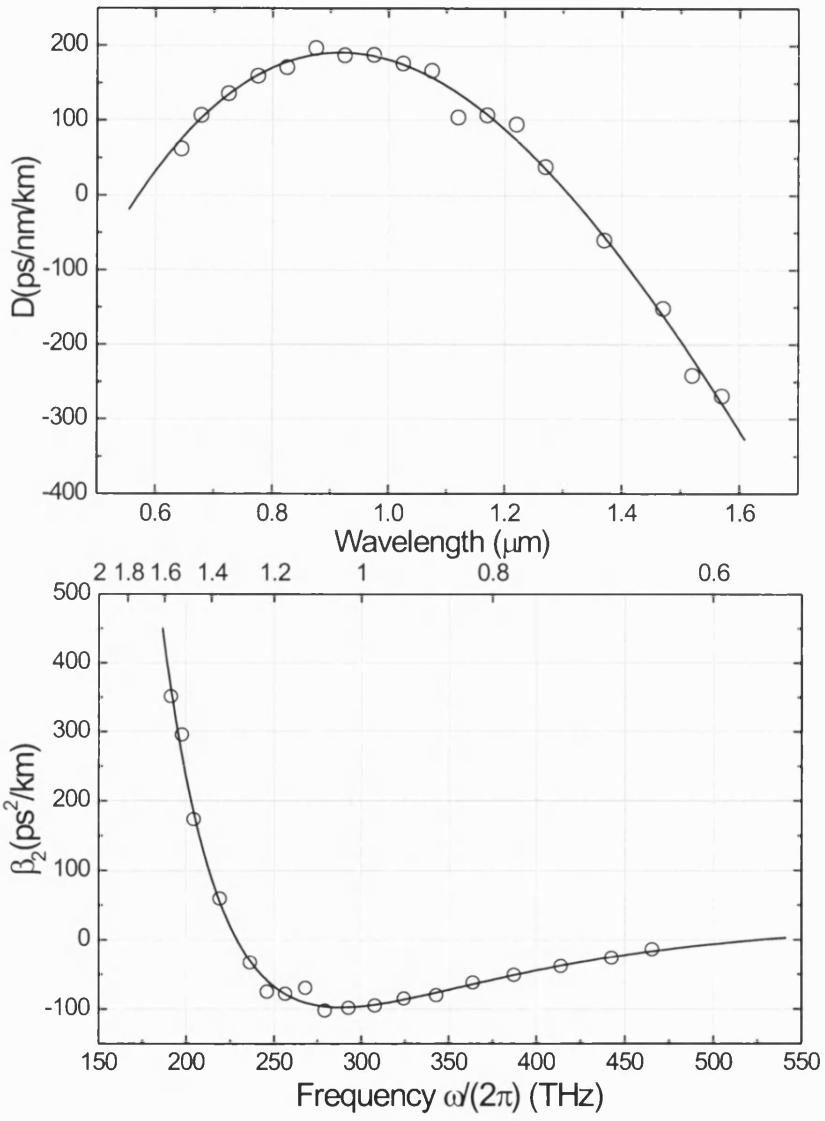

Figure 7.5: The measured group velocity dispersion shown as both D parameter and β_2.

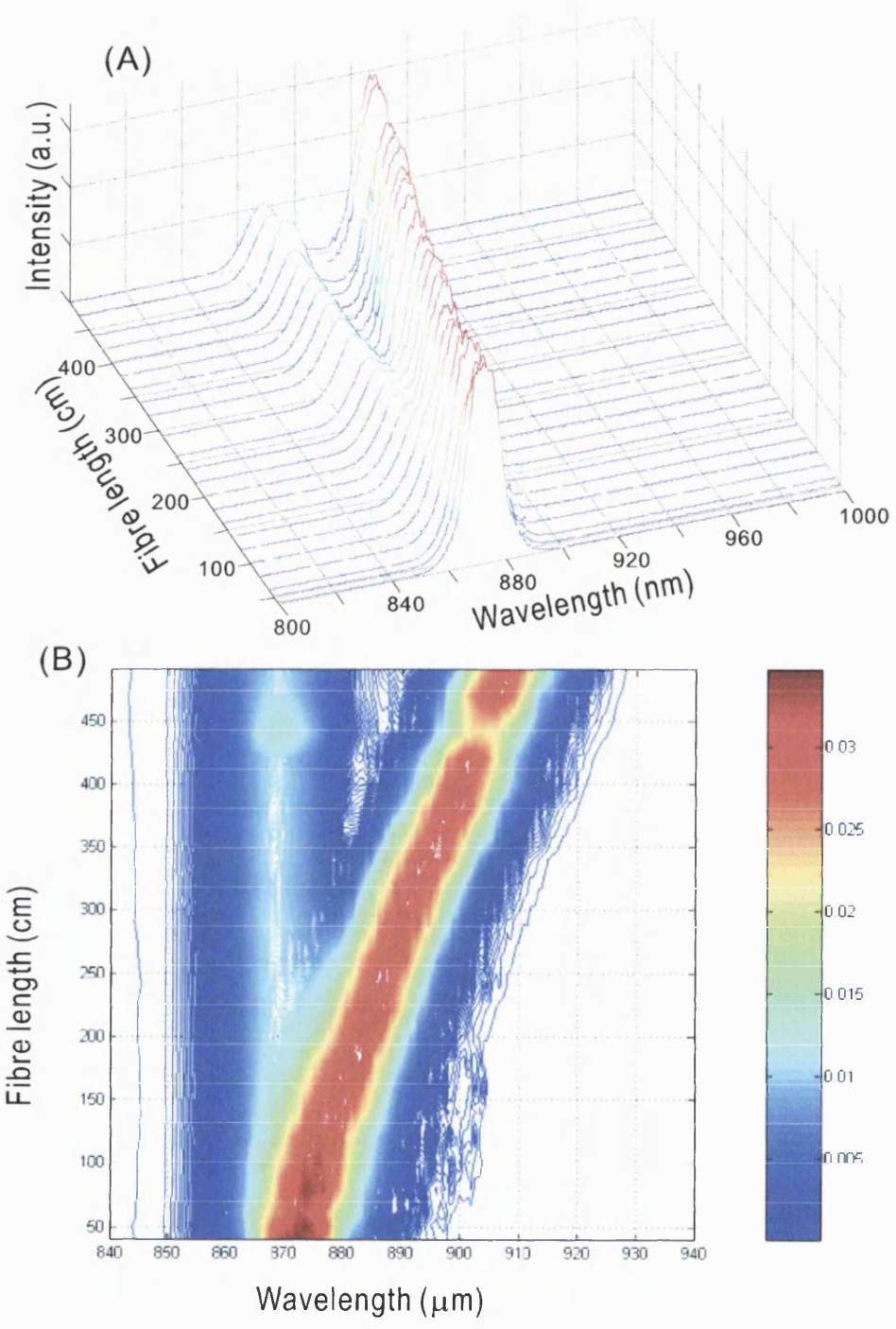

Figure 7.6: SSFS is dominant when the soliton is well away from the zero-GVD. (A) The spectrum measured at different fibre lengths. (B) The interpolated contour plot is based on the data from (A). The input peak power is 75W.

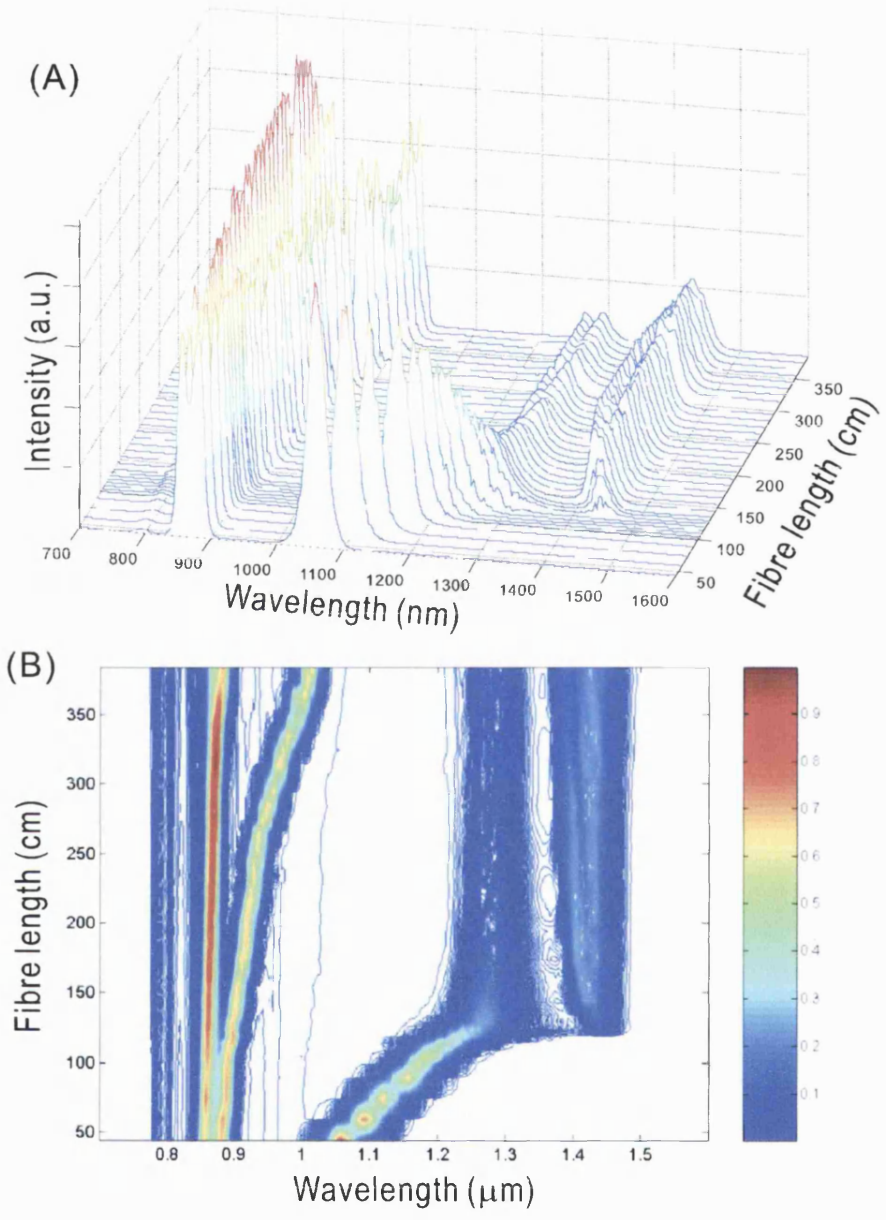

Figure 7.7: SSFS compensation by the strong Cherenkov radiation near the zero-GVD point with a negative GVD slope. (A) The spectrum measured at different fibre lengths. (B) The interpolated contour plot based on the data from (A). The input peak power is 230W.

the zero-GVD point quickly without increasing the fibre length. The initial conditions of the input pulses correspond to the 4th-order soliton power. From Fig.7.7, we can see that initially under the perturbation of Raman effects the input pulse splits into two Raman-shifting solitons with different peak powers. The one with bigger peak power shifts faster. As it approaches the zero-GVD point (1.31μm), a strong red-shifted radiation wave develops and the red shifting of the soliton is almost stopped completely. We should notice that the radiation wave already existed when the soliton was still well away from the zero-GVD point, but it was so weak that it was not visible in Fig.7.7. After the SSFS cancelling point (corresponding fibre length about 120cm), the energy of the soliton transfers to the radiation wave quickly and from Equ.7.4 (and also Fig.7.2(B)) we know that red detuning of the radiation will slightly decrease, which can be seen from Fig.7.7(B) (the edge of the radiation wave shifts slowly toward the soliton frequency). Although it is not completely stopped, the red-shifting of the soliton is largely compensated by the strong Cherenkov radiation.

To examine the robustness of the observed SSFS compensation effect, we put even more power (input pulse peak power 450W) into the fibre, which enables us to observe the behaviour of the second Raman shifted soliton. The results are shown in Fig.7.8(A)(B). Although the peak power is a bit lower than the first Raman-shifted soliton, it is clear that the SSFS of the second Raman-shifted soliton is compensated almost at the same wavelength as the first Raman-shifted soliton. This means that this SSFS compensation effect is not sensitive to the properties of the incoming solitons. Fig.7.9 shows the numerical simulation done by my colleague Dr. D.V. Skryabin, who predicted this SSFS compensation effect theoretically [29], using the parameters gathered from our experiments. The pattern of the soliton behaviour shown in our experiments is clearly seen from this simulation.

7.5 Conclusion

The excellent agreement between our experimental results and the numerical predictions shows that we have identified and observed an efficient mechanism to amplify the Cherenkov radiation emitted by optical solitons, which leads to the cancellation of the SSFS. The detuning between the solitonic pump and the

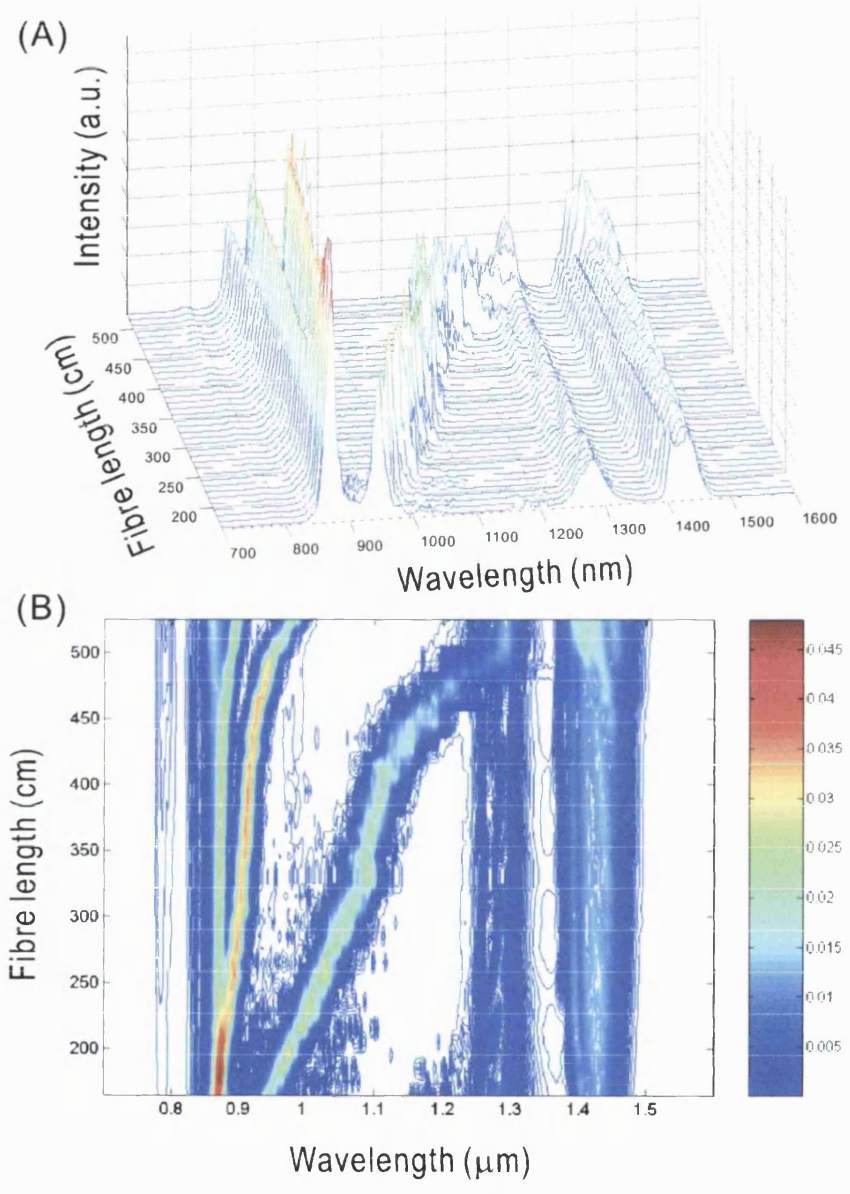

Figure 7.8: The observation of the second Raman-shifted soliton experiencing the SSFS compensation effect. The input peak power is 450W.

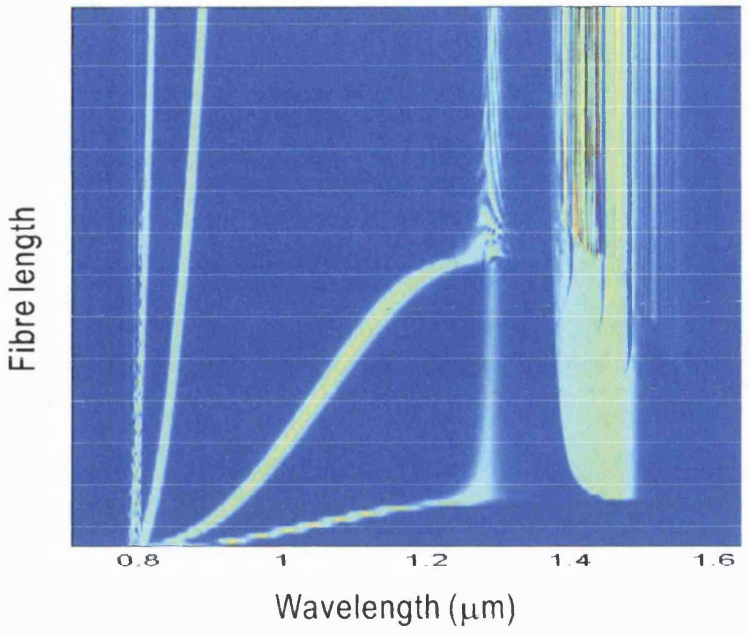

Figure 7.9: Numerical simulation shows the behaviour of a 200fs soliton as it propagates along the fibre approaching the zero-GVD point with negative dispersion slope. The fibre parameters used in the simulation are from the experimental data (7.5).

Cherenkov radiation in the frequency-locking regime is sensitive to the value of the GVD slope, which is determined by the PCF geometry. This suggests the possibility of tailoring the latter to achieve a desired output frequency, and thus, of developing a family of optical parametric amplifiers based on solitonic Cherenkov radiation. Such amplifiers would be useful for inline applications, despite the low nonlinearity and limited operating wavelength range, when compared with periodically poled $LiNbO_3$.

The effect of the SSFS compensation described above is very robust and has been observed for a broad range of pump frequencies and powers. The most likely reason why it has not been previously identified is that in telecommunication fibres, for commonly used frequencies, the radiation is always on the higher frequency side of the soliton, so that the recoil and Raman effects act in the same spectral direction. The results of this work show how novel and unexpected effects can be discovered in PCFs due to the unique combination of their dispersive and nonlinear properties.

Chapter 8

Summary, and future work

This thesis described the fabrication and characterisation of linear and non-linear phenomena in photonic band-gap fibres. An novel soliton phenomenon in a index-guiding PCF was also presented. In this chapter we summarise the main conclusions of the work and describe future research directions.

All solid photonic band-gap fibres

We have investigated and fabricated all solid PBGFs for the first time. Experimental samples were fabricated using two different silicate glasses. Both rod-in-tube method and multiple stack method are shown to be feasible for this purpose. The linear optical properties of the fibre made by using the multiple stack method have been measured. Four lowest-order transmission bands are observed in the VIS-NIR wavelength range and show excellent agreement with the numerical simulation. The uniform deformation of the high-index rods (SF6) is investigated numerically and was found to have relatively little effect on the lower-orders of the transmission bands. Group index and group index dispersion are measured over the 2nd-order and 3rd-order bands. The red-shifted zero-GVD point indicates the core material dispersion contributes most to the dispersion at the central part of each transmission band. The relatively high attenuation measured in the fibres is attributed to the presence of small air bubbles trapped in the fibre structure during the drawing process. By improving this cause of loss

we expect to reduce the loss to the bulk material limit.

Linear properties of hollow-core photonic band-gap fibres

Linear properties of a HC-PBGF designed for use in the 850 nm wavelength region are investigated. A series of numerical simulations show that the "blobs" at the joints of the thin silica strands play an critical role in opening a band-gap in such structures. Losses in these fibres, mainly due to the scattering of the surface roughness of the silica structure, are already at an acceptable level for many applications. The lowest loss mode has a quasi-Gaussian field pattern, and is strongly peaked in the air core. Higher-order modes can be observed in short fibre lengths, but have substantially higher losses. Coupling from the fundamental to the higher-order modes is weak, even when the fibre is tightly bent or twisted. The GVD of the low-loss mode, measured by using both a time-domain method and a low-coherence interferometry method, is anomalous over most of the low loss band, passing through zero towards the shorter-wavelength edge of the band gap. An unintentional core ellipticity of $10 - 15\%$ causes a splitting between the fundamental polarization modes and the polarization beat length varies from 4mm to 13mm across the transmission band.

Soliton propagation in hollow-core photonic band-gap fibres

We have demonstrated delivery of 800nm pulses from a regeneratively amplified Titanium-Sapphire laser system over 5m of HC-PBGF with an output pulse length of 300fs and observed soliton formation at an output pulse energy of around 65nJ. The nonlinear coefficient of the fibre is estimated by observing the self-phase modulation effects at the zero-GVD point, and is smaller than that derived from the soliton experiments. The discrepancy can be explained by the fact that the nonlinear phase shift required for soliton formation arises roughly equally from the nonlinear refractive index of air and the relatively small overlap of the guided mode with the more nonlinear silica. The transmitted solitons are nearly transform limited and their band-width is limited by the Raman gain spectra of the gas inside the fibre, which is responsible for the red-shifting of the soliton spec-

trum. The physical damage to the fibre end-face at high pulse energy has also been shown.

Soliton self-frequency-shift compensation by Cherenkov radiation

We report the cancellation of the soliton self-frequency shift in a silica-core photonic crystal fibre with a negative dispersion slope. Experimental and numerical results show that stabilization of the soliton wavelength is accompanied by exponential growth of the red-shifted Cherenkov radiation emitted by the soliton. The soliton frequency locking is a result of the balance between the spectral recoil from the radiation and the SSFS from Raman effects. The SSFS compensation of a second Raman-shifted soliton was also demonstrated, which proves that the soliton locking frequency is largely determined by the PCF geometry and not sensitive to the properties of the incoming solitons.

Future work

The work presented in this thesis could be extended in many directions including:

The improvement on fabrication process is needed to reduce the loss of the all solid PBGFs. The multi-band transmission property of the all solid PBGFs makes it possible to match the group velocity at different transmission bands, which could be very interesting for certain nonlinear processes. The solid core of the solid PBGFs enable us to add doping in it and build new types of lasers and amplifiers. Surface modes, which are naturally absent from the all solid PBGFs, can be added into the fibre in a controllable way to give the fibre some special features.

Due to the significant improvement in the fabrication process of hollow-core PBGFs, the surface modes, which will affect the fibre performance, has been under intense investigation. Our work of soliton transmission implies the possibility to design the nonlinearity of HC-PBGFs by changing the cladding structure to meet the requests of real applications. Atom optics in HC-PBGFs has also

tract a lot interests all over the world.

Our demonstration of SSFS compensation suggests the possibility of tailoring the GVD profile of index-guiding PCFs to achieve a desired output frequency, and thus, of developing a family of optical parametric amplifiers based on the solitonic Cherenkov radiation.

References

[1] JD Joannopoulos, RD Meade, and JN Winn. *Photonic Crystals: Molding the Flow of Light.* Princeton University Press, 1995.

[2] P Russell. Photonic crystal fibers. *Science*, 299:358, 2003.

[3] JC Knight. Photonic crystal fibres. *Nature*, 424:847, 2003.

[4] KC Kao and GA Hockham. Dielectric-fibre surface waveguides for optical frequencies. *Proc. IEE*, 113:1151, 1966.

[5] Allan W Snyder and John D Love. *Optical Waveguide Theory.* Chapman and Hall, 1983.

[6] TA Birks, JC Knight, and PS Russell. Endlessly single-mode photonic crystal fiber. *Opt. Lett.*, 22:961, 1997.

[7] TA Birks, D Mogilevtsev, JC Knight, PS Russell, and J Broeng. The analogy between photonic crystal fibres and step index fibres. In *OFC/IOOC '99 Technical Digest*, pages 114/FG4–1. Opt. Soc. Am., Feb. 1999.

[8] JC Knight, TA Birks, PSJ Russell, and JP de Sandro. Properties of photonic crystal fiber and the effective index model. *J Opt. Soc. Am. A*, 15:748, 1998.

[9] MJ Steel, TP White, CM de Sterke, RC McPhedran, and LC Botten. Symmetry and degeneracy in microstructured optical fibers. *Opt. Lett.*, 26:488, 2001.

[10] G. P. Agrawal. *Nonlinear Fiber Optics.* Academic Press, 3 edition, 2001.

[11] Shen YR. *Principles of Nonlinear Optics.* Wiley, New York, 1984.

[12] A Boskovic, SV Chernikov, JR Taylor, L GrunerNielsen, and OA Levring. Direct continuous-wave measurement of n_2 in various types of telecommunication fiber at $1.55\mu m$. *Opt. Lett.*, 21:1966, 1996.

[13] FM Mitschke and LF Mollenauer. Discovery of the soliton self-frequency shift. *Opt. Lett.*, 11:659, 1986.

[14] JP Gordon. Theory of the soliton self-frequency shift. *Opt. Lett.*, 11:662, 1986.

[15] *Dig. 2nd Int. Conf. Int. Opt.*, 1977.

[16] JB MacChesney, PB O'Connor, and HM Presby. A new technique for preparation of low-loss and graded index optical fibers. *Proc. IEEE.*, 62:1278–1279, SEP 1974.

[17] JC Knight, TA Birks, PS Russell, and DM Atkin. All-silica single-mode optical fiber with photonic crystal cladding. *Opt. Lett.*, 21:1547, 1996.

[18] TM Monro, YD West, DW Hewak, NGR Broderick, and DJ Richardson. Chalcogenide holey fibres. *Electron. Lett.*, 36:1998, 2000.

[19] VVRK Kumar, AK George, WH Reeves, JC Knight, PS Russell, FG Omenetto, and AJ Taylor. Extruded soft glass photonic crystal fiber for ultrabroad supercontinuum generation. *Opt. Express*, 10:1520, 2002.

[20] VVRK Kumar, AK George, JC Knight, and PS Russell. Tellurite photonic crystal fiber. *Opt. Express*, 11:2641, 2003.

[21] H Han, H Park, M Cho, and J Kim. Terahertz pulse propagation in a plastic photonic crystal fiber. *Appl. Phys. Lett.*, 80:2634, 2002.

[22] MA van Eijkelenborg, MCJ Large, A Argyros, J Zagari, S Manos, NA Issa, I Bassett, S Fleming, RC McPhedran, CM de Sterke, and NAP Nicorovici. Microstructured polymer optical fibre. *Opt. Express*, 9:319, 2001.

[23] MA van Eijkelenborg, A Argyros, G Barton, IM Bassett, M Fellew, G Henry, NA Issa, MCJ Large, S Manos, W Padden, L Poladian, and J Zagari. Recent progress in microstructured polymer optical fibre fabrication and characterisation. *Opt. Fiber Technol.*, 9:199, 2003.

[24] A Ortigosa-Blanch, JC Knight, WJ Wadsworth, J Arriaga, BJ Mangan, TA Birks, and PSJ Russell. Highly birefringent photonic crystal fibers. *Opt. Lett.*, 25:1325, 2000.

[25] TP Hansen, J Broeng, SEB Libori, E Knudsen, A Bjarklev, JR Jensen, and H Simonsen. Highly birefringent index-guiding photonic crystal fibers. *IEEE Photon. Technol. Lett.*, 13(2001):588–590, Jun 2001.

[26] K Suzuki, H Kubota, S Kawanishi, M Tanaka, and M Fujita. High-speed bi-directional polarisation division multiplexed optical transmission in ultra low-loss (1.3 db/km) polarisation-maintaining photonic crystal fibre. *Electron. Lett.*, 37(23):1399–1401, Nov 2001.

[27] J Noda, K Okamoto, and Y Sasaki. Polarization-maintaining fibers and their applications. *J Lightwave Technol.*, 4(8):1071–1089, Aug 1986.

[28] Arturo Ortigosa Blanch. *Highly birefringent photonic crystal fibres: linear and nonlinear effects.* PhD thesis, Univ. of Bath, 2002.

[29] DV Skryabin, F Luan, JC Knight, and PS Russell. Soliton self-frequency shift cancellation in photonic crystal fibers. *Science*, 301:1705, 2003.

[30] WH Reeves, JC Knight, PSJ Russell, and PJ Roberts. Demonstration of ultra-flattened dispersion in photonic crystal fibers. *Opt. Express*, 10:609, 2002.

[31] WH Reeves, DV Skryabin, F Biancalana, JC Knight, PS Russell, FG Omenetto, A Efimov, and AJ Taylor. Transformation and control of ultra-short pulses in dispersion- engineered photonic crystal fibres. *Nature*, 424:511, 2003.

[32] WH Reeves. *Photonic crystal fibre: the ultra-flattened dispersion regime.* PhD thesis, Univ. of Bath, 2003.

[33] WJ Wadsworth, RM Percival, G Bouwmans, JC Knight, TA Birks, TD Hedley, and PS Russell. Very high numerical aperture fibers. *IEEE Photon. Tech. Lett.*, 16:843, 2004.

[34] K Furusawa, A Malinowski, JHV Price, TM Monro, JK Sahu, J Nilsson, and DJ Richardson. Cladding pumped ytterbium-doped fiber laser with holey inner and outer cladding. *Opt. Express*, 9:714, 2001.

[35] WJ Wadsworth, RM Percival, G Bouwmans, JC Knight, and PSJ Russel. High power air-clad photonic crystal fibre laser. *Opt. Eexpress*, 11:48, 2003.

[48] N Venkataram, NT Gallagher, CM Smith, D Muler, JA West, KW Koch, and JC Fajardo. Low loss (13db/km) air core photonic band-gap fiber. In *Proceeedings of the 28th ECOC (2002)*, volume Copenhagen, Denmark, page PD1.1, 2002.

[49] BJ Mangan, L Farr, A Langford, PJ Roberts, DP Williams, F Couny, M Lawman, M Mason, S Coupland, R Flea, H Sabert, TA Birks, JC Knight, and PStJ Russell. Low loss (1.7db/km) hollow core photonic bandgap fiber. In *Proceedings of OFC 2004*, page PDP24, Los Angeles, 2004. OSA.

[50] JA West, CM Smith, NF Borrelli, DC Allan, and KW Koch. Surface modes in air-core photonic band-gap fibers. *Opt. Express*, 12:1485, Apr. 2004.

[51] JK Ranka, RS Windeler, and AJ Stentz. Optical properties of high-delta air-silica microstructure. *Opt. Lett.*, 25:796–798, 2000.

[52] TP Hansen, J Broeng, C Jakobsen, G Vienne, HR Simonsen, MD Nielsen, PMW Skovgaard, JR Folkenberg, and A Bjarklev. Air guidance over 345m large-core photonic bandgap fiber. *Postdeadline paper OFC2003 Atlanta*, PD4-1, 2003.

[53] K Takada, J Noda, and R Ulrich. Precison measurement of modal birefringence of highly birefringent fibers by periodic lateral force. *Appl. Opt.*, 24:4387, 1985.

[54] K Saitoh and M Koshiba. Photonic bandgap fibers with high birefringence. *IEEE Photon. Technol. Lett.*, 14:1291–1293, 2002.

[55] D Muller, J West, and K Koch. Interferometric chromatic dispersion measurement of a photonic gandgap fiber. In *Proc. SPIE Vol. 4870 : Active and Passive Optical Components for WDM Communications II*, pages 395–403, JUL 2002.

[56] G Humbert, JC Knight, G Bouwmans, PS Russell, DP Williams, PJ Roberts, and BJ Mangan. Hollow core photonic crystal fibers for beam delivery. *Opt. Express*, 12:1477, 2004.

[57] MJF Digonnet, HK Kim, J Shin, SH Fan, and GS Kino. Simple geometric criterion to predict the existence of surface modes in air-core photonic-bandgap fibers. *Opt. Express*, 12:1864, 2004.